Fiber optics for terahertz detection: Toward single-pulse terahertz detection using the dispersive Fourier transform

Rachel Ostic

Thesis submitted to the University of Ottawa
in partial Fulfillment of the requirements for the degree of
Master's in Physics

Department of Physics
Faculty of Science
University of Ottawa

uOttawa

Abstract

Terahertz spectroscopy shows promise in applications including quality control, security and medical imaging, but remains limited by slow data acquisition. This also poses an impediment to the study of samples undergoing irreversible transitions, as typical schemes rely on the assumption that results are consistent from pulse to pulse. In this work, we propose a high-speed terahertz detection technique based on chirped-pulse encoding that can enable single-shot measurements up to laser repetition rates in the MHz. An all-normal dispersion optical fiber is used to create a broadband probe spectrum, onto which the terahertz pulse waveform is encoded as a phase modulation. The sampling process makes use of the dispersive Fourier transform, a technique which maps the spectral features of a pulse into the time domain, in this case via the dispersion of a long commercial optical fiber. The elongated pulse can subsequently be detected with a high-speed photodetector and oscilloscope. We show steps toward implementing the technique by characterizing the components required to shape the probe pulse and providing some proof-of-concept measurements. In addition, fiber optic simulation procedures are detailed including complete coupled generalized nonlinear Schrödinger equations to provide insight into polarization effects that occur during highly nonlinear processes such as supercontinuum generation.

Contents

List of Figures

List of Tables

Statement of original contributions

For the single-pulse terahertz detection, Jean-Michel Ménard and Nicolas Joly (Max Planck Institute for the Science of Light) initiated the project (see Sections 2, 4). Rachel Ostic and Lauren Gingras aligned the terahertz generation scheme using tilted pulse front. Rachel Ostic aligned the terahertz detection components and collected data to characterize them. The supercontinuum generation in photonic crystal fiber was realized by Nicolas Couture and Rachel Ostic with support from Jean-Michel Ménard (see Section 3). Nicolas Couture and Rachel Ostic aligned the experiment, Nicolas Couture collected data, both contributed to the analysis of experimental results. Rachel Ostic developed the numerical model. The remaining contributors P. Harshavardhan Reddy, Shyamal Das, Anirban Dhar, Mrinmay Pal, Mukul Chandra Paul, Ajoy Kumar Kar were involved with fiber design and fabrication.

Two additional small contributions are not addressed in this thesis but are mentioned below. First, Rachel Ostic created data acquisition programs and schematic figures for an experiment on time-resolved second-order correlation measurements of nanolasers (project led by Roberto Morandotti, Institut national de la recherche scientifique). Second, Rachel Ostic contributed equally with Oliver Benning to design and implement a simple reinforcement learning model to solve a single-player game.

Publications during MSc

1. Nicolas Couture, **Rachel Ostic**, P Harshavardhan Reddy, Ajoy Kumar Kar, Mukul Chandra Paul, and Jean-Michel Ménard. Polarization-resolved supercontinuum generated in a germania-doped photonic crystal fiber. Journal of Physics: Photonics, 3(2):025002, March 2021.

2. **Rachel Ostic**, Jean-Michel Ménard. Speeding Up Ultrafast Spectroscopy. Physics 14, 23, February 2021.

Conference contributions during MSc

1. **Rachel Ostic**, Nicolas Couture, P Harshavardhan Reddy, Ajoy Kumar Kar, Mukul Chandra Paul, Jean-Michel Ménard. Adding a linear contribution to depolarization in simulations of supercontinuum generation. 2021 CAP Virtual Congress.

2. Nicolas Couture, **Rachel Ostic**, P Harshavardhan Reddy, Ajoy Kumar Kar, Mukul Chandra Paul, Jean-Michel Ménard. Wavelength-dependent depolarization in fiber-based supercontinuum. 2021 CAP Virtual Congress.

3. **Rachel Ostic**, Nicolas Couture, P. Harshavardhan Reddy, Ajoy K. Kar, Mukul C. Paul, Jean-Michel Ménard. Simulation of Linear Depolarization Effects During Supercontinuum Generation in Optical Fiber. Photonics North 2021.

4. Agnes George, A. Aadhi, Andrew Bruhacs, **Rachel Ostic**, Erin Whitby, William E. Hayenga, Zhiming M. Wang, Michael Kues, Christian Reimer, Mercedeh Khajavikhan, Roberto Morandotti. Time-resolved second-order correlation measurements of nanolasers. Photonics North 2021.

5. Agnes George, A. Aadhi, Andrew Bruhacs, **Rachel Ostic**, Erin Whitby, William E. Hayenga, Zhiming M. Wang, Michael Kues, Christian Reimer, Mercedeh Khajavikhan, Roberto Morandotti. Time-resolved second-order correlation measurements of metallic coaxial nanolasers under pulsed optical excitation. CLEO 2021.

6. **Rachel Ostic**, Oliver Benning, Patrick Boily. Solving JumpIN' Using Zero-Dependency Reinforcement Learning (Student Abstract). 35th AAAI Conference on Artificial Intelligence (AAAI-21).

7. Nicolas Couture, **Rachel Ostic**, P. Harshavardhan Reddy, Ajoy Kumar Kar, Mukul Chandra Paul, Jean-Michel Ménard. Polarization resolution of a fiber-based supercontinuum spanning more than 2 octaves. Frontiers in Optics 2020.

8. Nicolas Couture, **Rachel Ostic**, P. Harshavardhan Reddy, Shyamal Das, Anirban Dhar, Mrinmay Pal, Mukul Chandra Paul, Ajoy Kumar Kar, Jean-Michel Ménard. Polarization analysis of a supercontinuum generated in a germania-doped photonic crystal fiber. CLEO 2020.

9. **Rachel Ostic**, Lauren Gingras, Nicolas Joly, Jean-Michel Ménard. Single-pulse THz spectroscopy using the dispersive Fourier transform (Poster presentation). Schawlow-Townes Symposium 2019.

1 Introduction

1.1 Terahertz radiation

Terahertz (THz) radiation (or "T-rays") denotes the portion of the electromagnetic spectrum which falls in the 0.1 to 10 THz frequency range (i.e. near frequency order of magnitude 10^{12} Hz), between the optical and electronic regions of the spectrum [15]. These limits may be translated to the wavelengths 3 mm to 30 μm, wavenumbers 3 cm^{-1} to 333 cm^{-1} or photon energies 0.4 meV to 40 meV as shown in Figure 1. The photon energy in this region corresponds to the thermal weighting in a Boltzmann distribution near room temperature ($k_BT/h \sim 6$ THz) meaning that this spectral band is part of the incoherent thermal radiation surrounding us [16].

Despite the natural prevalence of THz light from blackbody sources, this frequency range came to be known as the "THz gap" owing to the lack of coherent sources able to produce this type of radiation before the 1980s [17, 16]. Since then, a variety of THz sources have been developed including incoherent, continuous wave emitters and coherent, pulsed emitters with a range of different bandwidths.

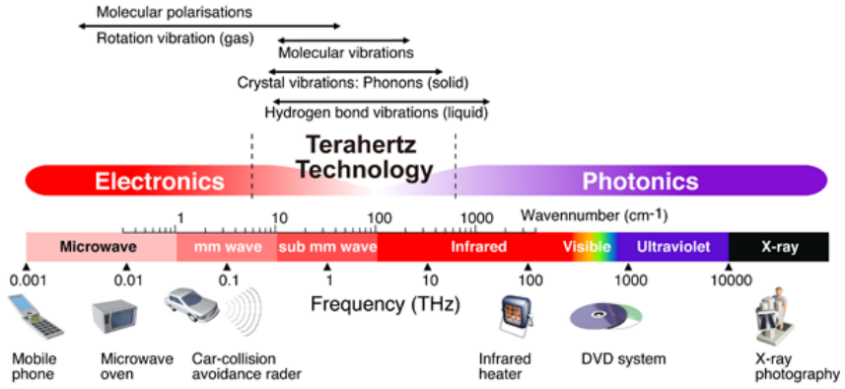

Figure 1: Electromagnetic spectrum spotlighting the THz region in the context of other spectral bands and technologies [1].

1.2 Overview of techniques and applications

There are two frequently-employed techniques to generate coherent THz radiation, namely through the use of photoconductive antennae and via optical rectification, down-converting ultrafast laser light to the THz region. The first emitters of coherent THz radiation were developed using photoconductive switches coupled to femtosecond laser systems [17]. In photoconductive antennae, the current density j in the biased semiconductor structure varies on a picosecond time scale when subject to ultrafast optical excitation. In this case, $E_{THz} \propto \frac{\partial j}{\partial t}$. The same type of effect can also be used to detect THz radiation coherently by gating an antenna with an ultrafast optical beam [18]. Alternately, electro-optic sampling with a nonlinear crystal is another coherent detection strategy in the time domain [19]. Beyond these two generation and detection techniques, there are other sources of THz radiation. THz pulses can be generated in air by mixing laser pulses with their second harmonic in an optically-generated plasma [15, 20]. High-power free electron beams are a source of pulsed or continuous wave THz radiation [16]. Spintronic heterostructures pumped by laser oscillators can deliver pulsed radiation covering a 1 to 30 THz band [21]. Incoherent black body radiation can be measured with thermal detectors as is common in Fourier transform infrared spectroscopy, but this suffers from low output power

in the range of interest and provides only intensity information [19]. Finally, THz radiation can be generated by quantum cascade lasers and detected with spectrally-matched quantum-well photodetectors [22]. Some of these methods will be discussed further as they relate to this work in Section 2.

Coherent pulsed radiation lends itself well to time-domain detection using optical probes since the oscillations of THz pulses, with periods on the order of picoseconds, can be sampled at a resolution corresponding to the duration of a near-infrared or optical femtosecond pulse. This is the basis of THz time-domain spectroscopy (THz TDS), a type of measurement where the electric field waveform of a THz pulse is resolved in the time domain using an optical probe. Rather than detecting spectral intensity directly, the time-varying electric field is Fourier transformed to give the spectral amplitude and phase. This data acquisition technique allows the extraction of both real and imaginary parts of the refractive index of a sample without relying on the Kramers-Kronig relations, which represents a major advantage over other spectroscopy techniques in the far infrared such as Fourier transform spectroscopy using broadband thermal sources [23]. Continuous wave THz sources, on the other hand, with narrower spectral bandwidths than the pulsed sources used for THz TDS, are better suited to real-time imaging over greater propagation lengths [3].

As throughout the rest of the infrared, many materials have identifiable resonances in the THz region, allowing for fingerprinting and identification. Rotational and vibrational modes of molecules result in fine features. Water molecules in particular are strongly absorptive in the THz. Lattice dynamics or intraband energy transitions can also play a role in the THz response, with long-range intermolecular order in polycrystalline structures resulting in absorption peaks [15, 3]. Identifying molecular signatures is a significant research area, with efforts moving toward ensuring high resolution, accurate measurements consistent with accessible databases [24, 2]. Semiconductor carrier dynamics and transport properties can also be probed non-invasively in the THz as features including plasma frequency and damping rates are often of the order of 1 THz [25, 26].

Since THz radiation is very low energy, this allows for non-contact and non-ionizing probing of samples, which is an attractive prospect for medical, quality control and security imaging. Materials that are non-polar and non-metallic are typically transparent in the THz range, contrary to in the visible. This includes paper, textiles, polymers, and semiconductors, allowing box or bag contents to be probed [15]. Furthermore, it is possible to differentiate between these materials based on the extracted absorption and and refractive index. This is possible because THz imaging is "functional imaging", meaning that each pixel of the generated snapshot contains full spectral information including amplitude and phase [16].

An imaging example from art history can be seen in Fig. 2. A stained glass panel containing multiple blue pigments can be analyzed using THz transmission spectra, revealing the distribution of different pigments throughout the piece. Many binding agents in the THz also have distinct spectral responses, giving additional insight into the composition of artistic media [2, 1].

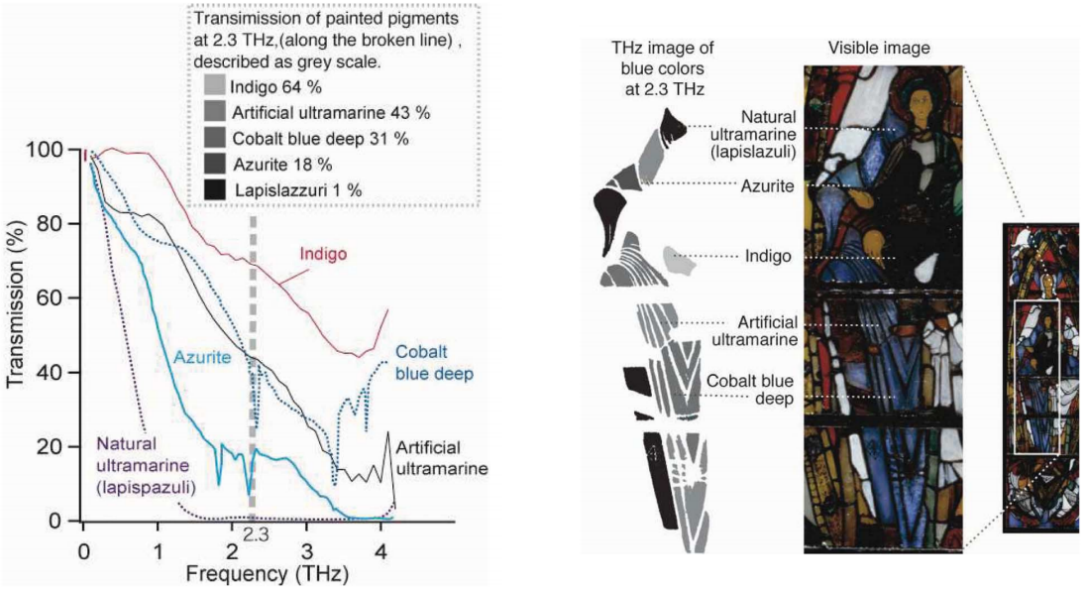

Figure 2: Example of a spectroscopy application in art [2]. Different blue pigments can be distinguished in the THz range by their transmission or absorption spectra. The transmission value at 2.3 THz is used to examine the pigment composition of different sections of the stained glass as illustrated by the translation to grey scale.

In medicine and biology, THz imaging is a candidate for detection of skin cancers, due to its high sensitivity to moisture content [25]. Meanwhile, THz spectroscopy can be used to probe organic polymeric structures' (e.g. DNA, RNA or proteins) low-energy vibrational modes [3].

Some pharmaceutical drugs and explosives exhibit characteristic spectra in the THz, allowing these compounds to be located and characterized even through packaging [3]. Figure 3 illustrates the distinctive absorption spectra of two anomers of glucose, as well as testosterone and 1,3-dinitrobenzene at room temperature and cooled to a cryogenic temperature of 13 K. These spectral profiles can serve, for example, to test the purity of active agents within medications. They can also facilitate the detection and identification of illicit or dangerous substances [18]. Additionally, THz TDS is sensitive to the structural form of a compound, which can reveal whether it is crystalline or amorphous [3].

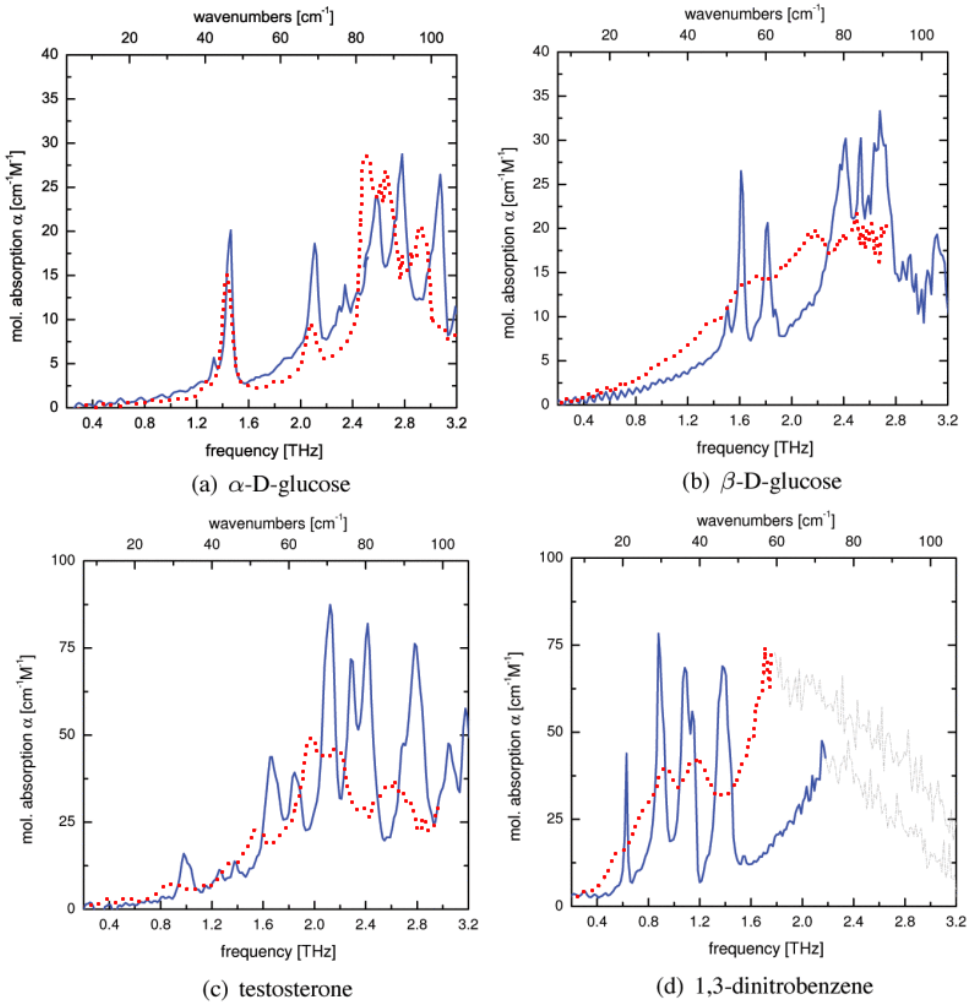

Figure 3: Absorption spectra at room temperature (dotted lines) and at 13 K (solid lines) for a) α-D-glucose, b) β-D-glucose, c) testosterone and d) 1,3-dinitrobenzene [3]. The regions beyond approximately 2 THz in d) are outside the dynamic range of the measurement system and therefore not reliable.

In a different direction, THz is a region for development of 6G networks. As telecommunications bands reach higher and higher frequencies, terahertz technologies may play a role in next generation wireless communication and networking. Water and other atmospheric absorption is significant and must be carefully modelled, extending existing loss frameworks from radiocommunications standards, but test channels have performed well over distances up to 60 m. THz devices are another active field of study enable interfacing with existing communication systems [27].

Throughout these applications, a common challenge is that measurements for pulsed THz techniques can be lengthy and unable to monitor dynamics from pulse to pulse [27, 8]. In Section 2.3, we will summarize some of the efforts made to accelerate THz TDS measurements.

1.3 Fiber optics for terahertz spectroscopy

Optical fiber, and in particular photonic crystal fiber, provides a platform for pulse shaping through its linear and nonlinear optical properties. Previous demonstrations have shown the

potential benefit of hollow-core optical fiber for structuring the spectrum of a commercial laser system in order to achieve tunable broadband THz generation and detection [4]. The use of specialized fiber stages has been proposed as an alternative to large amplifiers or other complex sources [28]. Figure 4 shows an example of nonlinear broadening via self-phase modulation to achieve a THz spectrum spanning close to 5 THz [4].

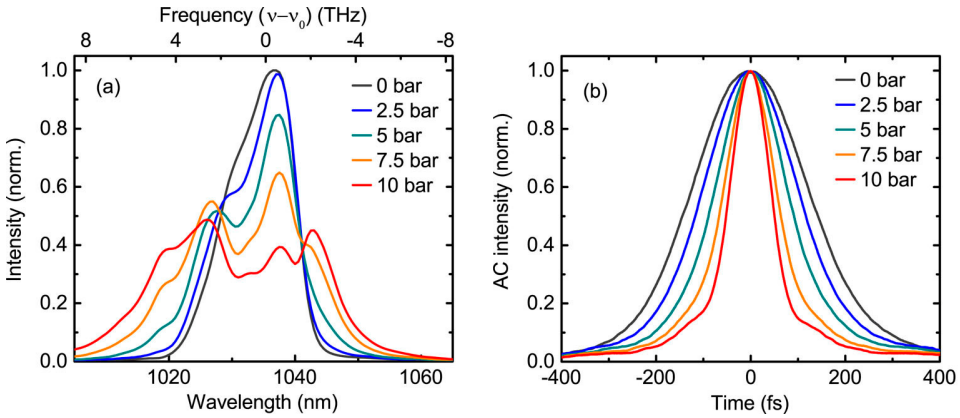

Figure 4: a) Spectral broadening and b) temporal auto-correlation signal intensities for pulses after travelling through an argon-filled hollow-core kagomé photonic crystal fiber at various pressure levels [4].

In this thesis, we will explore the use of fiber for THz detection by exploiting the nonlinear response of a photonic crystal fiber to create a broadband, continuous spectrum to use as a time axis for THz TDS.

Outline

This thesis will summarize investigations into the use of fiber optics to accelerate THz detection in the time domain. It aims to provide a proof of concept for a single-shot THz detection scheme supported by numerical models of spectral broadening and dispersion applied to the probe pulse. The results are still preliminary as the signal-to-noise ratio is far below the level needed to reliably extract information on a single-pulse basis. However, the simulations and experimental tests provide insight into what future directions might be pursued to make the technique viable.

Section 2 gives a summary of the conventional techniques used in the lab to generate and detect THz radiation as well as a review of some of the mathematical models that describe these phenomena.

Section 3 derives extended models for pulse propagation in optical fiber, and discusses their application in the context of polarization-dependent supercontinuum generation.

Section 4 presents the new single-shot scheme for THz detection and illustrates the implementation steps taken to date.

2 Terahertz generation and detection

This section introduces the standard methods to generate and detect THz radiation in the Ultrafast THz lab. First, we consider the nonlinear optical downconversion of NIR laser light into THz radiation, then discuss the generation of high field THz pulses via pump pulse front tilt. Next, we review THz detection through electro-optic sampling. Finally, there is a summary of existing single-shot THz detection techniques.

2.1 Generation

The technique employed in the lab is optical rectification, which can generate a broadband THz pulse. Optical rectification is a second-order nonlinear downconversion process [29]. To better understand this, let us review some principles of nonlinear optics.

The polarization of a material interacting with an electric field $\mathbf{E}$ is denoted $\mathbf{P}$, and follows the relationship:

$$\mathbf{P} = \epsilon_0 \chi \mathbf{E} \tag{2.1}$$

In our experiments, $\mathbf{E}$ is the oscillating electric field of a laser pulse. The quantity $\mathbf{P}$ therefore varies rapidly in time. At low electric field strengths, the polarization of the material results from the movement of electrons analogous to a harmonic oscillator. If the driving field amplitude is increased to a comparable level to the field binding electrons to nuclei, the harmonic potential is no longer sufficient to describe the interaction. Therefore, this linear form must be amended to account for the anharmonicity in the electronic response. The solution is an expansion in $\mathbf{E}$ [30]:

$$\mathbf{P} = \epsilon_0 \left(\chi^{(1)} + \chi^{(2)}\mathbf{E} + \chi^{(3)}\mathbf{E}^2 + \dots \right) \mathbf{E} \tag{2.2}$$

$$= \epsilon_0 \chi^{(1)} \mathbf{E} + \mathbf{P}^{NL} \tag{2.3}$$

where the higher order terms are the nonlinear terms which can be collected into the expression $\mathbf{P}^{NL}$. This form assumes an isotropic material response by the use of scalar coefficients. More generally, $\chi^{(i)}$ may take the form of a tensor to account for the material structure.

This additional $\mathbf{P}^{NL}$ term can be integrated into the wave equation for electromagnetic fields, which determines how they vary as a function of time and position. The wave equation is derived by combining Maxwell's equations into one second order partial differential equation relating the second derivatives in space to the second derivative with respect to time. The nonlinear polarization acts as a source term in the wave equation [30]:

$$\nabla^2 \mathbf{E} - \frac{n^2}{c^2} \frac{\partial^2 \mathbf{E}}{\partial t^2} = \frac{1}{\epsilon_0 c^2} \frac{\partial^2 \mathbf{P}^{NL}}{\partial t^2} \tag{2.4}$$

The assumptions involved in obtaining this formula are that $\nabla(\nabla \cdot \mathbf{E}) = 0$ and that the material is nonmagnetic: $\mathbf{B} = \mu_0 \mathbf{H}$. This is sufficient for cases where there are no free charges or currents and where the magnetic contribution is negligible.

The power series expression for $\mathbf{P}^{NL}$ can lead to the generation of new frequency components from linear combinations of existing ones, which is intuitive from trigonometric identities. If a light source contains spectral components $E_1 = A_1 \cos \omega_1$ and $E_2 = A_2 \cos \omega_2$, then the second

order polarization has a component that becomes:

$$\mathbf{P}^{(2)} \propto \cos\omega_1 \cos\omega_2 = \frac{1}{2}\left(\underbrace{\cos(\omega_1+\omega_2)}_{\text{Sum frequency generation}} + \underbrace{\cos(\omega_1-\omega_2)}_{\text{Difference frequency generation}}\right) \tag{2.5}$$

Optical rectification is the term used for difference frequency generation in the case $\omega_1 = \omega_2$: the resulting field component is a static one across the nonlinear interaction length. The term has also come to be used in the context of THz generation since the difference frequency in the THz region appears locally static relative to the original high-frequency light, i.e. $\omega_{THz} = |\omega_1 - \omega_2| \ll \omega_1$. This second order nonlinear process is due to the presence of a nonzero $\chi^{(2)}$, which occurs in noncentrosymmetric media.

By substituting scalar fields of the form $E_i = A_i e^{i(k_i z - \omega_i t)}$ for ω_1, ω_2 and $\omega_{THz} = \omega_1 - \omega_2$ into the wave equation and applying the slowly-varying amplitude approximation, the evolution of the THz field amplitude over the nonlinear interaction length takes the form:

$$\frac{dA_{THz}}{dz} = \frac{i\chi^{(2)}\omega_{THz}^2}{k_{THz}c^2} A_1 A_2 e^{i(k_1 - k_2 - k_{THz})z} \tag{2.6}$$

Since the downconversion efficiency is usually low, in practice A_1 and A_2 have a negligible z dependence (undepleted pump approximation). This leaves the dependence on z, the propagation direction, in the exponential factor. While Eq. 2.6 assumes monochromatic beams, it is possible to integrate over the spectral bandwidth of an incident beam to calculate the resulting THz spectrum [31]. In order for this conversion to occur, both energy and momentum must be conserved. The first condition is satisfied by $\omega_{THz} = \omega_1 - \omega_2$. The second requires that $\vec{k}_{THz} = \vec{k_1} - \vec{k_2}$, also known as the phase matching condition. The solution to Eq. 2.6 for propagation from $z = 0$ to $z = L$ assuming an undepleted pump takes the form [30]:

$$|A_{THz}(L)|^2 \propto \mathrm{sinc}^2((k_1 - k_2 - k_{THz})L/2) \tag{2.7}$$

which shows the dependence of the efficiency on the phase matching. Therefore, to optimize THz generation using this nonlinear process, the following must be satisfied:

$$\Delta k = k_1 - k_2 - k_{THz} = 0 \tag{2.8}$$

$$\implies n(\omega_1)\omega_1 - n(\omega_2)\omega_2 - n_{THz}\omega_{THz} = 0 \tag{2.9}$$

Another way to write this is with $\omega_1 = \omega_2 + \omega_{THz}$. With this substitution, the phase matching condition can be reformulated to include the group index, $n_g(\omega) = n(\omega) + \omega\frac{\partial n}{\partial \omega}$:

$$n(\omega_2 + \omega_{THz})(\omega_2 + \omega_{THz}) - n(\omega_2)\omega_2 - n_{THz}\omega_{THz} = 0 \tag{2.10}$$

$$\omega_{THz}\left(\underbrace{n(\omega_2+\omega_{THz}) + \omega_2\frac{n(\omega_2+\omega_{THz}) - n(\omega_2)}{\omega_{THz}}}_{\approx n_g(\omega_2)} - n_{THz}\right) = 0 \tag{2.11}$$

$$\implies n_g(\omega_1) \approx n_g(\omega_2) \approx n_{THz} \tag{2.12}$$

This means that in the usual condition of $\omega_{THz} \ll \omega_{NIR}$, the material used for THz generation should have a group index at the pump frequency approximately equal to the refractive index at the THz frequencies of interest. Alternatively, the group velocity of the pump must match the phase velocity of the generated THz radiation. In GaP, the values are approximately $n_{THz} = 3.3$

and $n_g(\omega_{NIR}) = 3.7$ while in ZnTe the values are 3.2 and 3.1 respectively for an 800 nm wavelength in the infrared to generate radiation at 1 THz [5]. It is also worth noting that the solution in Eq. 2.7 shows that Δk is inversely proportional to the coherence length of the nonlinear interaction, given by the position of the first zero of the sinc function $L_c = \frac{2\pi}{k_1 - k_2 - k_{THz}}$ [32]. The coherence length is a measure of the maximum interaction length over which the field components remain in phase to ensure constructive superposition for generation of THz radiation. If the nonlinear interaction occurs over a greater distance than this, the efficiency is very low. Materials for THz generation are chosen both for their suitable phase matching properties and their nonlinear susceptibility. Experimentally, the two initial frequency components ω_1 and ω_2 are part of the spectrum of a femtosecond laser pulse serving as the pump. Optical rectification occurring in the nonlinear medium generates a THz pulse with a bandwidth comparable to that of the pump pulse [15].

2.1.1 Tilted pulse front

Research work has been directed toward the design of high-field THz sources to enable nonlinear characterization of samples in that region of the electromagnetic spectrum or for electron control [29]. While semiconductor crystals such as ZnTe or GaP are effective at generating broadband THz radiation, they unfortunately have quite low nonlinear coefficients which limits the conversion efficiency. Other options include photoconductive switches pumped by ultrafast laser pulses, though these do not provide radiation over as broad a bandwidth, or large-scale sources such as free electron lasers. This leaves high-field THz generation out of reach with most systems.

Lithium niobate ($LiNbO_3$) is an alternative crystal with a nonlinear coefficient an order of magnitude greater than that of ZnTe, though its phase-matching properties for THz generation via optical rectification in the NIR are poor. The refractive index at THz frequencies, 5.0 ($\nu = 1$ THz), is approximately double the group index in the NIR, 2.3 ($\lambda = 800$ nm) [5]. This phase mismatch was remedied by introducing a tilted pulse front scheme, allowing for non-collinear phase-matching in the material to generate THz pulses with pulse energies three orders of magnitude greater than in ZnTe [33, 34, 35, 5]. In addition to allowing more flexible phase-matching conditions, this technique generates a plane THz wave, with components generated at different points in space or time interacting constructively, unlike collinear generation which yields a THz beam in the form of a cone [33]. The tilt is illustrated schematically in Fig. 5. Furthermore, the bandgap of lithium niobate is significantly higher than that of ZnTe, thereby avoiding saturation effects including two- and three-photon absorption at higher pump powers [5]. In this system, the pump intensity front is tilted with respect to the phase front (and propagation direction) of the pulse [29].

Instead of requiring that $v_g(\omega_{NIR}) = v(\omega_{THz})$, the tilt leads to a new condition [5]

$$v_g(\omega_{NIR}) \cos\gamma = v(\omega_{THz}) \tag{2.13}$$

where γ is the tilt angle applied using a grating. This can be seen in Fig. 5 where the projection of the NIR velocity along the direction of THz propagation is in fact $v_g(\omega_{NIR}) \cos\gamma$. For the parameters given above for lithium niobate, this leads to a tilt angle of $\gamma = \arccos\left(\frac{n_g(\omega_{NIR})}{n(\omega_{THz})}\right) = 63°$. This tilt can be achieved by imaging the first diffraction order from a grating into the nonlinear crystal. The tilt angle in free space before the crystal is determined by the grating, and a half wave plate can be used to optimize the polarization orientation for THz generation in the crystal [5] The polarization should be linear and in the plane of the page relative to the

orientation of these schematics. Small adjustments of the tilt angle can also optimize phase matching for a specific THz frequency. After the grating, a one- or two-lens system images the pulse at the grating interface into the crystal [36]. Ray-tracing in Figs. 6 or 7 illustrates this process: the air grating interface is taken as the "object" while the "image" formed by the lens system lies inside the lithium niobate crystal with a profile parallel to the exit interface. This technique has led to the generation of single-cycle pulses with peak THz fields on the order of 1 MV/cm [6]. In fact, photon conversion efficiencies surpassing 100% can be attained through cascaded repeated downconversion of the pump photons [37, 38].

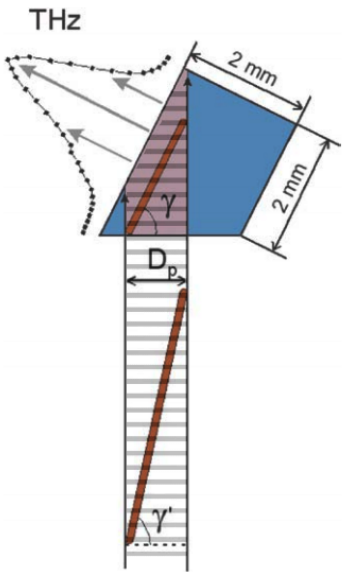

Figure 5: Illustration of pulse front tilt before entering crystal (below) and upon entering crystal depicted in blue. The THz propagates orthogonally to the tilted pulse front [5]. The dark red colour indicates the pulse front or intensity profile of the NIR beam, while the horizontal stripes represent phase fronts or lines of equal phase. The direction of propagation is upward in this schematic, and the pulse front outside the crystal is tilted at angle γ' with respect to the phase fronts. Once inside the crystal, refraction changes this angle to γ. The phase fronts are parallel to the crystal interface upon incidence and the pulse front is parallel to the exit interface.

The crystal is cut such that the pump beam enters at an interface normal to the phase front, while the THz beam exits normally to the adjacent interface, thereby requiring a corner at angle γ as shown in Fig. 5. Though this technique has its challenges in terms of eliminating imaging aberrations, it consistently reaches among the highest peak THz field strengths using optical rectification [7, 36, 29].

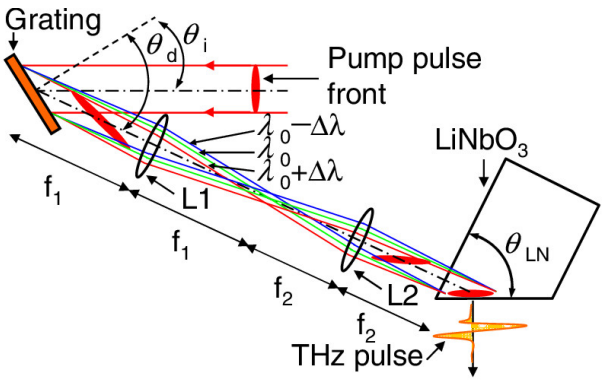

Figure 6: Schematic of pulse front tilt and two-lens imaging layout [6]. The incoming pump pulse front shown in red at the top is parallel to the phase front of the beam and orthogonal to the propagation direction. After the grating, the pulse front is tilted. Lenses L1 and L2 create an image of the air-grating interface in the lithium niobate crystal such that the pulse front tilt angle in the crystal is equal to θ_{LN}

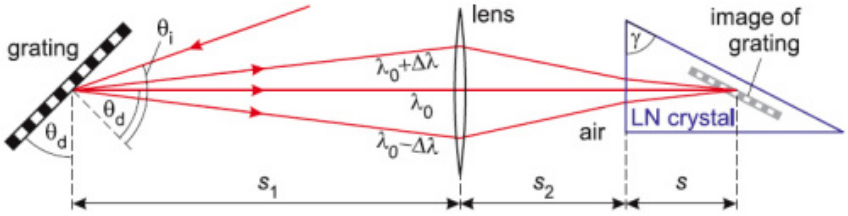

Figure 7: Schematic of one-lens imaging layout [7]. Same idea as Fig. 6 but with a single lens. The imaging system brings the spectral components dispersed by the grating back together to allow the difference frequency generation process to occur.

In this work, the interest in high-field THz generation was in increasing the level of signal to facilitate measurements and to potentially bring samples into a non-equilibrium state where rapid detection would be beneficial.

2.2 Detection

In this section, we focus mainly on electro-optic sampling as this is the technique used in the Ultrafast THz Lab. With a nonlinear crystal such as GaP or ZnTe, THz radiation induces birefringence proportional to the amplitude of its field by the Pockels effect, thereby allowing information from the THz to be mapped to a NIR probe pulse via a phase modulation [30, 15]. This occurs when the NIR and THz pulses are overlapped spatially and temporally within the crystal. To measure the electric field of the THz pulse in time, a mechanical delay stage varies the relative delay between probe and the THz pulse. Figure 8 shows this reconstruction procedure. Detection conditions can be approximated using Jones matrices as follows.

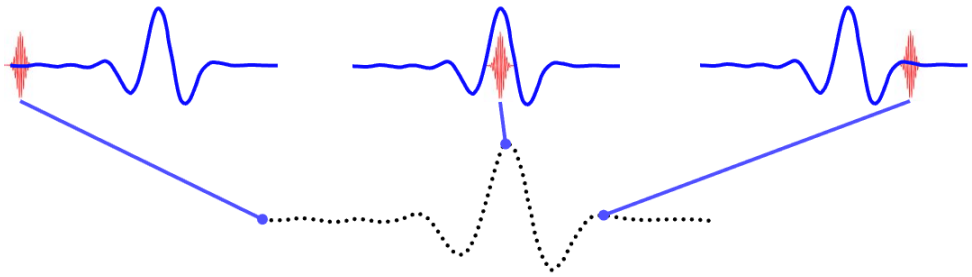

Figure 8: Schematic illustration of electro-optic sampling procedure with multiple overlap points as a function of time to reconstruct full THz waveform. Blue: THz, red: NIR probe, black: example of sampled waveform that is detected.

A rotation matrix brings different optical path elements into the same frame of reference by rotating by angle α:

$$R(\alpha) = \begin{pmatrix} \cos\alpha & \sin\alpha \\ -\sin\alpha & \cos\alpha \end{pmatrix} \tag{2.14}$$

The birefringent crystal can be represented by:

$$B = \begin{pmatrix} e^{-in_sL/\lambda} & 0 \\ 0 & e^{-in_fL/\lambda} \end{pmatrix} \tag{2.15}$$

$$= e^{-i\Theta} \begin{pmatrix} e^{-i\Gamma/2} & 0 \\ 0 & e^{i\Gamma/2} \end{pmatrix} \tag{2.16}$$

where $\Theta = \frac{(n_s+n_f)L}{2\lambda}$ is an average phase factor and $\Gamma = \frac{(n_s-n_f)L}{\lambda} \propto \chi^{(2)}E_{THz}$ represents the phase retardation experienced by the probe pulse due to the THz field. The indices n_s and n_f represent the slow and fast axis refractive indices. The small amount of intrinsic birefringence in the crystal can be neglected if proper balancing is carried out for electro-optic sampling which will be discussed later. If additional sensitivity is needed, compensation using a reference can also be applied to normalize for residual birefringence [39].

Polarization optics include a quarter wave plate with fast axis horizontal:

$$Q = \begin{pmatrix} e^{-i\pi/4} & 0 \\ 0 & e^{i\pi/4} \end{pmatrix} \tag{2.17}$$

The polarization basis is comprised of horizontal (H) and vertical (V) states relative to the optical table frame of reference:

$$e_H = \begin{pmatrix} 1 \\ 0 \end{pmatrix} \tag{2.18}$$

$$e_V = \begin{pmatrix} 0 \\ 1 \end{pmatrix} \tag{2.19}$$

In practice, the incident field is oriented horizontally:

$$E_i = E_0 \begin{pmatrix} 1 \\ 0 \end{pmatrix} \tag{2.20}$$

E_i represents the electric field amplitude of the NIR detection pulse whose polarization state is affected by the presence of the THz radiation in the electro-optic crystal. The quantity measured

experimentally is the intensity incident on a diode. We can use a polarizer to project along an axis oriented at angle β with respect to the horizontal:

$$P(\beta) = \begin{pmatrix} \cos\beta & \sin\beta \end{pmatrix} \tag{2.21}$$

Finally, we can calculate measured signal intensity by taking the product of the projected amplitude with its conjugate (i.e. absolute square). For example, for a crystal at angle ϕ followed by a polarizer at angle β, the electric field can be found via:

$$E_{pol}(\phi, \beta) = P(\beta)R(-\phi)BR(\phi)E_i \tag{2.22}$$

Next, the measured signal S_{pol} is given by:

$$S_{pol}(\phi, \beta) = E_{pol}E_{pol}^* = |E_{pol}|^2 \tag{2.23}$$

$$= \frac{1}{8}E_0^2 e^{-i\Gamma}\left[4e^{i\Gamma} + \left(1 + e^{i\Gamma}\right)^2\cos(2\beta) - \left(-1 + e^{i\Gamma}\right)^2\cos(2\beta - 4\phi)\right] \tag{2.24}$$

Consider the case where the horizontally-polarized background is completely blocked by the polarizer (i.e. $\beta = 90° = \pi/2$). Then we obtain:

$$S_{pol}(\phi, \frac{\pi}{2}) = E_0^2 \sin^2(2\phi)\sin^2(\Gamma/2) \tag{2.25}$$

$$\propto \Gamma^2 \quad \text{for small } \Gamma \tag{2.26}$$

With crystal orientation such that 2ϕ is an odd multiple of $\frac{\pi}{2}$, the THz field amplitude can be detected, but the phase information is lost due to the square.

Alternatively, holding ϕ constant at $\frac{\pi}{4}$ based on the previous condition gives:

$$S_{pol}(\frac{\pi}{4}, \beta) = \frac{1}{2}E_0^2\left(1 + \cos(2\beta)\cos(\Gamma)\right) \tag{2.27}$$

In this case, we notice that the general dependence is of the form $1 + \cos(\Gamma)$, which still conceals the sign information from Γ since $\Gamma \ll 1$. Furthermore, this dependence is ill-suited to detecting small modulations due to the background signal and roughly quadratic response in Γ of the cos function. After considering these cases, we can see that it is feasible to detect whether the probe pulse interacts with a THz pulse, but that measuring the THz waveform would omit phase information. By including additional polarization optics, we can reach a more sensitive and phase-preserving detection system.

2.2.1 Electro-optic sampling

In this scheme, after the THz detection crystal a quarter wave plate is added before a polarizing beamsplitter or Wollaston prism to modify the polarization state of the probe beam and separate its horizontal and vertical components as illustrated in Fig. 9. In this way, two diodes can be used to perform balanced detection, removing correlated background and noise and, more importantly, giving both amplitude and phase of the THz waveform.

After the quarter wave plate with fast axis oriented at angle θ, the electric field becomes:

$$E_{QWP}(\phi, \theta) = \left[R(-\theta)QR(\theta)\right]\left[R(-\phi)BR(\phi)\right]E_i \tag{2.28}$$

Here, we use two orthogonal projections which are obtained through the Wollaston prism:

$$P_1(\beta) = \begin{pmatrix} \cos\beta & \sin\beta \end{pmatrix} \tag{2.29}$$

$$P_2(\beta) = \begin{pmatrix} \cos(\beta + \pi/2) & \sin(\beta + \pi/2) \end{pmatrix} \tag{2.30}$$

The respective intensities are given by:

$$S_1(\phi,\theta,\beta) = |P_1(\beta)E_{QWP}(\phi,\theta)|^2 \tag{2.31}$$
$$S_2(\phi,\theta,\beta) = |P_2(\beta)E_{QWP}(\phi,\theta)|^2 \tag{2.32}$$

with balanced intensity signal $\Delta S = S_2 - S_1$. Keeping the crystal angle at $\phi = \frac{\pi}{4}$ for maximum modulation, the simplest is to take $\beta = 0$ resulting in measurements of the horizontal and vertical polarization components.

$$S_1(\frac{\pi}{4},\theta,0) = \frac{1}{2}E_0^2\left(1+\cos(\Gamma)\cos^2(2\theta)-\sin(\Gamma)\sin(2\theta)\right) \tag{2.33}$$
$$S_2(\frac{\pi}{4},\theta,0) = \frac{1}{2}E_0^2\left(1-\cos(\Gamma)\cos^2(2\theta)+\sin(\Gamma)\sin(2\theta)\right) \tag{2.34}$$
$$\Delta S(\frac{\pi}{4},\theta,0) = E_0^2\left(-\cos(\Gamma)\cos^2(2\theta)+\sin(\Gamma)\sin(2\theta)\right) \tag{2.35}$$

Since the goal is to measure Γ, a small quantity, it is most advantageous to select $\theta = \frac{\pi}{4}$ to obtain:

$$\Delta S(\frac{\pi}{4},\frac{\pi}{4},0) = E_0^2\sin(\Gamma) \propto \Gamma \tag{2.36}$$

Note that other angle combinations such as $\phi = \frac{\pi}{4}, \theta = 0, \beta = \frac{\pi}{4}$ yield the same results. The selected angles for polarizer and Wollaston prism preserve the sign information for Γ.

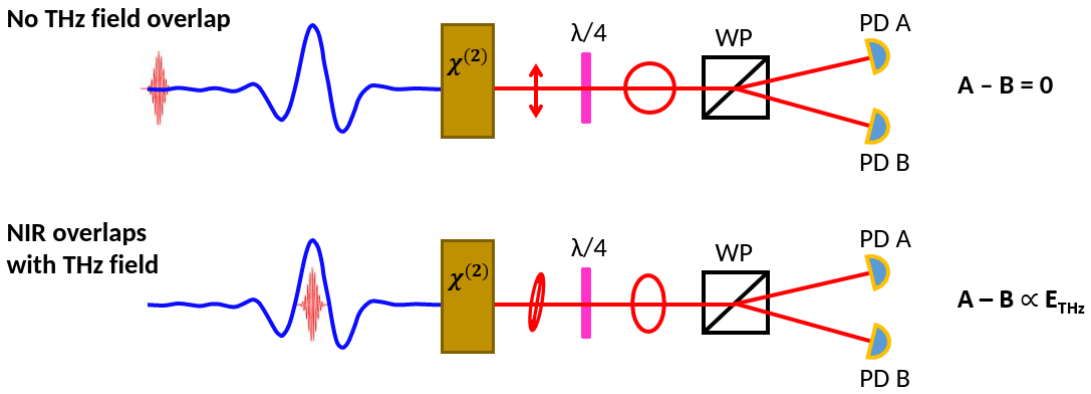

Figure 9: Comparison of detected $\Delta S = A - B$ when THz field is present and absent. Blue: THz, red: NIR probe, $\chi^{(2)}$: crystal, $\lambda/4$: quarter wave plate, WP: Wollaston prism, PD: photodiode.

Since the NIR probe pulse used in this technique has a duration an order of magnitude or more shorter than that of the THz pulse, the instantaneous THz field seen by the probe when the two beams interact in the crystal appears effectively static. Therefore, a mechanical micrometer translation stage can scan over the relative delay between the two beams by modifying one of the path lengths. This sampling process is known as "electro-optic sampling", a balanced detection technique to infer the THz electric field E_{THz}. Resolving E_{THz} in the time domain provides both spectral amplitude and spectral phase information about the THz pulse.

A more exact form for Γ, the phase retardation, is given by the equation [15]:

$$\Gamma = \frac{\omega_{NIR}L}{c}\Delta n = \frac{\omega_{NIR}L}{c}(n_{NIR})^3(r_{41})E_{THz} \tag{2.37}$$

where Δn is the crystal birefringence, ω_{NIR} is the frequency of the detection pulse, L is the thickness of the detection crystal, n_{NIR} is the crystal index of refraction at the detection frequency,

r_{41} is the crystal electro-optic coefficient, and E_{THz} is the electric field amplitude of the THz pulse. The electro-optic coefficient originates in the $\chi^{(2)}$ term from Eq. 2.2, and determines the rate of change of the refractive index of a noncentrosymmetric medium with respect to applied electric field strength. This is not a scalar process: based on the structure of the medium and the polarization of the electric field, the refractive index ellipsoid is deformed [30]. For electro-optic sampling, the birefringence of the detection crystal varies due to the THz field. Knowing the properties of the detection crystal therefore gives a way to calculate the THz electric field amplitude. To estimate it, we can use the diode signals S_1, S_2 and ΔS (Eq. 2.33) measured at the peak field position and compute:

$$|E_{THz}| \approx \frac{|\Delta S|}{S_1 + S_2} \frac{c}{\omega_{NIR} L (n_{NIR})^3 (r_{41})} \tag{2.38}$$

since $\Delta S \approx E_0^2 \Gamma$ where $E_0^2 = S_1 + S_2$. The $\sin\Gamma \approx \Gamma$ approximation holds in most cases as the modulation depth, $\frac{|\Delta S|}{S_1+S_2}$ is significantly below one. Typical values may be on the order of 10^{-3} to 10^{-1} [40].

In the lab, the two photodiodes illustrated in Fig. 9 are connected to a lock-in amplifier to detect the difference signal. An optical chopper sinusoidally modulates the THz generation beam at a selected frequency on the order of 600 Hz that is used as a reference for the lock-in amplifier. The internal local oscillator takes this reference to create an oscillatory reference signal to multiply with the measured signal. By filtering the product and integrating over an averaging period, it is possible to extract the periodic input signal from a very noisy background [41]. This approach is used to accurately measure small Γ signals. Note that due to the longer wavelength of the THz radiation, the THz spot size is over an order of order of magnitude larger than that of the probe pulse, with its frequency content near-uniformly distributed over its profile. Therefore, the probe spot can be well-centred within the THz spot and there are no significant spatial distortions associated with EOS.

2.2.2 Alternate polarization scheme

Different polarization alignments can be used in a similar way to electro-optic sampling, but without the need for careful balancing of the quarter wave plate and Wollaston pair [42, 43]. The following technique is useful when only one diode is available and it is not possible to optimally orient the quarter wave plate at $\frac{\pi}{4}$. Instead, we place the quarter wave plate with its fast axis horizontal ($\theta = 0$). This type of low optical bias measurement reduces the background light on the electro-optic sampling detectors to overcome dynamic range limitations [42]. Assuming $\phi = \frac{\pi}{4}, \theta = 0$ in Eq. 2.31, this yields:

$$S_1(\frac{\pi}{4}, 0, \beta) = E_0^2 \cos^2(\beta - \Gamma/2) \tag{2.39}$$

$$S_2(\frac{\pi}{4}, 0, \beta) = E_0^2 \sin^2(\beta - \Gamma/2) \tag{2.40}$$

$$\approx E_0^2 (\beta - \Gamma/2)^2 \quad \text{for small polarizer angles i.e. } |\beta - \Gamma/2| \ll 1 \tag{2.41}$$

$$\propto \beta^2 - \beta\Gamma + \frac{\Gamma^2}{4} \tag{2.42}$$

$$\approx \beta^2 - \beta\Gamma \tag{2.43}$$

The S_2 quantity with a polarizer angled at β from vertical gives an alternate method to infer the THz waveform by recording a reference signal with THz off (S_{ref}), then a measurement with

THz on (S_{THz}).

$$S_{ref}/E_0^2 = \beta^2 \tag{2.44}$$

$$S_{THz}/E_0^2 = \beta^2 - \beta\Gamma \tag{2.45}$$

$$\implies \Gamma = \frac{S_{ref} - S_{THz}}{E_0\sqrt{S_{ref}}} \tag{2.46}$$

Alternatively, using the quadratic equation:

$$S_{THz}/E_0^2 = \beta^2 - \beta\Gamma + \frac{\Gamma^2}{4} \tag{2.47}$$

$$\implies \Gamma = \frac{2}{E_0}(\sqrt{S_{ref}} \pm \sqrt{S_{THz}}) \tag{2.48}$$

The minus solution is approximately the same as Eq. 2.46 assuming the difference between the reference and THz on measurements is quite small. The wave plate stays aligned horizontally while the polarizer is slightly misaligned from the vertical. The angle β can reach up to approximately 0.3 rad ($= 17°$) to remain close to linear dependence in $\sin\beta$. Previous work has given a correction term to compensate for distortion as a function of polarizer angle which utilizes positive and negative solutions to a quadratic form assuming lock-in amplification to remove background [42]; this has not been assessed in the current solution form though could potentially be included in future.

Though electro-optic sampling is a standard, widely-used technique, it does have a shortcoming in that data acquisition is slow. Scanning across multiple time delays to map out the time-varying THz pulse using lock-in amplification leads to averaging over multiple laser pulses, which is a limitation for irreversible transitions or unstable systems [44]. It also means that for multidimensional spectroscopy, the acquisition time scales to the power of the number of dimensions to consider.

To combat this inefficient scaling, there are numerical techniques which can be implemented to perform data reconstruction from a randomly sampled subset of the full measurement range. One algorithm called "compressed sensing" has been shown to require only 15% of the data points used in a typical THz spectroscopy measurement to obtain the same information as a complete dataset [45]. The technique works on the assumption that the signal being measured is sparse in another basis, and that the transformation to said basis is known – common examples of operators are discrete Fourier or wavelet transforms. The randomly down-sampled signal can then be numerically "enhanced" up to the desired resolution by fitting to minimize error on the sample set while maximizing sparsity in the transform basis. The trade-off between those two optimization goals can be controlled via regularization in the numerical solution to find the best balance for the specific type of measurement. The reconstruction works in multiple dimensions, an advantage for THz pump-probe measurements, for example, which require scanning over two different temporal delay axes [45, 46]. Still, a factor of 6 acceleration in data acquisition time is not fast enough to detect individual THz pulses. The next section shows some existing experimental schemes that do enable single-shot detection.

2.3 Review of single-shot THz detection techniques

The idea of speeding up THz detection is not a new one - various schemes have been tested previously and will be presented in the following section. Measuring the full pulse waveform in a single shot has a number of advantages: reducing acquisition time, overcoming multi-shot limitations with high-field sources with large fluctuations, opening up the opportunity to

measure irreversible transitions. In these cases, each pulse must be treated as a separate event to accurately characterize the processes occurring.

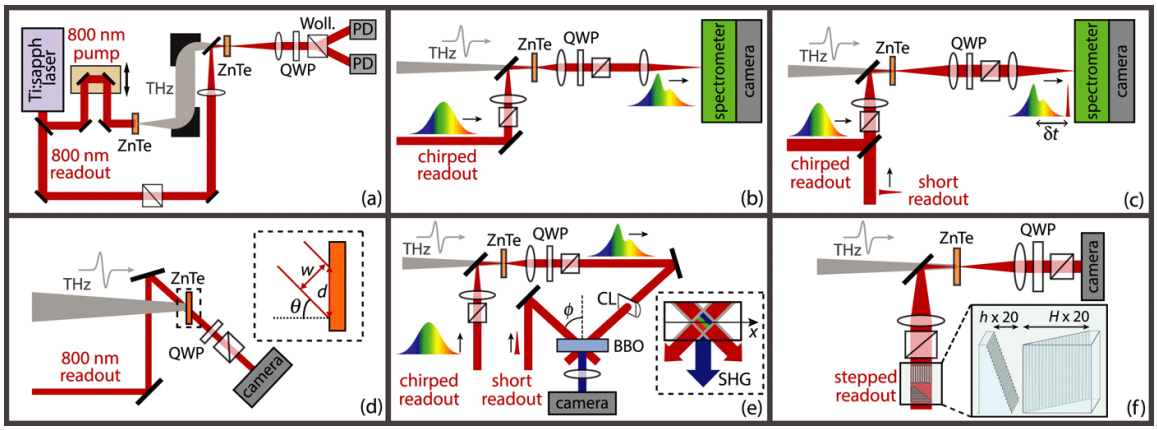

Figure 10: Schematic illustration of various single-shot detection techniques by Teo *et al* [8]. a) Electro-optic sampling, b) Collinear frequency-to-time encoding on a chirped probe pulse with spectrometer for detection, b) Collinear frequency-to-time encoding on a chirped probe with interferometric readout pulse and spectrometer for detection, c) Noncollinear space-to-time mapping with expanded beams and camera for detection, e) Space-to-time encoding based on noncollinear second harmonic generation between chirped probe pulse (as in b) and short readout pulse detected on camera, f) Angle-to-time encoding using expanded beam and transmissive echelons with camera for detection.

Figure 10 is a comparison of some of the proposed and demonstrated techniques. In a) the standard electro-optic sampling approach is shown. Many of the techniques that have been tested can be categorized into the following sections including frequency-to-time mapping as used in 10b), c) and e); space-to-time mapping as in d) and e); and angle-to-time mapping as in f) [8]. Two other sections are also included to describe further approaches to rapid THz detection; these are asynchronous detection methods and techniques without optical probes.

2.3.1 Frequency-to-time mapping

Examples of this technique are given in Figure 10b) and c). In the original demonstration of this scheme, the detection pulse is chirped to match the duration of a THz pulse, then goes through the same path as it would for electro-optic sampling. However, the signal is read out using a spectrometer and detector synchronized to the laser repetition rate. The time-varying THz pulse modulates the chirped pulse, therefore there is a mapping between time and frequency. By measuring the spectrum of the chirped probe, the THz signal can be recovered [47]. Since the Pockels effect gives a polarization rotation proportional to the THz field, an analyzer at 45° can be used instead of a Wollaston prism for the simplest possible phase-sensitive implementation ($E \propto \frac{\Delta I(\omega)}{I_0(\omega)}$). However, balanced detection can be achieved if the difference between spectra for both polarization components is measured [8, 48].

One of the main issues with this approach is that when encoding the THz waveform onto the chirped laser pulse, the fixed laser spectral bandwidth leads to a tradeoff between the THz bandwidth and spectral resolution that can be measured [8, 49]. Work has been done to bypass this limitation, for instance by generating a visible supercontinuum probe in sapphire [48, 50]. There are also distortion effects which depend on the detection pulse duration and intensity [51].

A further improvement to the technique can be obtained through linear spectral interferometry as shown in Figure 10c where the chirped probe pulse is overlapped with a short reader pulse separated by a time delay δt [52]. The temporal resolution is then set by the reader pulse duration. This also allows the THz modulation to be encoded either in phase or amplitude, depending on the polarization state of the probe relative to that of the THz. The phase encoding has potential as a high-field detection strategy to avoid over-rotation which can occur in electro-optic sampling [53, 54], though the detection bandwidth is limited by the resolution of the spectrometer, since it must be able to resolve interference fringes over the probe spectrum [8]. To overcome some of the resolution challenges, interferometric techniques can be combined with iterative numerical analysis [55]. These techniques use a two-dimensional CCD array, which limits the speed of the detection system based on the minimum integration and recovery time.

The proposed single pulse scheme developed in Section 4 still uses the chirped pulse encoding principle described above but includes a specialized optical fiber [56] to shape the spectrum of the detection pulse in order to remove the limitations of the fixed laser bandwidth.

2.3.2 Space-to-time mapping

In Fig. 10d, the THz modulation is applied to the probe pulse via a space-to-time mapping [57, 58, 59, 44, 60]. Rather than focusing the THz and probe beams onto the detection crystal, they must have a spot size on the order of a few mm to reach a time window spanning the duration of the THz pulse. Then, the probe pulse can be measured using a camera, which has the temporal axis mapped across the pixels. A noncollinear geometry is one option, while tilting the probe pulse-front is another to increase potential interaction length. The use of large spots means that the THz field is weaker than in conventional electro-optic sampling where the beams are tightly focused. Furthermore, because the probe spot size is the close to the THz spot size, diffraction-related spectral and intensity aberrations in the beams must also be considered [8, 59].

Another space-to-time technique shown in Fig. 10e combines a THz-modulated, chirped probe pulse with second harmonic generation [61]. In this approach, the probe is not measured with a spectrometer, but rather overlapped noncollinearly with a short readout pulse in a BBO crystal to generate a second harmonic beam. This second harmonic beam contains the information from the THz modulation in its spatial profile. This technique addresses some of the challenges associated with chirped-pulse encoding (Fig. 10b) and spatial encoding (Fig. 10d) by reducing the reliance on full characterization of the frequency-dependent chirp or THz spatial profile. However, the use of a second nonlinear process makes it difficult to perform balanced detection and leads to a noisier signal [8].

2.3.3 Angle-to-time mapping

In Fig. 10f, an example of an angle-to-time mapping technique is illustrated. An expanded probe beam passes through a pair of orthogonal transmissive echelons, which add a spatially-dependent optical path length to create a grid of different time delays at which to probe the THz pulse. When the probe is focused at the electro-optic crystal, the THz signal in time is mapped to the angle of the probe pulse. The probe is then imaged on a camera. The resulting two-dimensional measurement can be analyzed in terms of the time-delay grid to recover the THz signal [62, 63, 64, 65, 66]. This technique does not require significant changes to the geometry used for electro-optic sampling and allows for balanced detection if the camera detection area is

large enough to capture both polarization states. However, the imaging scheme requires careful consideration of the resolution and depth of focus to detect the edges of the echelons, and is highly sensitive to fabrication defects [8, 63].

Another example of angle-to-time mapping uses two sub-pulses to probe at different moments, though with the goal of examining inter-pulse rather than intra-pulse dynamics [60].

Instead of spreading the temporal duration over an elongated focal point, it is also possible to exploit the properties of Gaussian optics to encode the THz onto the curved wavefront of the probe pulse before it converges at the focus [67]. This technique is simple to implement, requiring only the addition of a lens in the probe path and can also yield information about the spatial distribution of the THz beam. This limits the measurement interval to a few picoseconds.

2.3.4 Asynchronous methods

Other high-speed detection methods have been demonstrated, notably asynchronous optical sampling [68]. In this technique, two different laser systems are used, one for THz generation and the other for detection. The repetition rates are slightly detuned from one another at a finely controlled offset frequency. This varies the delay between THz and probe by an integer multiple of the time shift determined by the offset frequency from pulse to pulse, effectively allowing the measurement to last the full duration from one pulse to the next. The probe signal can then be read out on an oscilloscope at the probe repetition rate. This provides both high-resolution and broad bandwidth THz data, but requires two mode-locked lasers which can be accurately synchronized in order to replace the mechanical delay stage. Furthermore, this technique is not strictly single-shot in the sense that the measurement is performed over a sequence of pulses, which makes this method inapplicable to recording irreversible processes occurring on a time scale comparable to the repetition rate.

Another technique using two femtosecond lasers makes use of frequency combs in order to perform multifrequency-heterodyning detection [9]. In this technique illustrated in Fig. 11, the two laser frequency combs give rise to slightly offset THz and photocurrent combs which can be demodulated based on the known frequency difference between pump and probe mode-locked lasers. This work is interesting to create an accurate THz frequency “ruler” but suffers from some of the same limitations are the previous technique.

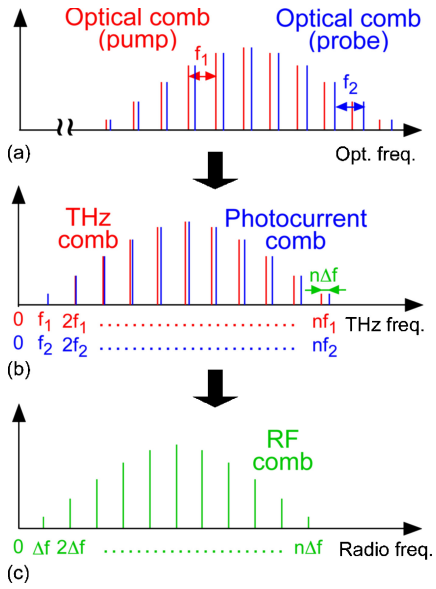

Figure 11: Schematic of frequency comb from [9]. Two lasers each produce a frequency comb; one is used to generate THz and the other for detection.

2.3.5 Strategies without optical probe

In a different direction, an interferometric technique using the THz beam without any optical probe has been demonstrated with a pair of specialized antenna coupled field effect transistor (FET) detectors, one for linear and the other for circular polarization [69]. After a beamsplitter, the two THz paths, one for a sample and one as a reference, are passed through polarizers to set them to orthogonal states. This allows them to be detected independently at the detector position via two types of interferogram. While this technique shows promise, it is not truly single-shot as it uses a continuous wave source and allows only the determination of an optical path difference caused by a sample. This may be a useful acceleration for raster scanning samples rapidly to analyze their spatial profile.

Alternatively, a specially fabricated metamaterial can be used as a grating in the THz range with a camera to create a spectrometer operating between 0.25 and 10 THz [70]. Cameras in this range are often thermal devices, leading to potentially long response times. A similar technique was used to spectrally filter and measure electron bunch properties of a free electron laser (FEL) [71]. A series of custom gratings and detectors were used to measure single-shot spectra of pulses from the IR to THz bands. This type of technique does not give the time-resolved amplitude and phase of the THz signal, however. It remains useful in cases of highly broadband radiation as in [71] to avoid the absorption limitations of electro-optic crystals.

Others have used improving THz detectors like microbolometers to perform measurements similar to FTIR, obtaining THz autocorrelations between 10 and 40 THz [72].

2.3.6 Takeaways

A common theme among these techniques is that integration time or frame rate of the array detector used to record the probe pulse becomes a limiting factor for the laser repetition rate to ensure that each pulse is captured. Rates up to the order of kHz are manageable, however beyond this level other data acquisition strategies should be considered. This leads us to consider the

dispersive Fourier transform, which has been demonstrated as an effective technique to monitor dynamics at a single-pulse level [56, 73, 74]. This will be discussed further in Section 4.

Furthermore, once installed, many of these techniques give inflexible detection pulse duration or temporal resolution. The addition of a photonic crystal fiber in the detection line can lead to a more flexible scheme with bandwidth tuning based on input power level [28]. To that effect, the following section gives background on the properties of optical fiber and how it can be used to generate broadband radiation.

3 Dispersion and nonlinear effects in optical fiber

A significant research contribution has been in deriving and implementing extended supercontinuum broadening simulations, including optional polarization information based on coupled mode equations. Supercontinuum generation refers to the creation of a highly broadband spectrum – typically spanning well over 100 nm, via propagation through a nonlinear medium. Here, we present the models used to simulate supercontinuum generation in optical fiber. This work stemmed from the importance of accurately characterizing and modelling the properties of two different types of optical fiber used in experiments detailed in Section 4. Spectral broadening and temporal chirp are two of the parameters required to enable spectral encoding of THz information onto a tuned probe pulse. This section provides a review of pulse shaping dynamics in optical fiber, a derivation of a frequency domain propagation equation, and results from a case study on supercontinuum generation in photonic crystal fiber which considers polarization dependent broadening. Simulation code is presented in the Appendix.

Two main physical properties of optical fiber are its dispersion and nonlinear response. Dispersion determines the rate at which different spectral components travel through a medium, causing pulses to distort and elongate. In optical fiber, there are two contributions to the total dispersion, one from the core medium itself and another, the waveguide dispersion, resulting from the frequency dependence of the guided mode structure and size. The total dispersion is modelled by expanding the wavenumber within the medium β about the central frequency of interest ω_0:

$$\beta(\omega) = n(\omega)\frac{\omega}{c} = \beta_0 + \beta_1(\omega-\omega_0) + \frac{1}{2!}\beta_2(\omega-\omega_0)^2 + \frac{1}{3!}\beta_3(\omega-\omega_0)^3 + \dots \tag{3.1}$$

where $n(\omega)$ represents the frequency-dependent index of refraction. Physically, β_1 represents the inverse of the group velocity and β_2 is the group velocity dispersion. The sign of β_2 distinguishes between two different regimes: $\beta_2 > 0$ is said to be normal dispersion, where low frequencies lead in time while $\beta_2 < 0$ is anomalous dispersion, where high frequencies are ahead. For analytical purposes, the frame of reference can typically be selected as a frequency centered about ω_0 travelling with the pulse at the group velocity, thereby eliminating the zero and first order terms to begin at β_2 [10]. Another common quantity cited for fiber dispersion is D [ps/(nm km)], an alternate form of the group velocity dispersion:

$$D = -\frac{2\pi c}{\lambda^2}\beta_2 \tag{3.2}$$

where c is the speed of light and λ is the wavelength. Commercial silica fibers have D increasing with toward longer wavelengths such that $D < 0$ for wavelengths below approximately 1300 nm and becomes positive beyond this point. The wavelength where $D = 0$ is known as the "zero-dispersion wavelength". For more complex fiber structures, the zero-dispersion wavelength may be shifted, may not exist or there may exist multiple zero-dispersion wavelengths.

As mentioned in Section 2, the nonlinear response of a medium can be conceptualized as a power series in the electric field amplitude with coefficients $\chi^{(i)}$. As a glass, silica has an overall uniform distribution of atoms such that it can be considered centrosymmetric, therefore $\chi^{(2)} = 0$. However, this is not the case for $\chi^{(3)}$. An important quantity is the nonlinear index of refraction n_2, a correction to the usual index n_0 in the case of strong electric fields [30]:

$$n = n_0 + n_2|E|^2 \quad \text{where } n_2 = \frac{3}{4n_0^2\epsilon_0 c}\chi^{(3)} \tag{3.3}$$

where ϵ_0 is vacuum permittivity.

For silica, $n_2 \approx 3 \times 10^{-20}$ m^2/W. This effect leads to spectral broadening through self-phase modulation. Under initially unchirped conditions, a pulse will undergo a self-induced nonlinear phase shift ϕ_{NL}, causing variation of the instantaneous frequency within the pulse [10]. An additional time-dependent intrapulse nonlinear effect is the Raman response shown in Fig. 12. The model used for this will be presented in the following sections. For this initial derivation, we consider a scalar model which neglects effects such as cross-phase modulation and four-wave mixing. A more complete form will be given later when discussing polarization effects.

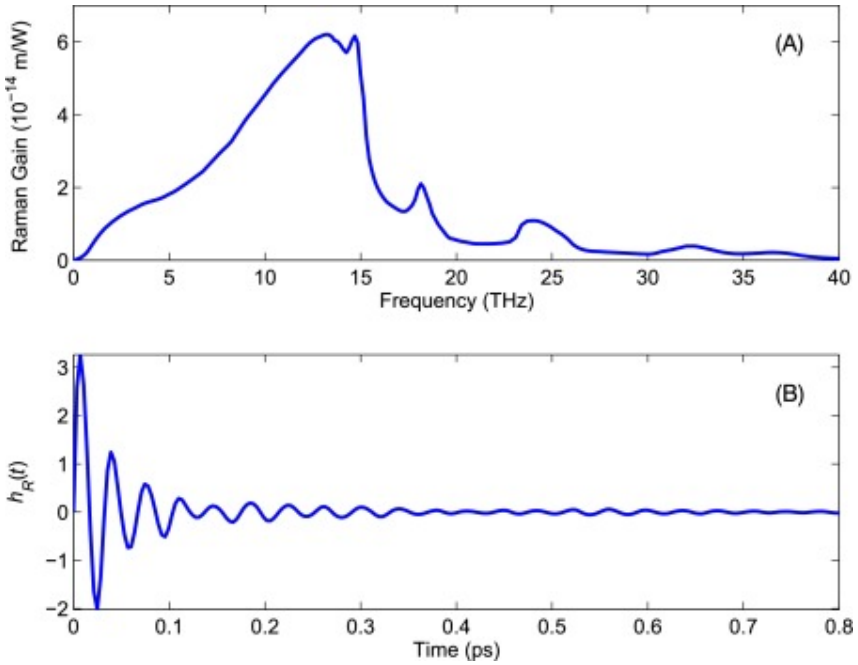

Figure 12: Raman gain spectrum (A) and associated temporal response (B). The response is usually modelled by fitting a damped sinusoidal function, sometimes incorporating non-oscillatory correction terms [10].

3.1 Generalized nonlinear Schrödinger equation

Fiber simulations solve a differential equation known as the generalized nonlinear Schrödinger equation (GNLSE) to map out the spectral and temporal evolution of a pulse during propagation [10, 30]. The slowly-varying pulse envelope is represented as $A(z,t)$ in the time domain, and its Fourier transform is $\tilde{A}(z, \omega - \omega_0)$. The function arguments will often be omitted for brevity. Beginning with the scalar form of the GNLSE, the typical equation to solve is:

$$\underbrace{\frac{\partial A}{\partial z} + \frac{\alpha}{2}A - \sum_{k\geq 2} \frac{i^{k+1}}{k!}\beta_k \frac{\partial^k A}{\partial t^k}}_{\text{Linear terms}} = \underbrace{i\gamma\left(1 + i\tau_{shock}\frac{\partial}{\partial t}\right)\left(A(z,t)\int R(t')|A(z,t-t')|^2 dt'\right)}_{\text{Nonlinear terms}} \tag{3.4}$$

where α is loss, β_k are dispersion coefficients, nonlinear coefficient is

$$\gamma = \frac{\omega_0 n_2}{c A_{eff}}, \tag{3.5}$$

in which ω_0 represents the angular carrier frequency of the light, n_2 is the aforementioned nonlinear refractive index, c the speed of light and A_{eff} is the effective area of the fiber mode.

The self-steepening term is proportional to $\tau_{shock} = \frac{1}{\omega_0}$, and the nonlinear response is modelled in time as

$$R(t) = (1 - f_R)\delta(t) + f_R h_R(t) \tag{3.6}$$

The weighting f_R determines the balance between Kerr and Raman nonlinear effects; δ is a Dirac delta to represent the instantaneous Kerr nonlinearity while the Raman contribution is approximated by:

$$h_R(t) = \frac{\tau_1^2 + \tau_2^2}{\tau_1 \tau_2^2} \exp(-t/\tau_2) \sin(t/\tau_1)\Theta(t) \tag{3.7}$$

with Θ as the Heaviside step function to respect causality [75]. The shorter timescale τ_1 determines the oscillatory response as illustrated in Fig. 12, while the τ_2 value sets the damping rate.

There are different numerical implementations that can be used to solve Equation 3.4, starting off with the split-step Fourier method. This technique considers the linear and nonlinear terms separately by splitting the propagation length into a sequence of small steps and alternately applying linear and nonlinear response at each step before advancing to the next [10]. This technique has the disadvantage of decoupling the dispersive and nonlinear parts of the GNLSE, which means that the step size must be very small to ensure accuracy. It also requires a call to an ordinary differential equation (ODE) solver for each step, which can become slow if the rate of evolution of the pulse spectrum is large, as in supercontinuum generation. It is also inefficient to try solving the full equation directly with an ODE solver [76].

For this reason, we adapted an alternate solution which transforms the entire GNLSE into the frequency domain and performs a variable change, thereby making the equation more readily solvable by numerical methods.

3.2 Transform to frequency domain

This procedure is defined in Ref. [75], and we have expanded and clarified their derivation. The definition of the Fourier transform $\mathcal{F}$ used is:

$$A(z,t) = \mathcal{F}^{-1}\left\{\tilde{A}(z, \omega - \omega_0)\right\} = \frac{1}{2\pi}\int \tilde{A}(z, \omega - \omega_0) \exp(-i(\omega - \omega_0)t) d\omega \tag{3.8}$$

$$\tilde{A}(z, \omega - \omega_0) = \mathcal{F}\{A(z,t)\} = \int A(z,t) \exp(i(\omega - \omega_0)t) dt \tag{3.9}$$

Note that it is conventional to work relative to pump frequency ω_0 for simulations, so while ω is the absolute frequency of the initial pulse, the transforms use $(\omega - \omega_0)$. Working through the terms of Equation 3.4, we obtain the following frequency-domain expressions for the spatial derivative and loss:

$$\mathcal{F}\left\{\frac{\partial A}{\partial z}\right\} = \int \frac{\partial A(z,t)}{\partial z} \exp(i(\omega - \omega_0)t) dt \tag{3.10}$$

$$= \frac{\partial}{\partial z}\int A(z,t) \exp(i(\omega - \omega_0)t) dt \tag{3.11}$$

$$= \frac{\partial \tilde{A}(z, \omega - \omega_0)}{\partial z} \tag{3.12}$$

$$\mathcal{F}\left\{\frac{\alpha}{2}A\right\} = \frac{\alpha}{2}\tilde{A}(z, \omega - \omega_0) \tag{3.13}$$

For the dispersion term, the time derivatives become frequency factors:

$$A(z,t) = \frac{1}{2\pi}\int \tilde{A}(z,\omega-\omega_0)\exp(-i(\omega-\omega_0)t)d\omega \tag{3.14}$$

$$\implies \frac{\partial A(z,t)}{\partial t} = \frac{\partial}{\partial t}\frac{1}{2\pi}\int \tilde{A}(z,\omega-\omega_0)\exp(-i(\omega-\omega_0)t)d\omega \tag{3.15}$$

$$= \frac{1}{2\pi}\int \tilde{A}(z,\omega-\omega_0)\frac{\partial}{\partial t}\exp(-i(\omega-\omega_0)t)d\omega \tag{3.16}$$

$$= \frac{1}{2\pi}\int \tilde{A}(z,\omega-\omega_0)\exp(-i(\omega-\omega_0)t)\cdot[-i(\omega-\omega_0)]d\omega \tag{3.17}$$

$$= \frac{1}{2\pi}\int \left[-i(\omega-\omega_0)\tilde{A}(z,\omega-\omega_0)\right]\exp(-i(\omega-\omega_0)t)d\omega \tag{3.18}$$

$$\implies \mathcal{F}\left\{\frac{\partial^k A}{\partial t^k}\right\} = [-i(\omega-\omega_0)]^k\,\tilde{A}(z,\omega-\omega_0) = [-i(\omega-\omega_0)]^k\,\mathcal{F}\{A\} \tag{3.19}$$

When summed over the full dispersion expansion, this leads to:

$$\mathcal{F}\left\{\sum_{k\geq 2}\frac{i^{k+1}}{k!}\beta_k\frac{\partial^k A}{\partial t^k}\right\} = \sum_{k\geq 2}\frac{i^{k+1}}{k!}\beta_k\,[-i(\omega-\omega_0)]^k\,\tilde{A}(z,\omega-\omega_0) \tag{3.20}$$

$$= \sum_{k\geq 2}\frac{(-1)^k i^{2k+1}}{k!}\beta_k(\omega-\omega_0)^k\tilde{A}(z,\omega-\omega_0) \tag{3.21}$$

Case by case: k even gives $(-1)^k i^{2k+1} = i$ since $2k+1 = 1,5,9,\ldots$; k odd gives $(-1)^k i^{2k+1} = (-1)(-i) = i$ since $2k+1 = 3,7,11,\ldots$

$$\mathcal{F}\left\{\sum_{k\geq 2}\frac{i^{k+1}}{k!}\beta_k\frac{\partial^k A}{\partial t^k}\right\} = i\sum_{k\geq 2}\frac{\beta_k(\omega-\omega_0)^k}{k!}\tilde{A}(z,\omega-\omega_0) \tag{3.22}$$

Having already worked out the expression for the transform of a time derivative, it is straightforward to simplify the nonlinear part of the equation as follows:

$$\mathcal{F}\left\{i\gamma\left(1+i\tau_{shock}\frac{\partial}{\partial t}\right)\left(A(z,t)\int R(t')|A(z,t-t')|^2dt'\right)\right\} \tag{3.23}$$

$$= i\gamma\left(1+i\tau_{shock}[-i(\omega-\omega_0)]\right)\mathcal{F}\left\{A(z,t)\int R(t')|A(z,t-t')|^2dt'\right\} \tag{3.24}$$

$$= i\gamma\left(1+\frac{(\omega-\omega_0)}{\omega_0}\right)\mathcal{F}\left\{A(z,t)\int R(t')|A(z,t-t')|^2dt'\right\} \tag{3.25}$$

$$= i\gamma\left(\frac{\omega}{\omega_0}\right)\mathcal{F}\left\{A(z,t)\int R(t')|A(z,t-t')|^2dt'\right\} \tag{3.26}$$

The frequency-domain GNLSE is therefore:

$$\frac{\partial\tilde{A}(z,\omega-\omega_0)}{\partial z} + \frac{\alpha}{2}\tilde{A} - i\sum_{k\geq 2}\frac{\beta_k(\omega-\omega_0)^k}{k!}\tilde{A} = i\gamma\left(\frac{\omega}{\omega_0}\right)\mathcal{F}\left\{A(z,t)\int R(t')|A(z,t-t')|^2dt'\right\} \tag{3.27}$$

The next step is a change in variables to combine the linear and nonlinear terms into a more compact expression. Define a linear operator $\hat{L}$ such that:

$$\hat{L} = -\frac{\alpha}{2} + i\sum_{k\geq 2}\frac{\beta_k(\omega-\omega_0)^k}{k!} \tag{3.28}$$

and define the new form of electric field amplitude $\tilde{A}'$ taking into account this operator:

$$\tilde{A}' = \tilde{A}\exp(-\hat{L}z) \tag{3.29}$$

Using this new $\tilde{A}'$ and the product rule, the spatial derivative can be developed:

$$\frac{\partial\tilde{A}(z,\omega-\omega_0)}{\partial z} = \frac{\partial}{\partial z}\left(\tilde{A}'\exp(\hat{L}z)\right) \tag{3.30}$$

$$= \frac{\partial\tilde{A}'(z,\omega-\omega_0)}{\partial z}\exp(\hat{L}z) + \tilde{A}'(z,\omega-\omega_0)\hat{L}\exp(\hat{L}z) \tag{3.31}$$

This leads to a final form given in Eq. 3.37 where the differential equation has been transformed into a product rather than a sum.

$$\frac{\partial\tilde{A}'(z,\omega-\omega_0)}{\partial z}\exp(\hat{L}z) + \tilde{A}'(z,\omega-\omega_0)\hat{L}\exp(\hat{L}z) - \hat{L}\tilde{A}(z,\omega-\omega_0) = \tag{3.32}$$

$$i\gamma\left(\frac{\omega}{\omega_0}\right)\mathcal{F}\left\{A(z,t)\int R(t')|A(z,t-t')|^2dt'\right\} \tag{3.33}$$

$$\frac{\partial\tilde{A}'(z,\omega-\omega_0)}{\partial z}\exp(\hat{L}z) + \tilde{A}'(z,\omega-\omega_0)\hat{L}\exp(\hat{L}z) - \hat{L}\tilde{A}'(z,\omega-\omega_0)\exp(\hat{L}z) = \tag{3.34}$$

$$i\gamma\left(\frac{\omega}{\omega_0}\right)\mathcal{F}\left\{A(z,t)\int R(t')|A(z,t-t')|^2dt'\right\} \tag{3.35}$$

$$\frac{\partial\tilde{A}'(z,\omega-\omega_0)}{\partial z}\exp(\hat{L}z) = i\gamma\left(\frac{\omega}{\omega_0}\right)\mathcal{F}\left\{A(z,t)\int R(t')|A(z,t-t')|^2dt'\right\} \tag{3.36}$$

$$\implies \frac{\partial\tilde{A}'(z,\omega-\omega_0)}{\partial z} = i\gamma\left(\frac{\omega}{\omega_0}\right)\exp(-\hat{L}z)\mathcal{F}\left\{A(z,t)\int R(t')|A(z,t-t')|^2dt'\right\} \tag{3.37}$$

This form of the GNLSE eliminates some of the numerical issues associated with ODE solvers and incorporates the full model rather than solving with only certain parts of the response at a time as with the split-step Fourier approach.

We can now look at a few results using this simulation equation implemented in Matlab with `ode45` [77].

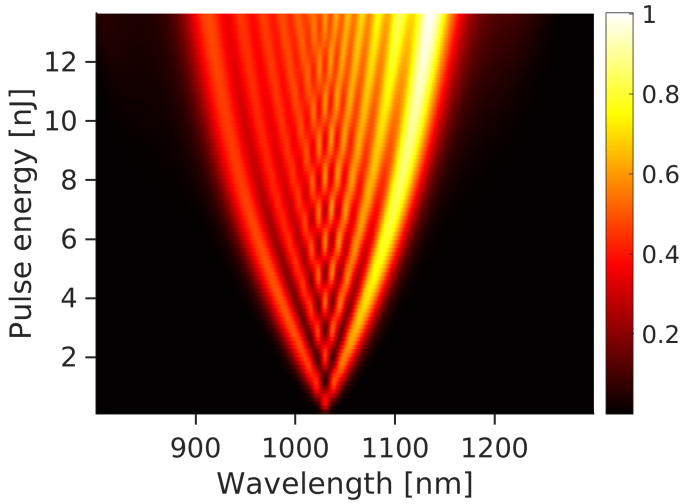

Figure 13: Example of spectral broadening as a function of input pulse energy for a 5 cm fiber with normal dispersion $\beta_2 = 0.015$ ps^2/m. The color scale is linear in this figure. Parameters are for a photonic crystal fiber to be discussed in Section 4 (see Table 2 for simulation parameters).

Figure 13 shows the effects of self-phase modulation as a function of input pulse energy on the spectrum of a Fourier transform-limited 180 fs Gaussian pulse. The color scale is linear and normalized to the most intense point on the surface. The spectrum broadens at the same rate on either side of the pump, gradually splitting into more and more distinct spectral peaks of approximately equal width. Using the same input conditions, we can select a fixed pulse energy to see how the nonlinear and dispersive effects impact the pulse over its propagation length.

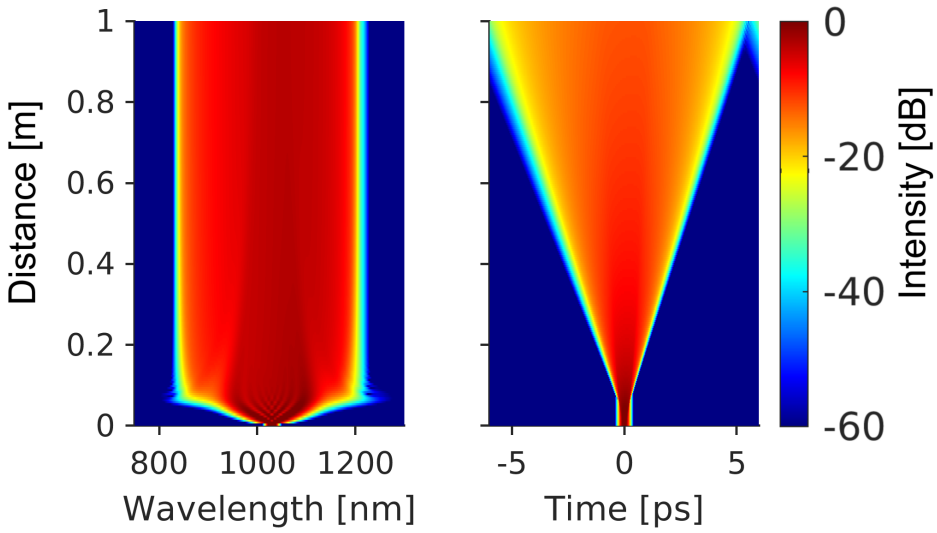

Figure 14: Logarithmic scale intensity for broadening of a 5.5 nJ input pulse under the same conditions as Fig. 13. The spectral broadening is shown on the left as a function of propagation length and on the right, the temporal profile of the pulse. Parameters are for a photonic crystal fiber to be discussed in Section 4.

Figure 14 shows the pulse spectrum and temporal profile as a function of propagation length in optical fiber, both on a logarithmic scale. Self-phase modulation dominates the first 5 cm of propagation as the spectrum undergoes nonlinear broadening. After this point, the spectral bandwidth no longer increases, but the dispersion of the fiber leads to spreading in the time domain. These two "phases" lead to the definition of two relevant length scales: L_{NL} the nonlinear length and L_D the dispersion length. These are defined according to [10]:

$$L_{NL} = \frac{1}{\gamma P_0} \tag{3.38}$$

$$L_D = \frac{T_0^2}{|\beta_2|} \tag{3.39}$$

where γ is the nonlinear coefficient (Eq. 3.5), P_0 is the peak optical power, T_0 is the input pulse duration and β_2 is the group velocity dispersion. For the case shown in Fig. 14, these can be estimated: The nonlinear coefficient used is

$$\gamma = \frac{(3\times10^{-20}\ \mathrm{m^2/W})(1.8\times10^{15}\ /\mathrm{s})}{(3\times10^{8}\ \mathrm{m/s})\pi(1.45\times10^{-6}\ \mathrm{m})^2} = 0.03\ \mathrm{m^{-1}W^{-1}} \tag{3.40}$$

and the peak power is $P_0 = (5.5\times10^{-9}\ \mathrm{J})/(180\times10^{-15}\ \mathrm{s}) = 30$ kW for a nonlinear length $L_{NL} = \left[(0.03\ \mathrm{m^{-1}W^{-1}})(18\times10^{3}\ \mathrm{W})\right]^{-1} = 1$ mm. Meanwhile, the dispersion length is $L_D = (180\times10^{-15}\ \mathrm{s})^2/(0.015\times10^{-24}\ \mathrm{s^2/m}) = 2$ m. These quantities highlight the difference in length

scales for linear vs. nonlinear effects and illustrate certain limits in which these contributions to the GNLSE may be considered somewhat independent as illustrated by the stages shown in Fig. 14. A final observation about the temporal broadening on the right hand panel concerns the top right corner where there is a continuation of the top left corner section. This wrapping effect can distort simulation results and is due to the cyclical properties of the numerical fast Fourier transform. It can be resolved by choosing temporal limits and step size carefully while considering the required limits in the frequency domain [78, 75].

Another phenomenon that can be reproduced in this type of simulation is the formation of Raman self-shifting solitons. Solitons are a solution to the GNLSE in regions of anomalous dispersion in which the nonlinear and dispersive material effects cancel, allowing the pulse to propagate while maintaining its temporal profile. In fiber, Raman effects contribute to the formation of a red-shifted peak approximately 13 THz away from the pump, the location of maximum gain in Fig. 12 [10]. If this part of the spectrum lies in a region of anomalous dispersion, it can become a soliton. The continued Raman excitation amplifies the lower-frequency part of the soliton spectrum, creating a continued red-shift [79]. In the frequency domain, Raman solitons appear as peaks which red-shift over their propagation length. They can be seen as narrow peaks delayed with respect to the pump in the time domain. Solitons can also transfer energy to spectral components on the blue end of the spectrum in the form of phase-matched dispersive waves [10]. This will be illustrated later.

3.3 Polarization-resolved supercontinuum experiment

An experimental observation made when studying polarization properties of a supercontinuum generated in a germania-doped photonic crystal fiber (PCF) led us to expand the simulation from a scalar GNLSE to a pair of coupled GNLSEs (CGNLSEs) for two polarization states [11]. Analysis of this supercontinuum under study in the lab showed interesting polarization dynamics as a function of input polarization state and optical power which the scalar GNLSE model for spectral broadening could not replicate. To better understand what effects might cause the measured results, we created a vector form of the fiber simulation. The experiment and simulation became their own project, not directly related to THz detection, but the extended CGNLSE model nonetheless serves to enhance general understanding of fiber optics and provides options for more in depth analysis of spectral broadening processes.

In this experiment, a linearly polarized pulsed laser beam with variable power and polarization angle travels through 0.8 m of PCF with a zero-dispersion wavelength of 1047 nm, close to the center laser wavelength $\lambda_0 = 1030$ nm. The 50 mol% germania core composition of the fiber and the presence of capillary structures increase the refractive index contrast between core and cladding to enhance mode confinement within the core, leading to a high nonlinear coefficient. The zero-dispersion wavelength near to the pump wavelength allows better phase matching for spectral broadening processes such as the generation of Raman solitons and four-wave mixing [78]. These properties in combination with the laser system in the lab make this fiber a good candidate for studying supercontinuum generation.

In Fig. 15, the experimental configuration is shown. A half wave plate and polarizer control the optical power delivered to the fiber and another half wave plate adjusts the polarization angle. At the fiber output, the generated supercontinuum spectrum is measured using a monochromator system equipped with three different gratings for measurements between 400 and 5000 nm. An ultrabroadband polarizer controls the polarization basis for these spectral measurements. In practice, the monochromator grating response is given for two orthogonal polarization states

oriented horizontally and vertically in the lab frame of reference, so we use these as a polarization basis for the measurements. We also locate the principal axes of the PCF and placed it so that at the fiber output, they aligned with these horizontal and vertical references as well. All of the optics in the beam path from fiber output to detector have wavelength-dependent reflection/transmission, responses which have been taken into account in normalizing the measured spectra.

The aforementioned principal axes of an optical fiber are its fast and slow birefringence axes. During fabrication, these can be carefully engineered by forming an elliptical core or inserting stress rods within the cladding to craft a polarization-maintaining fiber. However, in optical fiber designed to have a uniform cross-section, the circular symmetry is broken randomly along the fiber length by small defects or variations in stress within the glass. In this case, the definition of principal axes is extended to refer to an orthogonal pair of axes which preserve a linear polarization state [80]. These can be found by imaging the fiber tip, monitoring optical phase differences, or using interferometric techniques [81]. We rotated the input polarization state at low optical power to find the angles (θ in Fig. 16) resulting in a linearly polarized output. We also placed the output end of the fiber in a rotation mount and oriented it such that the principal axes were horizontal (H) and vertical (V) in the lab frame at that point.

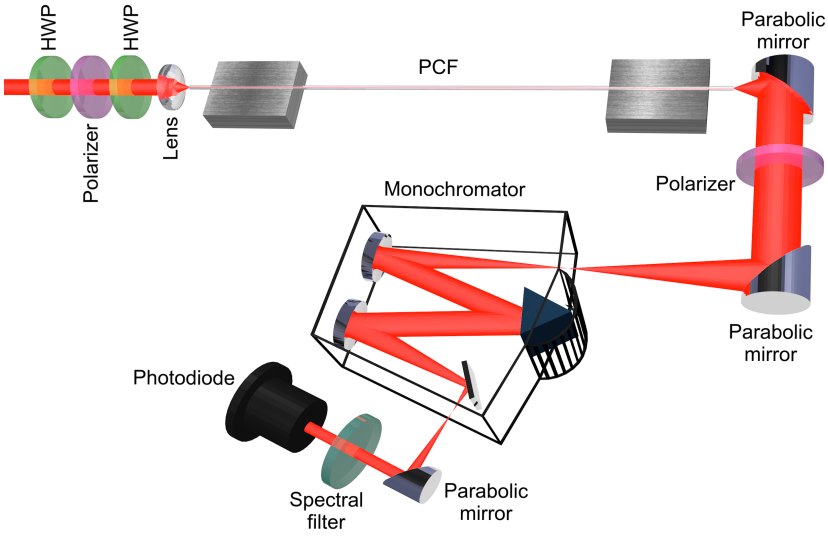

Figure 15: Experimental setup used in [11]. The input at top left is the output from a Yb:KGW ultrafast laser centered at 1030 nm with a 180 fs pulse duration. The first half wave plate (HWP) and polarizer control the input power, and the second HWP sets the linear input polarization state. The beam is coupled into the PCF under study, and the output spectrum is characterized with the monochromator system using an orthogonal polarization basis determined by the second polarizer. After the fiber output, off-axis parabolic mirrors are used for imaging to reduce chromatic aberrations.

With this layout, we vary the angle of the linear input polarization state to observe the effects on spectral broadening as shown in Fig. 16. The surface plots (a, b, d, e) represent the log scale spectral power as a function of wavelength and input polarization angle. The input angles $\theta = 0°$ and $\theta = 90°$ correspond to the principal axes of the fiber. Panels a, b and c are measurements for an input pulse energy of 0.35 nJ while panels d, e and f show the same measurements repeated at 1.1 nJ. Already at 1.1 nJ the spectrum has broadened significantly to span up to 500 nm through self-phase modulation and the formation of a Raman soliton and dispersive wave pair

[79, 78].

The quantity in Fig. 16c and f is called the degree of polarization, in this case defined as

$$DOP(\mathcal{R}) = \frac{|P_V(\mathcal{R}) - P_H(\mathcal{R})|}{P_V(\mathcal{R}) + P_H(\mathcal{R})} \tag{3.41}$$

where P_V is the optical power measured in the vertical polarization state and P_H is the optical power measured in the horizontal polarization state. $\mathcal{R}$ denotes a spectral band of interest, which can range from monochromatic (single wavelength point) to the full spectrum, allowing us to consider global polarization dynamics if $\mathcal{R}$ is a broad band, or small-scale features by using narrower regions. In Fig. 16, $\mathcal{R}$ is the full spectrum, showing that when aligned to one of the principal axes, 95% of the total power remains in that polarization state at the output ($DOP = 0.9$).

Consistent with previous observations, we find that spectral features such as the Raman soliton or dispersive wave present in one principal axis appear uncoupled with those in the other axis and that the broadest supercontinuum spectrum is obtained with an input polarization state aligned to a principal axis [82]. This input condition is hypothesized to result in a total output spectrum that is a linear combination of the independent H and V spectra, each with energy proportional to the projection from the input polarization state onto that axis [83]. This assumption is a realistic approximation for the case of a highly-birefringent fiber, since the fast and slow components become separated in time and no longer interact. However, the PCF used in these experiments has quite low birefringence on the order of 10^{-6}.

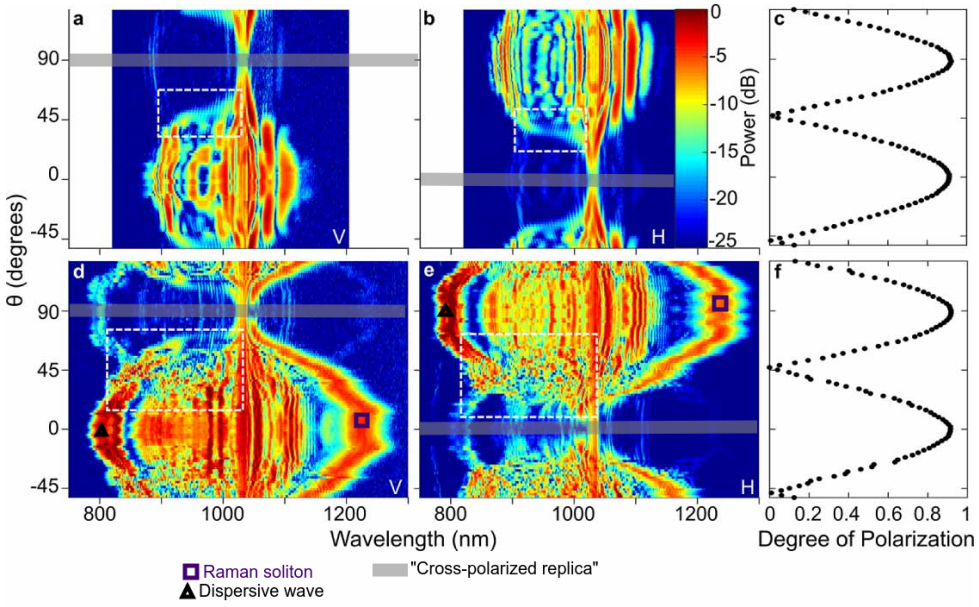

Figure 16: Polarization dependence of supercontinuum generation at low power. Top row: input pulse energy 0.35 nJ. Bottom row: input pulse energy 1.1 nJ. a),d) Vertically (V) polarized spectrum as a function of input polarization angle; b),e) Horizontally (H) polarized spectrum as a function of input polarization angle; c),f) The degree of polarization based on overall spectrum power distribution per axis [11].

The imperfect degree of polarization caught our attention in these results. We attribute the residual trace of the more intense cross-polarized spectrum (e.g. at 90° in a or d) to output coupling, a result of mechanical stress in the v-groove mount used to secure the fiber input. In

tests with an alternate clamping system consisting of magnets instead of glue, the cross-polarized replica was three times larger. This signal accounts for 2% of the total intensity, leaving 3% having depolarized during propagation within the fiber or during in-coupling. We expect that the polarization should be well preserved, but even with alignment to a principal axis there is a non-negligible intensity in the orthogonal state.

Next, we select the input angle $\theta = 0°$ and vary the input pulse energy to generate the two-octave supercontinuum in Fig. 17. The spectrum in V corresponds to the polarization state matching the input while H is the cross-polarized measurement. With increasing power, solitons break off toward longer wavelengths, extending the spectrum into the infrared with corresponding dispersive waves broadening to shorter wavelengths. Four wave mixing, phase matched for a pump near the zero-dispersion wavelength, also contributes to spectral broadening for pulses of this time duration [78]. The most intense region is toward the visible, where the power level reaches approximately an order of magnitude higher than rest of the spectrum. The H measurement at low pulse energies follows the trends in Fig. 16 for $\theta = 0°$ with intensity concentrated at the pump and a faint copy of V. With increasing pulse energy, nonlinear spectral broadening mechanisms occur independently in the H polarization state as indicated by the Raman solitons in the inset of panel b at 5 and 25 nJ.

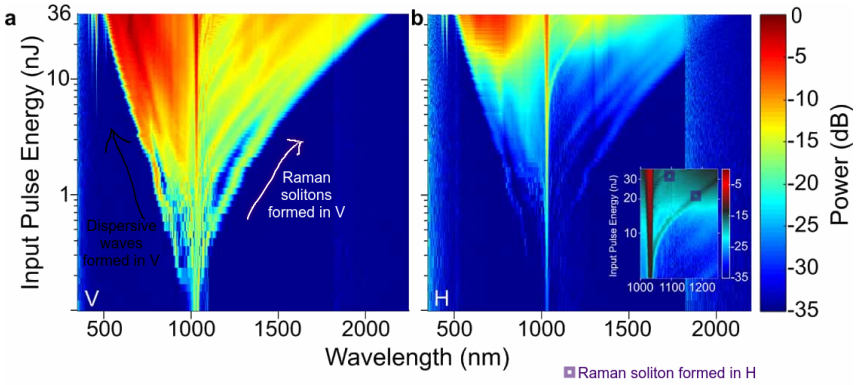

Figure 17: Spectra measured in a) vertical and b) horizontal polarization states as a function of input pulse energy for linear polarization $\theta = 0°$ at input (see Fig. 16). Inset in b) is a zoom on part of b) shown in a different colour scale to better show the Raman solitons breaking away from the pump [11].

The DOP over the full spectrum is stable up to a pulse energy of 10 nJ; above this threshold the DOP begins to drop from 0.9 to 0.4 at the top pulse energy of 36 nJ. This is shown in the Fig. 18a line identified SC and indicates that 30% of the total output power is found in the polarization state orthogonal to the original input beam. The other lines indicate that the DOP at the pump wavelength is stable near 0.5 across all pulse energies while the power redistribution from V to H occurs at lower pulse energies for shorter vs. longer wavelengths. The fine depolarization trends can be seen in the surface plot in b. We notice that at pulse energies above 20 nJ, the lowest DOP region is to the right of the pump due to an intense soliton in H causing the intensities in V and H to reach the same level locally. On the other hand, the blue-shifted side of the spectrum has a DOP consistently below 0.6, compared to the longer wavelengths which, past 1500 nm conserve a DOP well above 0.6. This suggests a depolarization process acting preferentially on shorter wavelengths. Panels c and d show cross sections of spectral intensity and DOP at the highest pulse energy. As mentioned previously, the generation of solitons and dispersive waves occurs independently in each principal axis, and these features continue to red- and blue-shift

respectively during propagation. We hypothesize that this is the reason for the higher DOP at the edges of the spectrum–these components are generated only in the V axis toward the end of the propagation length and have little distance over which to depolarize.

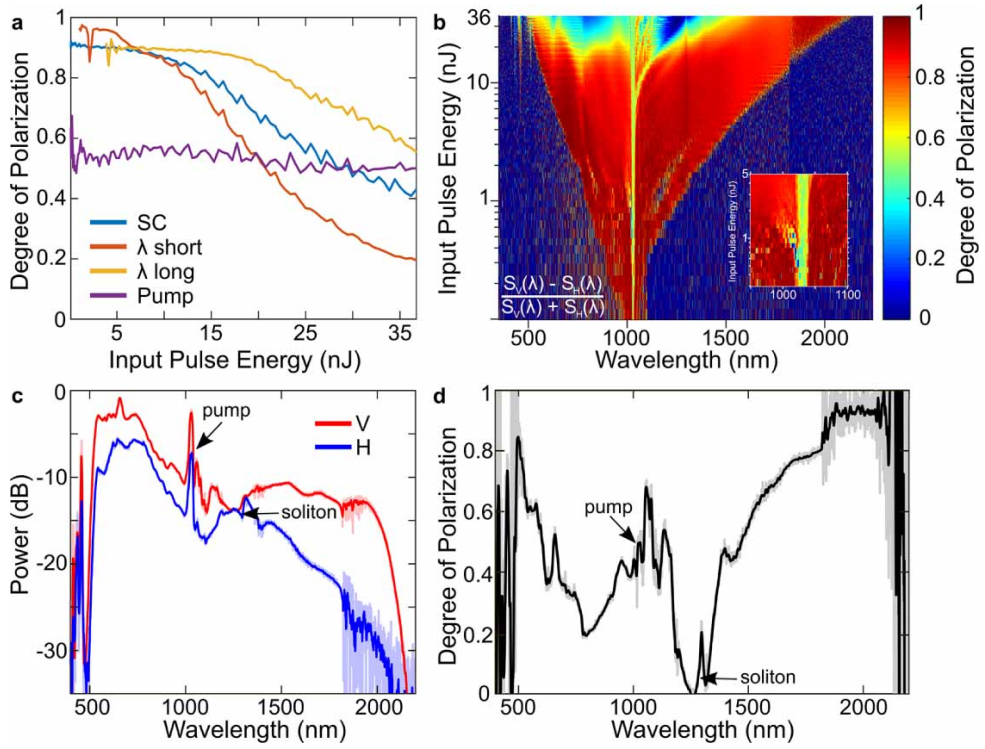

Figure 18: a) The degree of polarization for four different spectral regions: full supercontinuum (SC), 795 to 805 nm (λ short), 1495 to 1505 nm (λ long) and an 8 nm band at the pump. b) Wavelength-dependent DOP as a function of pulse energy. c) Log scale spectra at the highest pulse energy with highlighted spectral features. d) Wavelength-dependent DOP associated to spectra from c. Paler colours are raw data; dark have had smoothing applied [11].

From these experiments, we can establish that depolarization effects are both wavelength- and pulse energy-dependent. Specific trends that we observe include an apparent pulse energy threshold for overall depolarization, the best preserved polarization state at the longest wavelength edge of the spectrum and highly depolarized regions on either side of the pump. Previous experimental and theoretical studies have found a power threshold above which nonlinear depolarization overcomes intrinsic polarization maintaining ability from birefringence [84, 85, 86, 87, 88, 89]. One explanation for this effect is polarization modulation instability which can manifest in the noise-seeded transfer of intensity to an orthogonal polarization mode at two gain peaks localized symmetrically on either side of the pump frequency [90, 91]. Intrinsic and unintentional birefringence from fabrication and handling are known to impact the polarization state during supercontinuum generation, allowing polarization maintaining propagation for low powers but more complex depolarization dynamics at high power as the nonlinear refractive indices may overcome the small intrinsic birefringence [10, 89, 92, 93, 84]. Cross-phase modulation is another potential explanation for depolarization effects without a threshold–the nonlinear index of refraction originating from the $\chi^{(3)}$ susceptibility tensor couples the two orthogonal polarization modes and causes a phase shift proportional to the input pulse intensity [94]. In order for this to occur, there must be some initial intensity in the state orthogonal to the input, hypothesized to occur from scattering at the input fiber tip [94, 95]. Cross-phase modulation can also contribute in the scalar case: as spectral components are generated and shift in time according to

the dispersion profile of the fiber, they may come to interact in time. This is the case between Raman solitons and dispersive waves, and can lead to the the generation of higher frequency components at the edge of the spectrum [96]. This may be the origin of the peaks seen near 500 nm in Fig. 17a. It has been shown that the edges of supercontinuum spectra tend to have higher polarization stability than near the pump [97]. Other references have suggested that solitons generated in optical fiber conserve a higher degree of polarization than other spectral features, which could be a clue as to the high degree of polarization at the long wavelength end of our measured spectra [98, 97].

In order to better understand the different mechanisms at play in our experiments, we extend the scalar GNLSE simulations to take into account polarization dynamics. We hypothesize that a linear effect such as scattering acts as a source for nonlinear depolarization since polarization modulation instability and cross-phase modulation, two of the most frequently discussed causes of depolarization across supercontinuum spectra, both require an initial noise seed or non-zero cross-polarized component [10, 90].

3.4 Coupled generalized nonlinear Schrödinger equations

We incorporate a linear polarization mode-coupling model into an extended form of the coupled generalized nonlinear Schrödinger equations (CGNLSEs) [10]. The linear polarization mode-coupling model is given in the frequency domain, after translation into the convention used in the previous sections, by [92]:

$$\frac{\partial \tilde{A}_x}{\partial z} = i\beta_x \tilde{A}_x + \epsilon \tilde{A}_y \tag{3.42}$$

$$\frac{\partial \tilde{A}_y}{\partial z} = i\beta_y \tilde{A}_y - \epsilon^* \tilde{A}_x \tag{3.43}$$

These equations are similar to Eq. 3.27, the frequency domain GNLSE, but they have a far simpler form of the propagation equation with only dispersion and an exchange of energy between x and y polarization states. The factor ϵ [m^{-1}], which can be complex, represents an average deformation rate in the fiber as a way to take into account slight manufacturing defects and the ensuing depolarization effects [92]. This model leads to a polarization rotation on top of the beat length associated with intrinsic birefringence. It is perhaps misleading to call this linear polarization mode coupling as the original authors do since one might expect this to indicate that intensity is exchanged between both modes simultaneously so that they end up with similar output spectra. Rather, the intensity is transferred in a continuous rotation. However, despite its simplicity the theory does accurately predict a $|cos(2\theta)|$ dependence for Fig. 16c and f. It has the added benefit of integrating readily into a GNLSE. The other β_x (β_y) term denotes the dispersion properties for the x (y) principal axis of the fiber. In practice, this is represented by a polynomial expansion of the form seen in Eq. 3.27 such that:

$$\beta_i \tilde{A}_i = \sum_{k\geq 2} \frac{\beta_{k,i}(\omega - \omega_0)^k}{k!} \tilde{A}_i \tag{3.44}$$

Equations 3.42, 3.43 can naturally be integrated into CGNLSEs containing nonlinear terms. We

used the most general form we could find, resulting in the following pair of equations [10, 84, 97]:

$$\frac{\partial A_x}{\partial z} + \frac{\alpha_x}{2}A_x + \frac{\Delta\beta}{2}\frac{\partial A_x}{\partial t} - \sum_{k\geq 2}\frac{i^{k+1}}{k!}\beta_{k,x}\frac{\partial^k A_x}{\partial t^k} - \epsilon A_y$$
$$= i\gamma\left(1 + i\tau_{shock}\frac{\partial}{\partial t}\right)\left\{(1-f_R)\left[A_x\left(|A_x|^2 + \frac{2}{3}|A_y|^2\right) + \frac{i\gamma}{3}A_x^* A_y^2 e^{-2i\Delta\beta z}\right] + f_R R_x\right\} \quad (3.45)$$

$$\frac{\partial A_y}{\partial z} + \frac{\alpha_y}{2}A_y - \frac{\Delta\beta}{2}\frac{\partial A_y}{\partial t} - \sum_{k\geq 2}\frac{i^{k+1}}{k!}\beta_{k,y}\frac{\partial^k A_y}{\partial t^k} + \epsilon^* A_x$$
$$= i\gamma\left(1 + i\tau_{shock}\frac{\partial}{\partial t}\right)\left\{(1-f_R)\left[A_y\left(|A_y|^2 + \frac{2}{3}|A_x|^2\right) + \frac{i\gamma}{3}A_y^* A_x^2 e^{-2i\Delta\beta z}\right] + f_R R_y\right\} \quad (3.46)$$

For a detailed derivation and discussion of these equations, see reference [10], chapter 6 in particular. The final Raman response term is given by:

$$R_x = A_x\int h_R^{new}(t')|A_x(z,t-t')|^2 dt' + f_a A_x\int h_a(t')|A_y(z,t-t')|^2 dt'$$
$$+ \frac{f_b}{2}A_y\int h_b(t')\left[A_x(z,t-t')A_y^*(z,t-t') + A_x^*(z,t-t')A_y(z,t-t')e^{-2i\Delta\beta z}\right]dt' \quad (3.47)$$

for x, and interchanging the x and y indices gives the equivalent equation for y. The Raman response model also includes an extra non-oscillatory term compared with Eq. 3.4 [10].

$$h_R^{new} = f_a h_a + f_b h_b \quad (3.48)$$
$$h_a = \frac{\tau_1^2 + \tau_2^2}{\tau_1\tau_2^2}\exp(-t/\tau_2)\sin(t/\tau_1)\Theta(t) \quad (3.49)$$
$$h_b = \frac{2\tau_b - t}{\tau_b^2}\exp(-t/\tau_b)\Theta(t) \quad (3.50)$$

It is worth noting that good results are often obtained even when neglecting the $A_i^* A_j^2 e^{-2i\Delta\beta z}$ term in the instantaneous response and the cross terms in R_i in Eq. 3.45 and 3.46 [99].

From this point, it's necessary to bring the new propagation equations into the same format as Eq. 3.37. Here, the process is shown with Eq. 3.45 for reference. The equation must first be transformed into the frequency domain:

$$\frac{\partial\tilde{A}_x}{\partial z} + \frac{\alpha_x}{2}\tilde{A}_x - i\frac{\Delta\beta}{2}(\omega-\omega_0)\tilde{A}_x - i\sum_{k\geq 2}\frac{\beta_{k,x}(\omega-\omega_0)^k}{k!}\tilde{A}_x - \epsilon\tilde{A}_y$$
$$= i\gamma\left(\frac{\omega}{\omega_0}\right)\mathcal{F}\left\{(1-f_R)\left[A_x\left(|A_x|^2 + \frac{2}{3}|A_y|^2\right) + \frac{i\gamma}{3}A_x^* A_y^2 e^{-2i\Delta\beta z}\right] + f_R R_x\right\} \quad (3.51)$$

The linear operators become axis-dependent:

$$\hat{L_x} = -\frac{\alpha_x}{2} + i\sum_{k\geq 2}\frac{\beta_{k,x}(\omega-\omega_0)^k}{k!} + i\frac{\Delta\beta}{2}(\omega-\omega_0) \quad (3.52)$$
$$\hat{L_y} = -\frac{\alpha_y}{2} + i\sum_{k\geq 2}\frac{\beta_{k,y}(\omega-\omega_0)^k}{k!} - i\frac{\Delta\beta}{2}(\omega-\omega_0) \quad (3.53)$$

If known, the values for axis-dependent loss α_i and dispersion $\beta_{k,i}$ can be included along with the birefringence $\Delta\beta$ between them. The variables get changed again to the $\tilde{A}'$ form using their respective linear operators.

$$\tilde{A_x}' = \tilde{A_x} \exp(-\hat{L_x} z) \tag{3.54}$$

$$\tilde{A_y}' = \tilde{A_y} \exp(-\hat{L_y} z) \tag{3.55}$$

Carrying on from Eq. 3.51, the equation can be simplified to a form that is convenient to implement numerically.

$$\begin{aligned} &\frac{\partial \left(\tilde{A_x}' \exp(\hat{L_x} z) \right)}{\partial z} - \hat{L_x} \left(\tilde{A_x}' \exp(\hat{L_x} z) \right) - \epsilon \left(\tilde{A_y}' \exp(\hat{L_y} z) \right) \\ &\quad = i\gamma \left(\frac{\omega}{\omega_0} \right) \mathcal{F} \left\{ (1 - f_R) \left[A_x \left(|A_x|^2 + \frac{2}{3} |A_y|^2 \right) + \frac{i\gamma}{3} A_x^* A_y^2 e^{-2i\Delta\beta z} \right] + f_R R_x \right\} \end{aligned} \tag{3.56}$$

$$\begin{aligned} &\frac{\partial \tilde{A_x}'}{\partial z} \exp(\hat{L_x} z) - \epsilon \left(\tilde{A_y}' \exp(\hat{L_y} z) \right) \\ &\quad = i\gamma \left(\frac{\omega}{\omega_0} \right) \mathcal{F} \left\{ (1 - f_R) \left[A_x \left(|A_x|^2 + \frac{2}{3} |A_y|^2 \right) + \frac{i\gamma}{3} A_x^* A_y^2 e^{-2i\Delta\beta z} \right] + f_R R_x \right\} \end{aligned} \tag{3.57}$$

$$\begin{aligned} \implies \frac{\partial \tilde{A_x}'}{\partial z} &= \epsilon \tilde{A_y}' \exp\left((\hat{L_y} - \hat{L_x}) z \right) \\ &+ i\gamma \left(\frac{\omega}{\omega_0} \right) \exp(-\hat{L_x} z) \mathcal{F} \left\{ (1 - f_R) \left[A_x \left(|A_x|^2 + \frac{2}{3} |A_y|^2 \right) + \frac{i\gamma}{3} A_x^* A_y^2 e^{-2i\Delta\beta z} \right] + f_R R_x \right\} \end{aligned} \tag{3.58}$$

We updated Matlab code to solve Eq. 3.58 coupled with the equivalent equation in y. The input pulse is projected on the principal axes at an angle θ with respect to the x axis.

In order to verify that the results make sense, the first step is to see if they are consistent with the scalar case when the polarization state is aligned to a principal axis. This is shown in Fig. 19. For this initial simulation, the linear coupling model is neglected by setting $\epsilon = 0$. The parameters in this simulation were tuned to closely match the experimental supercontinuum bandwidth using the measured dispersion curve and estimated nonlinear response for 50 mol% germania doping in the core (see Table 2 for parameters). Fiber loss is neglected ($\alpha = 0$). The two principal axes are assumed to have the same dispersion properties as the measurement was only performed in one polarization state and the estimated birefringence is quite low, suggesting that the two principal axes should not be substantially different. This is also supported by the similar spectra between principal axes in Fig. 16. We see that the x results for $\theta = 0°$ in the CGNLSE simulation are nearly identical to the scalar case, indicating that this vector model is a good extension of the original framework developed in [75]. At $\theta = 0°$, the y spectrum is at the level of the noise floor, which was included to provide a non-zero seed in both polarization states for potential modulation instability. The y signal does rise above the level of the noise floor for $\theta = 1°, 5°$. For reference, the wavelength-dependent DOP at 5 nJ for each input angle is presented below the spectra, showing that only at $\theta = 5°$ does a drop in DOP near the pump become evident.

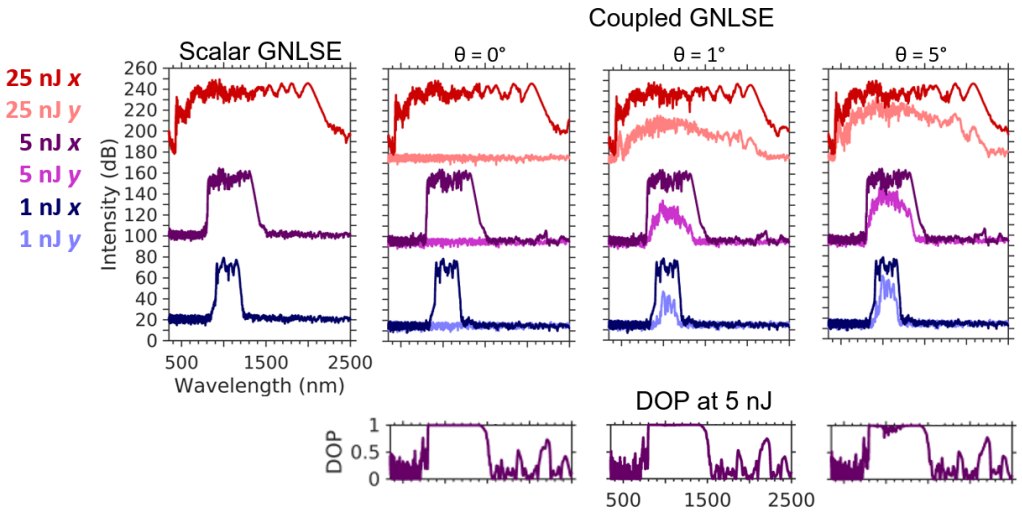

Figure 19: Comparison of scalar GNLSE with coupled equation x, y solutions for three input angles $\theta = 0°, 1°, 5°$ at pulse energies 1, 5 and 25 nJ. Below, the DOP across the 5 nJ spectra for each input angle. The linear coupling coefficient ϵ is zero. Spectral resolution is 2 nm.

We fix an input angle of $\theta = 1°$ to mimic experimental uncertainty and proceed to consider different depolarization contributions in Fig. 20. The labels indicate the type of depolarization effect included in the simulation. The "nonlinear" simulation is the same as in Fig. 19, with $\epsilon = 0$. It solves equation 3.58 and the corresponding differential equation in y. The "linear" simulation sets $\epsilon = -0.23$ m^{-1} which corresponds to 4% depolarization after 1 m propagation if neglecting nonlinear effects, consistent with experimental depolarization fraction attributed to propagation as discussed in the context of Fig. 16. It also neglects all nonlinear terms which couple x and y, leaving only the scalar Kerr and Raman terms which do not contribute to depolarization. Finally, the column entitled "both" uses the full vector nonlinear model in equation 3.58 with $\epsilon = -0.23$ m^{-1}. The nonlinear model alone does not result in decrease in DOP as shown by the DOP curve on the right. However, the linear model does cause a dip in the DOP near the pump and at the short wavelength end of the spectrum. With both linear and nonlinear depolarization, these trends are further emphasized. This indicates that the inclusion of a linear polarization rotation model likely acts as a seed for the nonlinear redistribution of intensity among polarization states. These trends are also consistent with experimental observations made above regarding DOP being lowest toward the middle of the spectrum and highest at the long wavelength edge.

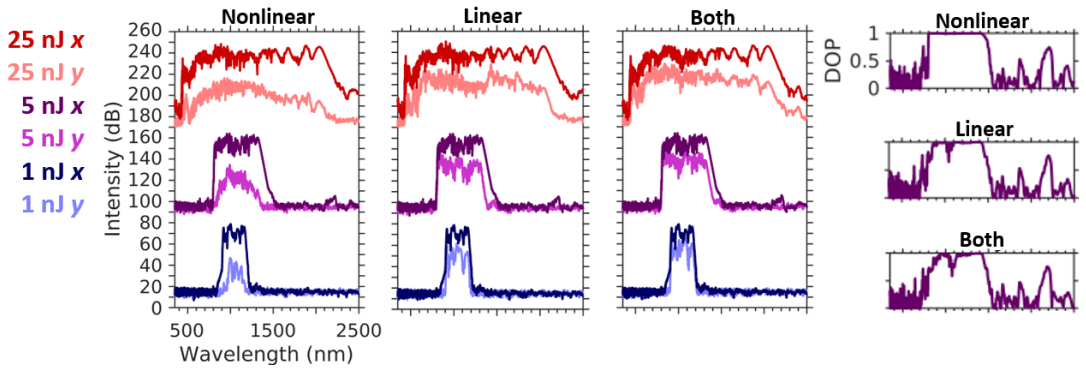

Figure 20: At $\theta = 1°$, comparison of linear and nonlinear depolarization mechanisms in CGNLSEs. Note that the linear vs. nonlinear distinction applies only to the depolarization or polarization coupling mechanisms - each principal axis retains its scalar GNLSE mechanisms.

The same type of simulation is repeated in Fig. 21 but with an increased linear coupling coefficient $\epsilon = 0.6$ m^{-1}. Again, the linear coupling alone causes some depolarization, but it is the effect of the linear coupling term combined with nonlinear cross terms that brings the DOP more in line with our experimental observations. Interestingly, most of the spectral broadening occurs in the first 10 cm of propagation apart from a continued red-shift of Raman solitons. This confirms the hypothesis that the most depolarized regions of the spectrum are among those generated earliest during propagation.

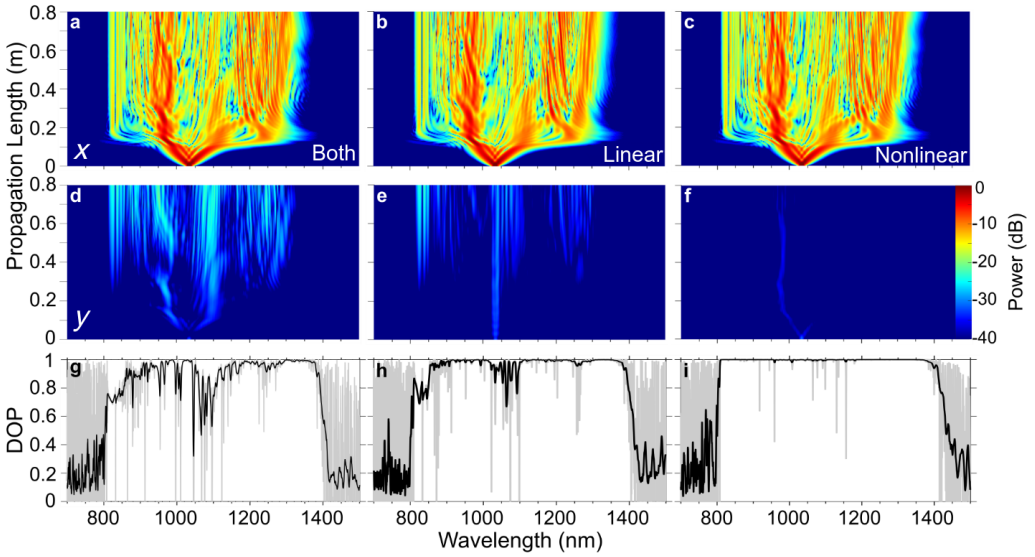

Figure 21: Spectra in x and y as a function of propagation distance for a pulse energy of 5 nJ. Similar to Fig. 20 with ϵ increased to 0.6 m^{-1} to show spectral broadening along the fiber length.

Finally, we can also look at the pulse energy dependence of spectral broadening in Fig. 22. As the pulse energy increases, the effective broadening length decreases from 50 cm to reach the full bandwidth at 1 nJ down to approximately 5 cm at 25 nJ. The regions most susceptible to depolarization remain the pump and shorter wavelengths. However, the pulse energy threshold for overall depolarization observed in experiment is not reproduced in these simulations. Other studies have found thresholds above which polarization is no longer maintained in simulations using similar models, but often with a circular basis instead of the linear xy polarization basis

used here [84].

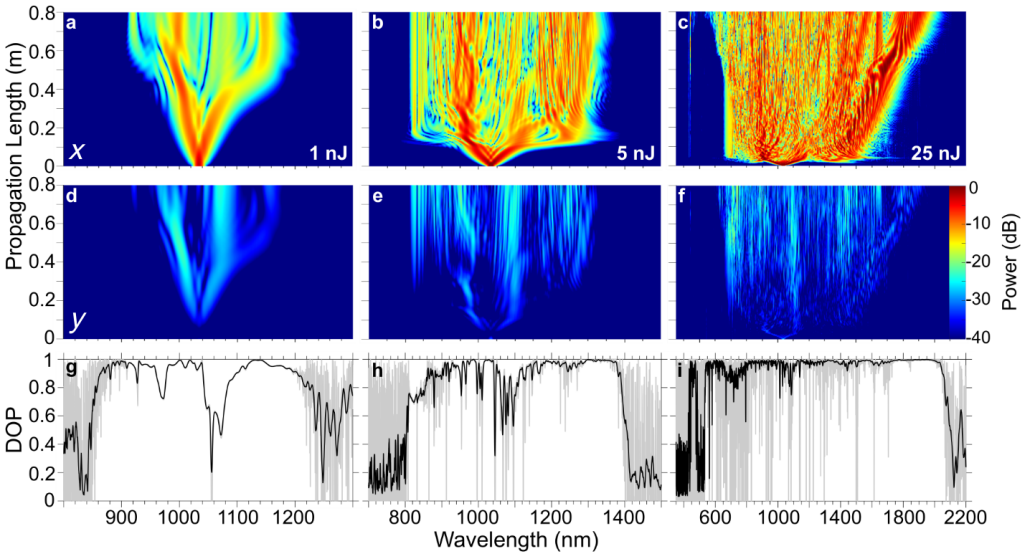

Figure 22: Spectral broadening as a function of propagation length for pulse energies 1, 5 and 25 nJ. Same as Fig. 21 in the "both" case.

The model used could be extended to take into account more principal axis-dependent properties including dispersion or differential loss. The nonlinear response and effective mode area could be improved by making them frequency dependent. Further simulation work on the temporal and coherence properties of supercontinuum generation may be interesting to determine whether these spectra have the potential to be compressed back to transform-limited pulses. Analysis of spectrograms could be used to show which frequency components interact in time during propagation to generate new ones. From a technical point of view, it could be worthwhile to compare these results to their split-step Fourier equivalents to see if the numerical implementation has an impact on the trends we observe. The current formulation tends to run more quickly due to the single ode solver call and adaptive step size. Lastly, though mathematically equivalent, it would be good to check if the CGNLSEs in a circular basis yield the same results under numerical integration. Despite the limitations of the current implementation, it helps to more accurately assess polarization maintaining capability by showing the regions of the spectrum most likely to experience polarization degradation. The supercontinuum research work was largely exploratory at the start, but ultimately allowed us to better understand fiber optic modelling to improve simulations for other projects, including the one described in the following section. The comparison between "linear" and "nonlinear" depolarization models yields results that qualitatively agree with many of our experimental observations and trends, allowing us to conclude that both models are factors contributing to depolarization.

4 Single-pulse terahertz detection experiment

The technique described here is referred to as "single-pulse" rather than "single-shot" to distinguish it from previous techniques in Section 2.3 and to emphasize that this technique truly does offer the opportunity to record every pulse at high repetition rates by streaming data continuously with no minimum detector integration time.

This section is an overview of the steps taken to implement a new THz detection technique which combines spectral encoding on a fiber-broadened, chirped probe with the dispersive Fourier transform. We present the laser system and THz generation scheme, then go through the alignment and characterization of the probe beam as it undergoes shaping in the time and frequency domains.

Figure 23 is a schematic illustration of the technique. Starting at left, the laser beam is split two ways, with most of the intensity going toward generating THz pulses. The remaining intensity is used for detection. The detection beam travels through a photonic crystal fiber (PCF) to create a broader spectrum, then passes through a double grating stretcher to disperse the pulses in time. This results in a broadband, chirped pulse with a duration on the order of the duration of a THz pulse. The detection beam is divided between two paths, one of which interacts with the THz pulse via the Pockels effect in a nonlinear crystal. This serves to map the time-varying THz electric field into the frequency domain of the detection pulse. The THz-modulated and unmodulated copies of the detection pulse are overlapped in time and space and travel through a 5 km commercial optical fiber to perform a dispersive Fourier transform (DFT). DFT is the time-stretch effect in which the frequency-dependent refractive index of an optical fiber plays the role of a high-speed spectrometer, spreading the spectral components of the probe pulse in time rather than in space. The resulting interference pattern will be used to determine the applied THz field.

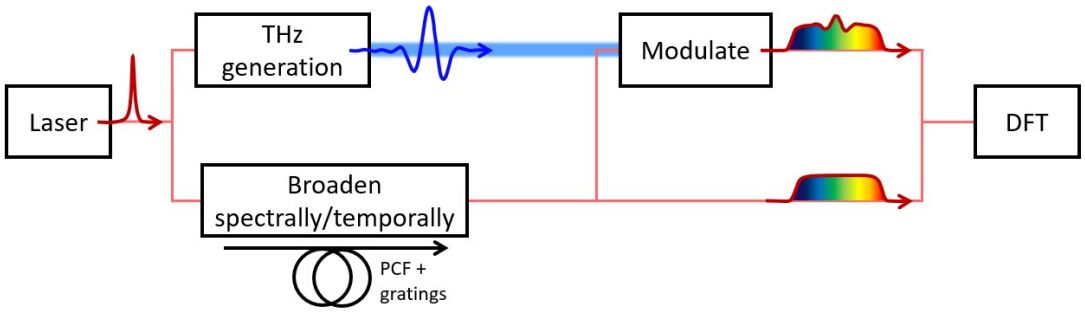

Figure 23: Overview of detection scheme

One of the strengths of the Ultrafast THz Spectroscopy lab is in the use of fiber optics for pulse-shaping to enhance field strength and bandwidth in THz generation and detection. This project is another example of the complementary nature of fiber and THz, specifically focusing on detection.

Certain questions about the technique are more easily answered using theory and simulations than experiment. Notably, the Pockels effect that is used to modulate the detection pulse for EOS can be viewed as a nonlinear frequency mixing process, not just as a polarization modulation, therefore we need to better understand how the proposed single-pulse detection scheme depends on bandwidth and pulse duration. In the case mentioned in [8], the detection pulse is only stretched in time, not spectrally broadened, and this leads to a trade-off between

the stretched pulse duration and the temporal resolution of the detected THz pulse. Here, the pulse undergoes nonlinear broadening mainly in the form of self-phase modulation to reach a much greater bandwidth than that produced by the laser. Therefore, the trade-off can be mitigated. Some parts of the detection technique are supported by theoretical simulations to verify observations.

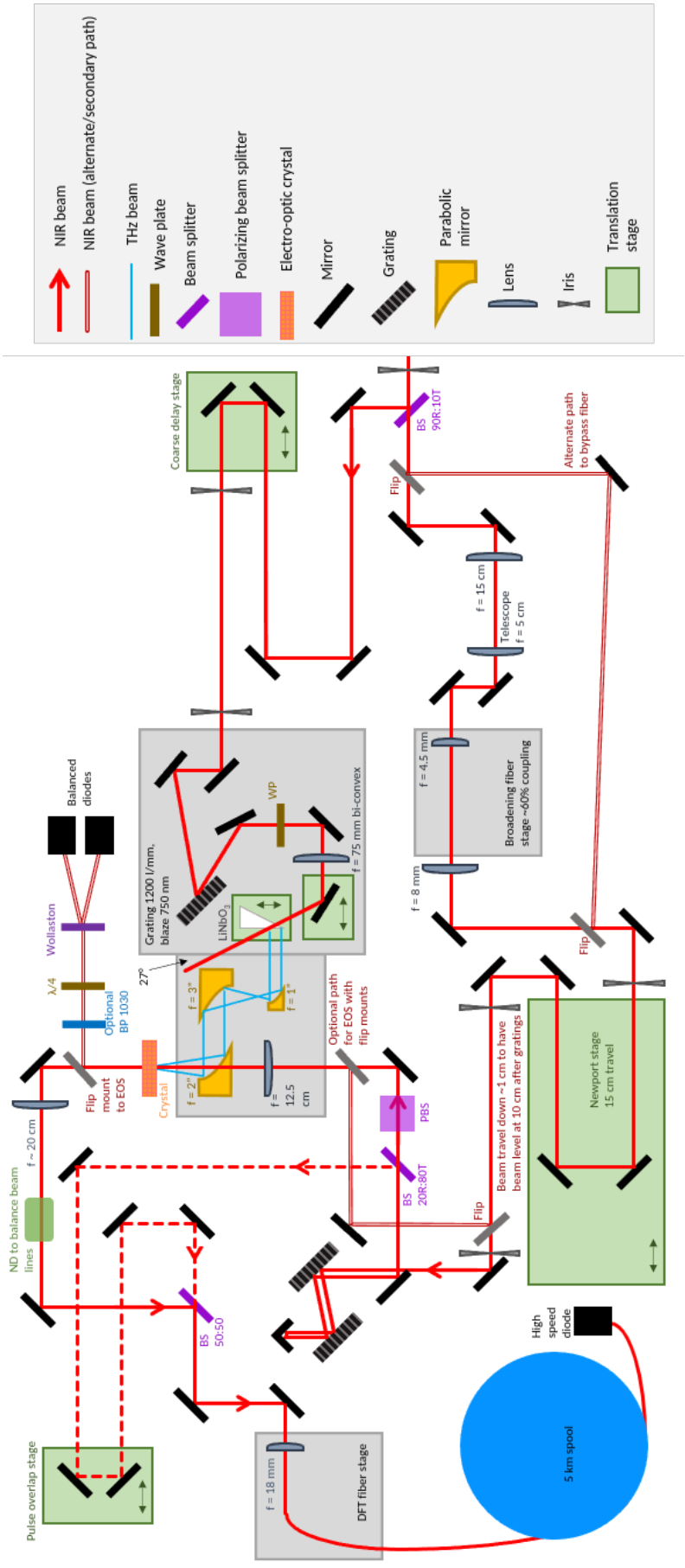

Figure 24: Schematic of full experimental layout with partial legend at right

Figure 24 provides an illustration of the full setup used for experimental work as it is placed on the optical table. The beam from the laser enters the setup at the right hand side of the illustration to encounter a 90% reflection beamsplitter which sends the majority of the laser intensity toward a tilted pulse front THz generation system. In this path, there is a coarse translation stage to compensate for large path length changes in the detection line during tests. The remaining 10% of the laser intensity is used as a probe to detect the generated THz pulse. This beam first passes through a telescope to shrink the beam width, then is coupled into an all-normal dispersion fiber to broaden its spectrum. An alternate path accessible using mirrors on flip mounts allows the user to bypass the fiber if need be. Next, there is a motorized micrometer precision translation stage to control the detection path length repeatably within $< 50\ fs$. The detection pulse then passes through a grating stretcher (roof mirror shift direction shown horizontal but vertical in practice) to increase the its duration. This can also be bypassed using flip mirrors. The beam passes through a polarizing beamsplitter to clean up the polarization state after spectral and temporal broadening, then focuses through the parabolic mirror to meet the THz beam in an electro-optic crystal. Before this occurs, part of the beam is split off to act as a reference for the THz modulated part. The probe beam can either be sent toward electro-optic sampling detection or passed through a 5 km optical fiber for high-speed detection.

4.1 Laser system

The development of femtosecond laser systems has facilitated the generation of THz pulses by providing pulses with peak powers high enough for optical rectification. The laser system used in experiment is in the PHAROS family from Light Conversion. The gain medium is a Yb:KGW crystal which has a tunable bandwidth in the 1030 nm range. It is pumped by a semiconductor diode.

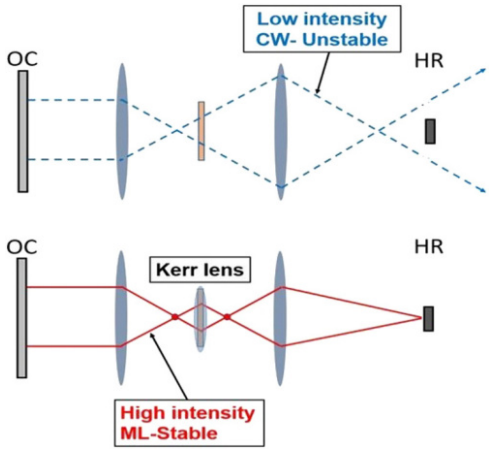

Figure 25: Ray tracing in a common type of Kerr-lens mode-locking cavity for (top) continuous wave radiation with random relative phase among modes vs. (bottom) intense pulse due to constructive interference achieved by mode locking [12]. HR: highly reflective mirror; OC: output coupler.

In order to create a short, intense pulse, the laser cavity must be configured to allow mode locking, that is to say that the phase of the longitudinal modes in the cavity become synchronized, creating periodic constructive interference peaks. In the PHAROS system, the gain medium also exhibits Kerr nonlinearity, leading to an intensity-dependent refractive index. Because of the typically-Gaussian transverse beam profile, this nonlinear effect causes the medium to act as a

lens. By spatially filtering the beam, the residual intensity between the constructive interference peaks is blocked. This filtering can be achieved in multiple ways, whether by including an aperture in the path or simply engineering the cavity such that light which does not experience the Kerr lens is diffracted outside the cavity as illustrated in Fig. 25. Under these conditions, the equilibrium state between gain from the medium and loss due to the spatial filtering is mode-locked operation [12]. This mechanism is the basis of the PHAROS oscillator. Part of the oscillator intensity is sent to a chirped pulse amplification stage to increase the pulse energy from $\sim$ 0.1 μJ to up to $\sim$ 10 to 1000 μJ depending on the selected repetition rate, which is tunable between 1 and 1100 kHz with a consistent average output power of 6 W.

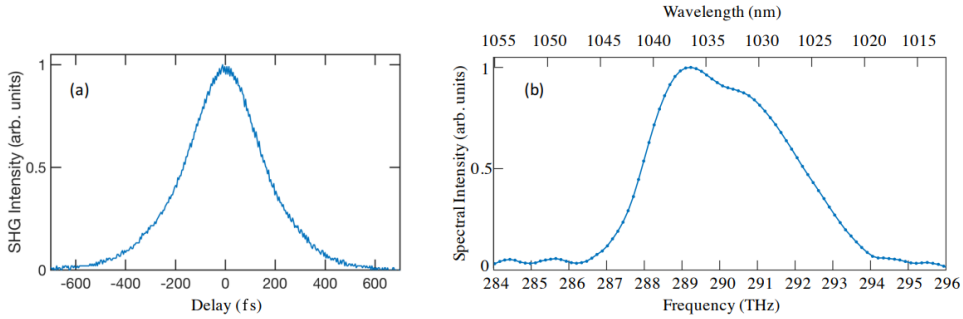

Figure 26: Laser autocorrelation (second harmonic signal generated at noncollinear overlap in a BBO crystal) and spectrum [13]. The deconvoluted pulse duration is approximately 180 fs full-width at half maximum (FWHM).

Figure 26 shows the autocorrelation trace of the laser pulse measured by noncollinear second harmonic generation as well as the laser spectrum. The temporal profile confirms a pulse duration of approximately 180 fs after deconvolution assuming a Gaussian shape. The spectrum is not Gaussian, which suggests that the laser compressor is not able to fully compensate for higher order dispersion within the pulse. Gratings are used to optimize the group velocity dispersion for a minimum pulse duration and can also be carefully adjusted to compensate for third order dispersion, but further pulse compression schemes can require additional prism or mirror systems to balance out residual fourth order dispersion and above [100]. However, this is not a serious concern for the work presented here.

4.2 Experimental terahertz generation

Figure 27 shows the compact single-lens layout used to generate THz radiation in $LiNbO_3$ via the tilted pulse front technique described in Section 2. The incoming pump beam is diffracted off a reflective grating, then imaged into the tip of the generation crystal through a large aperture bi-convex lens. A half wave plate rotates the polarization state after the grating to optimize for difference- rather than sum-frequency generation, though in practice some second harmonic radiation is still generated in the $LiNbO_3$ crystal. The THz radiation is emitted in a collimated manner, and subsequently focused using an imaging system composed of three parabolic mirrors. The last parabolic mirror has a hole drilled through it, tapering toward the reflective surface, to allow a NIR probe beam to overlap with the THz beam as it focuses into the detection crystal. The crystal used in this experiment is 5 mm thick GaP. The schematic shows two background rectangular outlines: these are individual breadboards. In particular, the parabolic mirror system is much simpler to align with a laser diode in the visible spectrum in order to avoid aberrations. The modular breadboards allow these sections of the optical path to be aligned

separately in a more convenient part of the lab, then later assembled. A THz camera was used initially to optimize THz spatial profile, intensity and direction when emerging from the $LiNbO_3$ crystal. Afterward, the imaging breadboard can be placed where the camera was such that the 1" focal length parabolic mirror captures the THz radiation. We move the THz camera to the position of the electro-optic crystal to optimize the THz focus and ensure it overlaps with the NIR probe focus.

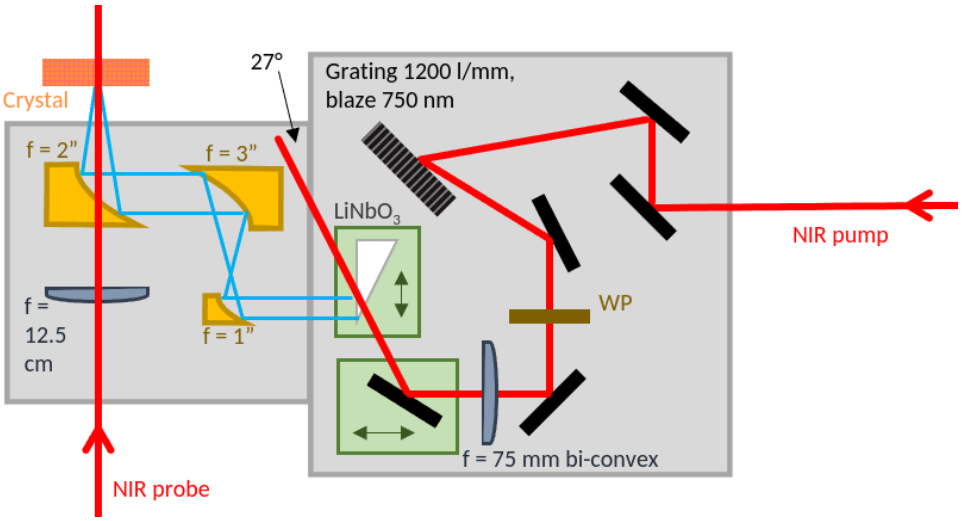

Figure 27: Schematic of experimental layout for THz generation using $LiNbO_3$

In order to have a baseline measurement for what the generated THz waveform looks like in the time domain, an electro-optic sampling arm accessible by flip mount is set up after the detection crystal (see top center Fig. 24). It is comprised of a quarter wave plate, Wollaston prism and two biased silicon diodes connected to a lock-in amplifier set to measure the difference between the two balanced signals as outlined in Section 2. Consistent with previous studies for similar pumping conditions, the peak THz frequency is slightly below 1 THz with a bandwidth of approximately 1 THz [7].

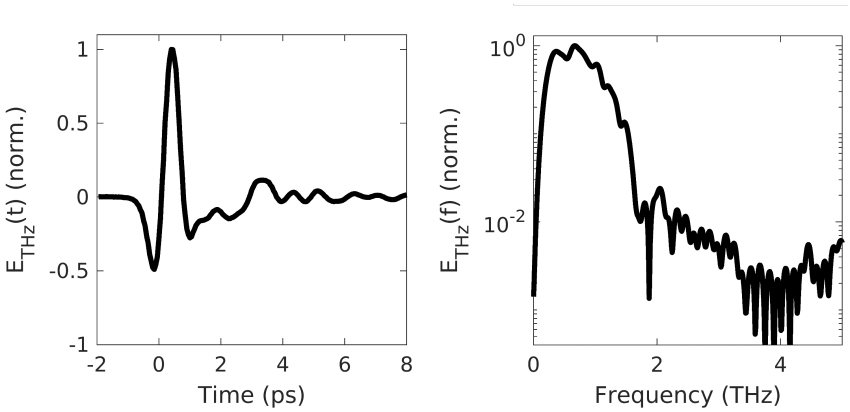

Figure 28: EOS measurement of THz pulse with unmodified laser pulse. The maximum occurs at 0.7 THz and the bandwidth at half maximum is 0.9 THz (spanning 0.2 to 1.1 THz)

The best dynamic range that one can hope to achieve in EOS measurements is on the order of about 10^3 without averaging [101, 23]. This single measurement is therefore not particularly well optimized, but shows the expected temporal and spectral profile of the THz pulse. The

measurement consists of 200 points, each one requiring half a second for data acquisition. The lock-in time constant is set to 100 ms, and there is a programmed software wait time of 400 ms to allow the stage to move and stabilize for a total measurement duration of 100 s. It is possible to reduce the acquisition time with continuous scanning schemes and faster lock-in settings, but this is the baseline for our laboratory implementation. A dry air or nitrogen environment around the THz path in the setup could help to improve signal amplitude and obtain a smoother spectrum by reducing absorption in water vapor [102].

4.3 Photonic crystal fiber for spectral broadening

The broadening fiber used for this project is a photonic crystal fiber designed and fabricated at the Max Planck Institute for the Science of Light by Nicolas Y. Joly. It is an all-normal-dispersion (ANDi) fiber. Self-phase modulation broadens the laser spectrum while leaving the low-noise phase profile [56, 103]. In contrast, broadening in the anomalous regime is prone to modulation instability [78]. Figure 29 shows a close-up view of the fiber cross section including capillary holes and core.

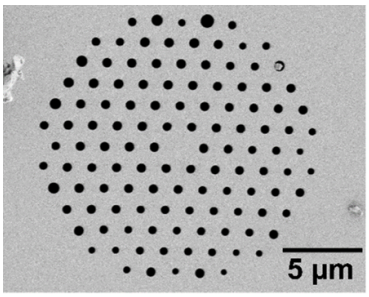

Figure 29: SEM image of fiber core

4.3.1 Coupling efficiency

This fiber has a very small core size, meaning that to achieve optimal coupling, careful consideration of focal length, numerical aperture and focus spot size are required. The focus spot size depends on the initial diameter of the beam and on the focal length of the lens used, but lenses with short focal lengths that are practical for this application typically have small usable diameters, leading to clipping if the beam is not first demagnified using a telescope. This leads to a tradeoff as both a large initial diameter and short focal length are desirable. Since the numerical aperture of the fiber has not been measured, it was ultimately easier to compare experimental coupling efficiencies to select a good configuration.

In Table 1, there is a comparison of achieved coupling efficiencies as a function of focal length and magnification for a 1 m fiber. These measurements were taken using average input powers of 2 mW and below at a repetition rate of 1.1 MHz with pulse duration increased to further lower the peak pulse intensity. Using the full-size laser beam, coupling is poor as much of the laser intensity is clipped around the lens. As the telescope system decreases the size of the beam incident on the lens, results improve for decreasing focal lengths. The lens with the shortest focal length used, 3.1 mm, has a very high numerical aperture of 0.7, which appears to be too large for the fiber acceptance angle since coupling efficiency starts to cap out in the lower left corner of the table. Ultimately, the best coupling was obtained for a 4.5 mm focal length at 0.33 magnification.

		Focal length [mm]				
Pulse duration	Magnification	3.1	4.5	8	11	18.4
180 fs	1		6%	13%	12%	8%
6 ps	1		6%	13%	12%	9%
6 ps	0.67		12%	16%	17%	
6 ps	0.5		11%	18%	16%	
6 ps	0.33	20%	23%	16%	12%	6%
6 ps	0.25	21%	21%	15%	11%	

Table 1: Comparison of various coupling configurations for a 1 m length of fiber. Values in table represent percentage coupling efficiency $= 100 \times \frac{\text{(optical power before coupling lens)}}{\text{(optical power at fiber output before collimation)}}$. Empty cells were not tested. Highlighted cells show promising range. Parameters were tested roughly from right to left and top to bottom order, with some repetitions to ensure consistency. Focal length 4.5 mm at 0.33 magnification is the selected optimal configuration.

These coupling measurements were performed at a pulse duration of 6 ps to decrease the peak power below the threshold for nonlinear effects to ensure that the power in vs. power out were more accurate. When the spectral bandwidth increases, the powermeter measurements become unreliable.

When starting coupling with a 1 m length of fiber, a small bend will help prevent higher-order or cladding mode content from reaching the output facet, leaving only the fundamental to maximize. It is then possible to delicately cleave the extra fiber away, leaving only a 5 cm length and a coupling efficiency increased by approximately a factor of three to reach 60%.

However, when starting from scratch with the 5 cm segment used in experiment, the initial spike in coupled optical power is often due to light travelling through the cladding. Therefore, to redirect into the fundamental mode, it becomes necessary to image the fiber tip. The lens normally used to collimate the output light is moved slightly farther from the fiber to bring the fiber tip image into focus on a camera sensor about 10 cm away. Figure 30 shows the process of imaging the fiber tip, starting in a) with poor coupling dominated by cladding modes and then reaching a position in b) with the light creating a bright disk in the core. From this point, the fiber xy position relative to the focus is typically close enough that optimizing coupling can be done based on maximizing output optical power. The rings and dot patterns are likely artifacts due to camera saturation.

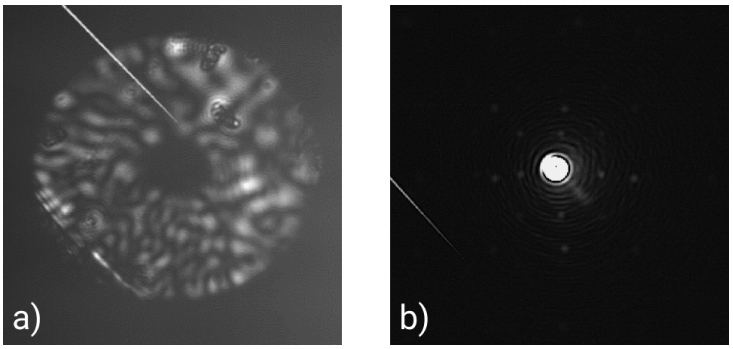

Figure 30: a) Image of fiber tip at the start of the coupling process for a short fiber where the ring shape clearly shows the cladding is lit up and the core is not. b) Fiber tip image after adjusting the fiber position on its 3D stage to couple light into the core.

Another important consideration is that this solid core fiber cannot withstand arbitrarily high peak intensities. Based on the core diameter of approximately 3 μm as shown in Fig. 29, we can estimate that an approximate "spot size" for the beam in the fiber of $A_{eff} = \pi(1\ \mu\text{m})^2$. The pulse energy is approximately:

$$p = \frac{\overline{P}}{F} \tag{4.1}$$

where $\overline{P}$ is the average laser power and F is the laser repetition rate. From this, the peak power and intensity are as follow:

$$P_{peak} = \frac{p}{T_0} \tag{4.2}$$

$$I_{peak} = \frac{P_{peak}}{A_{eff}} = \frac{p}{T_0 A_{eff}} \tag{4.3}$$

where T_0 represents the pulse duration. For fused silica, the measured breakdown intensity is 55 GW/cm^2 [104], for a maximum pulse energy at $T_0 = 180$ fs of:

$$p(T_0 = 180\text{ fs}) = \left(55 \times 10^9\ \text{W}/(10^{-2}\ \text{m})^2\right)(180 \times 10^{-15}\ \text{s})\pi(10^{-6}\ \text{m})^2 \tag{4.4}$$

$$= 0.3\ \text{nJ} \tag{4.5}$$

Another estimate is that the dielectric strength of fused silica is ~ 500 MV/m [105]. Assuming a refractive index near 1.5, this gives an intensity of:

$$I = \frac{cn\epsilon_0}{2}|E|^2 \tag{4.6}$$

$$= \frac{(3 \times 10^8)(1.5)(8.85 \times 10^{-12})}{2}|500 \times 10^6|^2 \tag{4.7}$$

$$= 50\ \text{GW/cm}^2 \tag{4.8}$$

which is consistent with the previous limit. These estimates would mean that the maximum average power incident on the fiber should be:

$$\overline{P}(180\text{ fs}, 1.1\text{ MHz}) = pF = (0.3 \times 10^{-9})(1.1 \times 10^6) = 0.3\ \text{mW} \tag{4.9}$$

In practice, experiments with a different photonic crystal fiber with a core diameter double that of the fiber considered here (see [11]) gave good results up to ~ 40 nJ for the same input conditions. Because the breakdown pulse energy scales with the square of the core diameter, a reasonable value becomes $p_{max} \approx 10$ nJ. The limit for average power is then:

$$\overline{P}(180\text{ fs}, 1.1\text{ MHz}) \approx 10\ \text{mW} \tag{4.10}$$

Measurements were performed using this as a maximum power with no apparent problems. The more conservative theoretical estimate above serves mainly as an order-of-magnitude calculation to illustrate the throughput limitations of the system since it does not take into account the mode profile of the beam. The actual mode cross-section is larger than the effective area obtained with a radius of 1 μm.

4.3.2 Comparison with simulation

Based on simulation code developed in Section 3, we worked on a model to match the experimental spectral broadening (see Table 2 for parameters). In this case, the scalar GNLSE model is sufficient as the polarization properties are of little interest; the polarization state is cleaned

up with a beam-splitting polarizer afterward. The orientation of the principal fiber axes was not evaluated. The all-normal dispersion curve of the PCF is determined via an empirical model taking into account the microstructures and can be modelled with a polynomial expansion. This yields coefficients $\beta_2 = 0.015$ ps^2/m, $\beta_3 = -3.7 \times 10^{-5}$ ps^3/m, $\beta_4 = 3.0 \times 10^{-7}$ ps^4/m, $\beta_5 = -1.1 \times 10^{-9}$ ps^5/m, $\beta_6 = 2.5 \times 10^{-12}$ ps^6/m. In Fig. 31, the experimental spectrum is overlaid with a simulation result with matching parameters. The experimental spectra exhibit a spectrum far more skewed toward shorter wavelengths, however the overall structure and bandwidth are comparable. The discrepancies may be due to a more complex initial experimental pulse that the simulation fails to account for. The starting point for the simulation is a Gaussian envelope with a small amount of second and third order dispersion applied to better match the experimental data (see simulation parameters, Table 2).

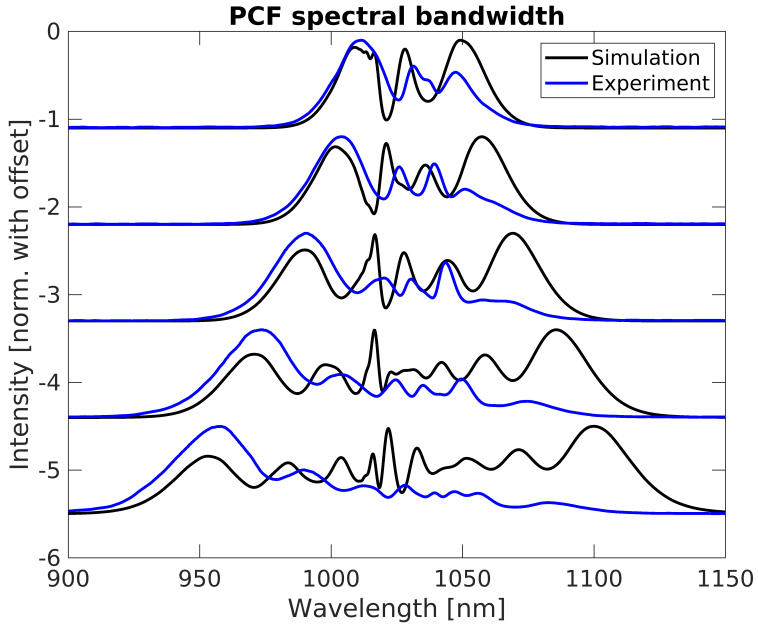

Figure 31: Comparison of experimental and simulated spectra from the PCF. From top to bottom, the average input pulse power levels are 2.5, 3.3, 4.6, 6.7 and 8.8 mW respectively. Measurements performed at 1.1 MHz repetition rate with a coupling efficiency of approximately 60% for a pulse duration of 180 fs.

The resolution and effective scan length for single-pulse THz detection will be determined by the pulse bandwidth and duration. The first of these characteristics is controlled by the PCF as shown above: a higher peak input power gives a broader spectrum. After that, the amount of chirp applied is determined by the grating stretcher which controls the final duration of the pulse for THz detection.

4.4 Grating dispersion

The output pulse from the broadening PCF then travels through a double-pass grating stretcher system to temporally stretch the pulse so that it overlaps with the full THz oscillation. The beam hits both gratings for its first "pass", then is reflected back with a roof mirror to hit both a second time (second "pass") before continuing.

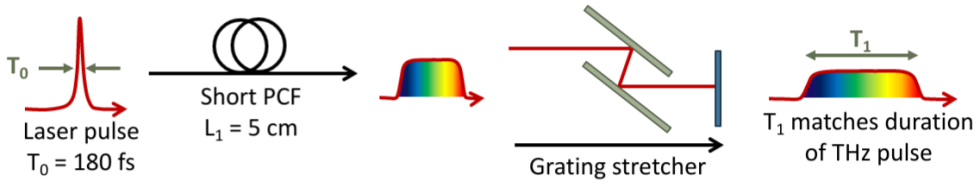

Figure 32: The detection pulse undergoes spectral broadening in the PCF but does not stretch significantly in time. It propagates through a double pass grating pair to apply enough chirp that it can fully overlap with the THz pulse.

A pair of gratings will chirp the pulse negatively, such that short wavelengths precede long wavelengths in time [100]. It is worth noting that this is the inverse of what usually happens in a material such as silica. For this project, this means that when the pulse travels through the detection crystal, the shorter wavelengths are ahead in time but after DFT in the long fiber, the long wavelengths will be ahead in time.

4.4.1 Simulation

Grating dispersion coefficients can be expanded to high orders by taking derivatives of the phase imparted by the grating pair [100, 106]:

$$\phi_g = \frac{2\omega L_g}{c}\left[1-\left(\frac{2\pi c}{\omega d}-\sin\gamma\right)^2\right]^{\frac{1}{2}} \tag{4.11}$$

where ω is the light frequency, L_g is the distance between the two parallel gratings measured along the normal to their surfaces, c is the speed of light, d is the grating period and γ is the angle of incidence measured from the grating normal [100].

This results in second order or group velocity dispersion (GVD), third order dispersion (TOD) and fourth order dispersion (FOD) terms as follow:

$$\text{GVD} = \frac{d^2\phi_g(\omega)}{d\omega^2} = -\frac{\lambda^3 L_g}{\pi c^2 d^2}\left[1-\left(\frac{\lambda}{d}-\sin\gamma\right)^2\right]^{-\frac{3}{2}} \tag{4.12}$$

$$\text{TOD} = \frac{d^3\phi_g(\omega)}{d\omega^3} = \frac{3L_g\lambda^4(d+d\cos 2\gamma+2\lambda\sin\gamma)}{4c^3\pi^2 d^3}\left[1-\left(\frac{\lambda}{d}-\sin\gamma\right)^2\right]^{-\frac{5}{2}} \tag{4.13}$$

$$\text{FOD} = \frac{d^4\phi_g(\omega)}{d\omega^4} = -\frac{3\lambda^5 L_g(d^2\cos 4\gamma+3d^2+4(d^2-\lambda^2)\cos 2\gamma+16d\lambda\sin\gamma\cos^2\gamma+6\lambda^2)}{8\pi^3 c^4 d^4\left[1-\left(\frac{\lambda}{d}-\sin\gamma\right)^2\right]^{\frac{7}{2}}} \tag{4.14}$$

Under the conditions $\lambda = 1030$ nm, $1/d = 300$ lines/mm, $\gamma = 45°$ and $L_g = 4$ cm, the values are GVD$= -1.80\times10^4$ fs^2, TOD$=2.53\times10^4$ fs^3, FOD$=-4.9\times10^4$ fs^4.

To apply dispersion to a pulse, it is convenient to work in the frequency domain where the dispersion from the gratings can be applied as a phase shift. By analogy with the dispersive part of the GNLSE seen in the previous section, we can see that the linear dispersion summation

can be represented as a phase factor modifying the Fourier-space spectral amplitude:

$$\frac{\partial \tilde{A}}{\partial z} = i \sum_{k \geq 2} \frac{\beta_k \omega^k}{k!} \tilde{A} \tag{4.15}$$

$$\int \frac{\partial \tilde{A}}{\tilde{A}} = \int i \sum_{k \geq 2} \frac{\beta_k \omega^k}{k!} \partial z \tag{4.16}$$

$$\ln \tilde{A} = i \sum_{k \geq 2} \frac{\beta_k z \omega^k}{k!} + \text{const. from initial conditions} \tag{4.17}$$

$$\implies \tilde{A}(z, \omega) = \tilde{A}(0, \omega) \exp\left(i \sum_{k \geq 2} \frac{\beta_k z \omega^k}{k!} \right) \tag{4.18}$$

This is written in terms of absolute frequency, but one can easily switch to relative frequency instead. For gratings, the z dependence is not necessary, what is needed is an expression to find the electric field amplitude knowing the input and the grating stretcher properties. In fact, the spatial dependence $\beta_k z$ can be replaced with $\frac{d^k \phi_g(\omega)}{d\omega^k}$ to give field $\tilde{A}_g$ after passing through the gratings.

$$\tilde{A}_g(\omega) = \tilde{A}_0(\omega) \exp\left(i \sum_{k \geq 2} \frac{d^k \phi_g(\omega)}{d\omega^k} \frac{\omega^k}{k!} \right) \tag{4.19}$$

Taking the simulation results from Fig. 31 for reference, the effect of a grating pair with an incidence angle of 45° and a separation of 4 cm measured along the grating normals is shown in Fig. 33. The center wavelength for grating dispersion estimates is taken to be the laser center wavelength of 1030 nm.

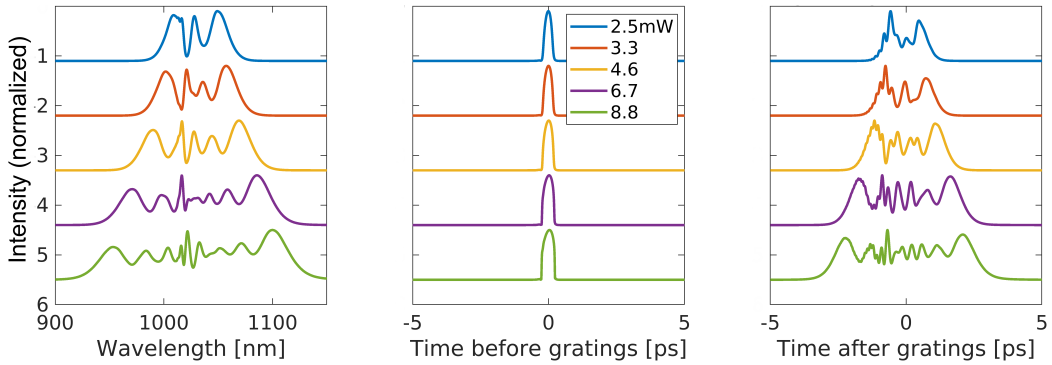

Figure 33: The effect of grating pair on the simulated detection pulse after PCF spectral broadening. Spectra at left correspond the the simulation results in Fig. 31. In the center, the corresponding intensity profile in the time domain after the PCF. Right, the temporal profile after the grating pair using the values calculated above (GVD= -1.80×10^4 fs^2, TOD=2.53×10^4 fs^3, FOD=-4.9×10^4 fs^4). The broader the spectrum, the greater the final pulse duration.

Using these calculations for the grating dispersion and the effect of the PCF, it is useful to create a spectrogram to ensure that the frequency content of the pulse is well spread across the longer duration. This reveals the instantaneous frequency content of the pulse across its duration by convolving it with a gating pulse. The spectrogram function used is:

$$\sigma(\omega, \tau) = \left| \int A_g(t) A_{ref}(t - \tau) e^{i\omega t} dt \right|^2 \tag{4.20}$$

where A_g denotes the electric field envelope for the detection pulse after the gratings and A_{ref} is that of a reference pulse used for gating.

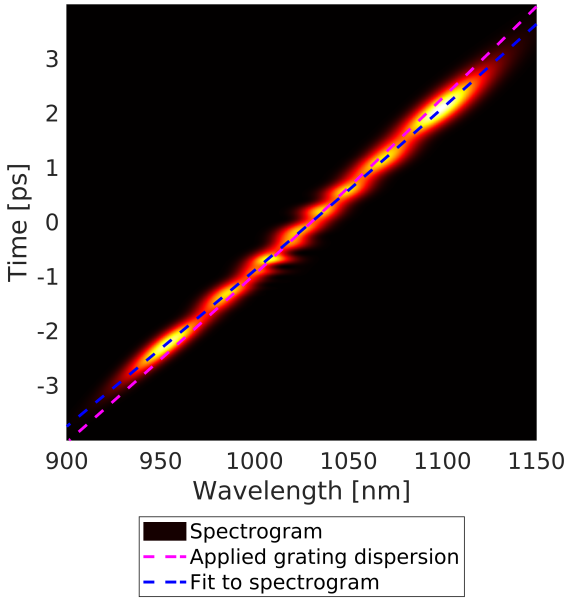

Figure 34: Simulated spectrogram for the highest average input power in Fig. 33, 8.8 mW. After passing through the PCF, the pulse is elongated by the grating stretcher and the chirp is close to linear with respect to the wavelength.

The result of this spectrogram simulation is shown in Fig. 34 for the broadest spectrum of Fig. 33. A_{ref} was taken to be a Gaussian pulse with a FWHM duration of 100 fs. Since the PCF has its own dispersion and nonlinear processes which modify the temporal profile of the pulse, it can be seen that the applied grating dispersion does not perfectly match the actual chirp. The applied grating dispersion curve follows the form:

$$\Delta T = (\text{GVD})\Delta\omega + \frac{1}{2}(\text{TOD})(\Delta\omega)^2 + \frac{1}{6}(\text{FOD})(\Delta\omega)^3 \tag{4.21}$$

where GVD, TOD and FOD were calculated above (see Eq. 4.12) and $\Delta\omega = \omega - \omega_0$ where ω_0 is the center frequency of the pulse (corresponding to 1030 nm wavelength). An adjusted fit, also shown, gives a better instantaneous wavelength-to-time conversion within the pulse (GVD$= -1.66 \times 10^4$ fs^2, TOD$=2.3 \times 10^4$ fs^3, FOD$=-4.9 \times 10^4$ fs^4).

With this fixed grating configuration, the resulting temporal duration can effectively be tuned purely based on the spectral bandwidth, which in turn scales with the input power at the PCF. Based on a model where the NIR detection beam is assumed to have a Gaussian form, the temporal resolution associated to the frequency encoding becomes $\delta t = \sqrt{T_0 T_C}$ where T_0 is the unchirped pulse duration in the Fourier-transform limit case and T_C is the pulse duration after applying grating chirp [49]. Effectively, this condition gives a time resolution limit which relates the spectral bandwidth available for encoding and the temporal duration available for encoding, i.e. $\delta t \propto \sqrt{T_C/\Delta\omega}$. Though not Gaussian, the available spectral bandwidth for encoding in the case illustrated in Fig. 34 spans approximately 150 nm, corresponding to a Gaussian $T_0 \sim 10$ fs, while $T_C \sim 5$ ps. This would result in a temporal resolution on the order of $\sqrt{10 \times 5000} = 224$ fs,

which is similar to the temporal resolution normally obtained in electro-optic sampling with our 180 fs laser pulse.

4.4.2 Experimental considerations

As noted previously, the short length of fiber that is used for spectral broadening does not significantly increase the duration of the laser pulse as SPM occurs. Therefore, a grating pair is necessary to chirp the pulse to increase its duration. With a different type of fiber, it might be feasible to incorporate both the spectral and temporal broadening steps into one longer fiber propagation step resulting in a similarly chirped pulse. The advantages would be fewer alignment concerns, potential for a more compact setup without the double pass grating pair, and possibly better overall throughput. The 300 groove/mm gratings used in this experiment reportedly have an absolute efficiency of about 70% for a single incidence which means $0.7^4 = 0.24$ or 24% efficiency optimistically for the four sequential diffractions, neglecting that some energy is lost to other diffraction orders. In practice, the measured efficiency for the power ratio after to before gratings is about 12% or $0.12^{\frac{1}{4}} = 0.59$ or 59% of intensity directed into the first diffraction order per incidence. The disadvantage of working with fiber only would be the loss of the chirp degree of freedom.

One key challenge when aligning the gratings is to avoid all spatial chirp or aberration since this makes it impossible to couple the entire bandwidth of the modulated pulse into the second optical fiber used for DFT. For practicality, we used an incidence angle of 45° which orients the zero-order diffraction beam perpendicular to the incident beam in order to use the optical table grid as an alignment aid.

4.5 Electro-optic modulation

4.5.1 With electro-optic sampling

As mentioned previously, there is an electro-optic sampling option which helps to find the correct motorized translation stage position for temporal overlap between the THz and probe pulses using existing Labview automation. This is also interesting in that it helps show the difficulty in correctly interpreting sampled THz signals if the probe pulse does not have a negligible duration compared to the THz pulse. In this section, we consider some results from signals measured under different probe conditions.

In Fig. 35a, we see the same signal as was shown in Fig. 28, measured using conventional electro-optic sampling with a short probe pulse from the laser. In b, the probe beam passes through the grating stretcher before interacting with the THz pulse. The measured THz waveform does not change significantly, nor does its frequency content. The gratings do modify the temporal profile of the NIR pulse: they can stretch the pulse to a maximum duration of approximately 500 fs over the 15 nm laser spectral bandwidth. This should degrade the temporal resolution and distort the signal. However, this effect is not evident, possibly because the underlying dispersion on the pulse is of the opposite sign, allowing the grating to partially compensate. In rows c to e, the beam passes through the broadening PCF and grating stretcher and the distortions due to increased bandwidth and duration are more evident. The frequency bandwidth of the waveforms stays the same, but the shape of the spectrum varies with input power.

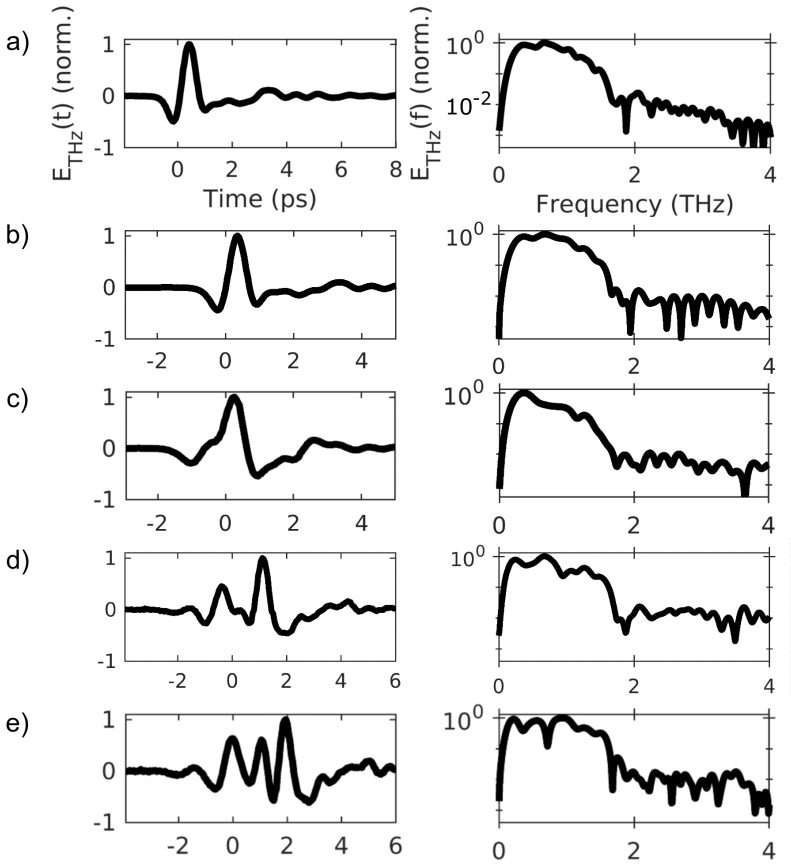

Figure 35: Electro-optic sampling signals recorded at 1.1 MHz repetition rate with a) laser pulse as probe (bypassing PCF and gratings), b) probe bypassing PCF but passing through grating stretcher, c) probe passing through PCF (average input power 2.5 mW) and gratings, d) probe passing through PCF (average input power 6.7 mW) and gratings, e) probe passing through PCF (average input power 8.8 mW) and gratings. Lefthand column shows normalized time domain signal (temporal zero delay arbitrary) and the righthand column contains the normalized log-scale frequency content of the waveform. Note that the pulse energy for THz generation does not vary throughout these measurements.

It is also important to note that the shape of the signal varies based on the overlap between THz and probe pulses in the detection crystal. While rows c, d, and e are measured with probes following identical optical paths, rows a and b are two variants designed to bypass one or more pulse shaping stages in the detection line and therefore may have slight discrepancies in spatial overlap since they were optimized independently at the overlap with the THz beam. The beams for the line passing through the PCF and the line going around are both aligned to the same reference irises and position when monitoring consistency across motorized translation stage path length, but they have different widths and may not focus at precisely the same position.

We saw in Section 2 that for electro-optic sampling, the signal measured is roughly proportional to the product of the probe intensity and THz field amplitude (see Equation 2.36). Therefore, taking the waveform in Fig. 35a as a reference, we can use the simulated probe pulses after PCF and gratings corresponding to the input powers shown in c, d and e to verify that the distortions behave as expected. This signal is estimated as:

$$S(t) = \int d\tau E_{THz}(\tau) I_{probe}(\tau - t) \tag{4.22}$$

where the integral represents the long integration time for the diodes and lock-in amplifier. The temporal overlap product between probe and THz pulses is integrated, hence the need for a short probe pulse to precisely sample as short an interval as possible. Equation 4.22 shows that in the limit where the probe can be represented by a Dirac delta function, the THz waveform will be faithfully reproduced while a longer pulse will become convoluted with the original signal. If the lengthened probe still has a single peak, the effective result is similar to boxcar averaging, and the higher frequency features will be lost. However, the pulse used in experiment has a complex multi-peak structure shaped by self-phase modulation. This leads to the creation of new peaks in the measured transient.

This is illustrated in Fig. 36, which takes the three waveforms from Fig. 35 measured with both PCF and grating stretcher in the detection line and pairs them with simulations of the expected probe pulse temporal profile after PCF and gratings (see Fig. 33). The reference THz pulse for the simulations is the one measured via regular electro-optic sampling using the laser pulse. Qualitatively, simulation imitates experiments in the development of additional peaks and the signal elongation in time. The discrepancies are likely explained in part by the potential spatial overlap inconsistency discussed above between the reference (no PCF, no gratings) and these experimental results as well as the pronounced spectral asymmetry in experiment which is not well reproduced in simulation.

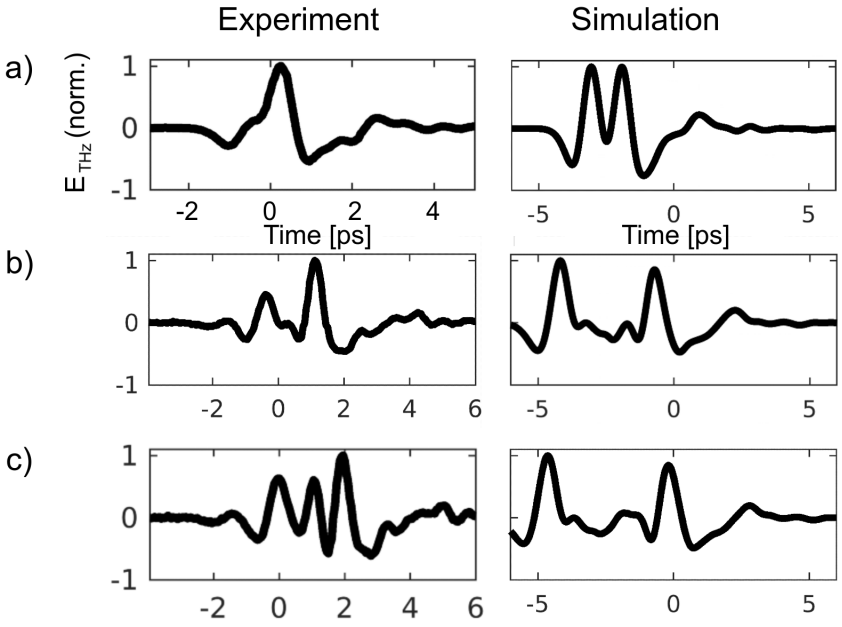

Figure 36: Comparison of experimental electro-optic sampling results with simulation. a) Probe passing through PCF (average input power 2.5 mW) and gratings, b) probe passing through PCF (average input power 6.7 mW) and gratings, c) probe passing through PCF (average input power 8.8 mW) and gratings.

The modulation depth $\frac{\Delta S}{S_1+S_2}$ as described in Section 2 at the peak electric field position was approximately 0.1% for a 1.1 MHz repetition rate or 1% for a 50 kHz repetition rate. This is not wholly representative of the peak field since, as seen above, the peak for an electro-optic measurement with a broadband chirped pulse may be convoluted with the probe. The two measurements are comparable in that they were made with the nearly the same probe pulse energy and bandwidth. The tenfold increase is expected; the peak pump intensity increases by an order of magnitude as the repetition rate changes from 1.1 MHz to 50 kHz. As shown in the

solution to Eq. 2.6, the THz field amplitude depends on $|A_{pump}|^2$, the intensity.

4.5.2 With USB spectrometer

The experiments of the previous section allow us to determine the correct position for the electronic translation stage in order to temporally overlap THz and NIR probe pulses by finding the distorted THz signal encoded on the shaped probe pulse under different experimental conditions. It provides a baseline for comparisons with alternate detection techniques and demonstrates the need for a sufficiently short time resolution in order to measure the THz pulse accurately. With this knowledge, we can move toward utilizing the spectrum as an extra degree of freedom on which to encode the THz electric field waveform as illustrated in Fig. 37. The Pockels effect occurs on a faster time scale than the THz pulse oscillations, causing an instantaneous polarization modulation on the region of the spectrum temporally overlapped with a particular point in the THz signal.

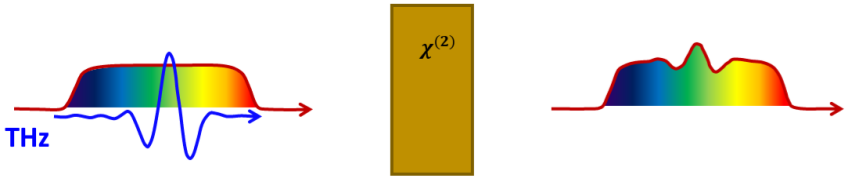

Figure 37: The spectrally and temporally broadened detection pulse interacts with a THz pulse when the two are overlapped in space and time in a $\chi^{(2)}$ crystal such as GaP. This schematic is does not show that the effect is actually a polarization rotation.

For these measurements, we use a calibrated USB spectrometer (StellarNet) with 0.5 nm resolution to give an absolute frequency reference for the dispersion on the probe pulse. These experiments were performed at a 50 kHz repetition rate to strike a balance between THz modulation depth and probe intensity: the higher the peak laser intensity, the greater the THz field, but the more the average power must be decreased in the probe line to avoid damaging the delicate PCF.

For a first test, we block the modulated probe using a single polarizer to measure the square of the THz signal. In Fig. 38, we see the probe spectrum, then the modulation detected through the polarizer from interacting with the THz pulse. To extract $|E_{THz}|^2$, this modulation must be normalized by the probe intensity. For electro-optic sampling with a short pulse, this normalization can be omitted because each sampled delay uses the same probe intensity. In this case, the intensity is variable across the measured time period, and this will scale the modulated signal accordingly. The $\Delta I/I_0$ spectrum shown in c should be proportional to $|E_{THz}|^2$. In d, the wavelength is transformed to a time delay according to Eq. 4.21 using the fit from Fig. 34. For comparison, the reference EOS signal with no PCF and no grating stretcher is squared and shown in orange. The peak positions roughly line up with the reference.

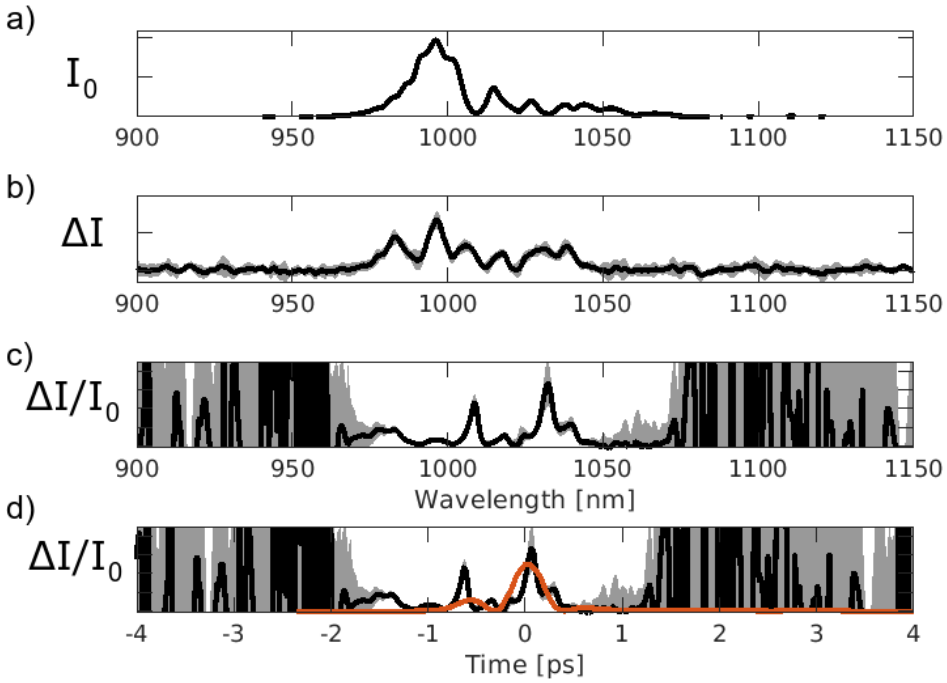

Figure 38: a) Probe pulse spectral intensity I_0 generated with 370 μW average power input to PCF, b) Difference between spectra through polarizer with and without THz modulation ΔI, c) Difference normalized by probe spectrum $\Delta I/I_0$, d) Normalized difference mapped to time domain according to fitted grating response with reference squared THz waveform overlay in orange. Grey outline represents standard deviation over 5 measurements. All vertical scales arbitrary.

This probe bandwidth appears to give a 3 ps sampling window, which is sufficient for tests but would not be adequate for resolving resonances without fitting [24].

The single polarizer, as mentioned in Section 2, is limited by its lack of phase sensitivity. Knowing that $\Gamma \ll 1$, it also creates a smaller signal to detect than a phase sensitive scheme would ($\Gamma^2 < \Gamma$). We next turn to the scheme described in Section 2.2.2 which adds a quarter wave plate and rotates the polarizer to let part of the background reach the USB spectrometer. Figure 39 shows results measured at 50 kHz using this technique. Panel a) shows the spectrum of the probe broadened by the PCF. Row b) shows the spectrum measured after the detection crystal, quarter wave plate and polarizer with THz pulse modulation visible in the more intense regions of the spectrum. The three different columns here are showing the same measurement for different probe translation stage positions, each one shifted by a delay of 1 ps $= \frac{2(150\ \mu\text{m})}{3\times10^8\ \text{m/s}}$. To extract a quantity proportional to the electric field, the same measurement through the polarizer is also done while blocking the THz generation line to give a reference. Then the THz signal is recovered using equation 2.48. According to its convention, a) shows $|E_0|^2$, b) shows S_{THz} the THz modulated signal, c) shows $\sqrt{S_{THz}} - \sqrt{S_{ref}}$ and d) shows $\frac{1}{E_0}(\sqrt{S_{THz}} - \sqrt{S_{ref}})$. Noise level is estimated by standard deviation across five repeated measurements, then taking the maximum variation at each point when comparing point-wise standard deviation and analytical error propagation. The paler filled outline shows this variability.

The three relative probe delays across Fig. 39 allow us to verify the time mapping based on grating and fiber dispersion. In row d), features A, B and C are identified as they appear on different regions of the spectrum. In e), we show that the shift they experience between probe delays is in good agreement with the simulated dispersion curve across the measurement window.

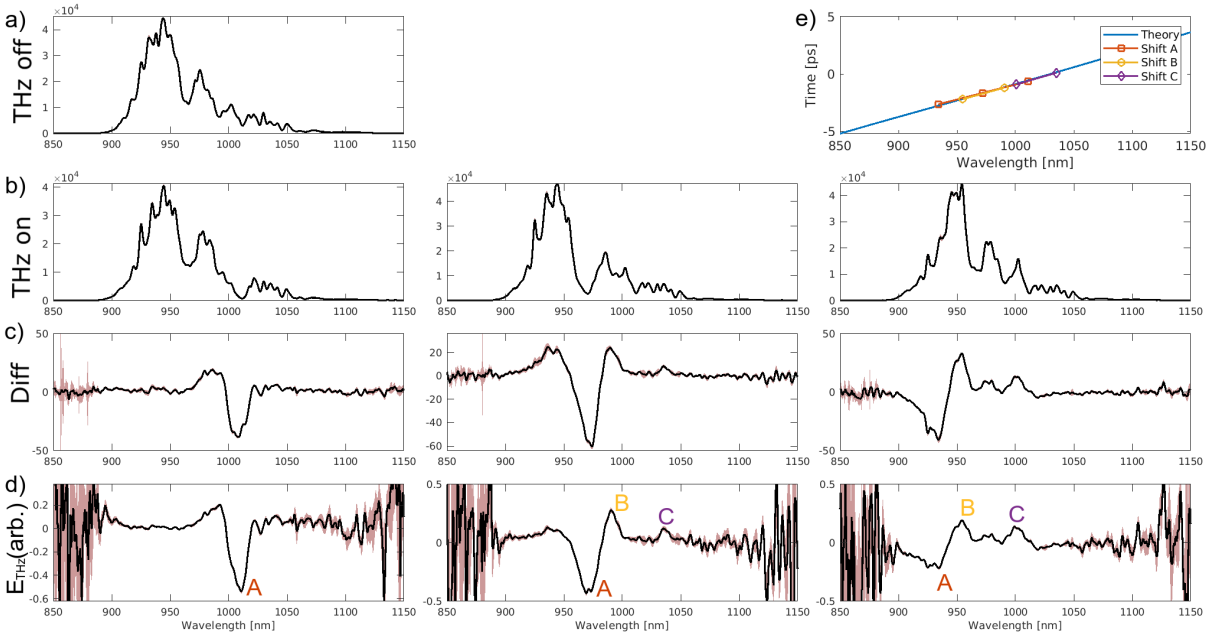

Figure 39: a) Spectrum of probe pulse without THz, repetition rate 50 kHz, average input power 450 μW at PCF. b) Row of spectra measured showing THz modulated probe after quarter wave plate and polarizer oriented 15° from vertical for three different relative probe delays separated by 1 ps. c) Difference between square root of spectra in b and the square root of their equivalent with THz beam blocked. d) Signal in c normalized by square root of a; this is proportional to THz electric field. Note certain features labelled which are visible at different wavelengths as the probe delay varies. e) Comparison of simulated grating dispersion feature shift as a function of relative probe delay. Standard deviation outline shown in a, b, c, d over a sequence of five measurements.

The left most panels for rows b, c, d are taken with the shortest probe path length, so the THz pulse only interacts with the later end toward the longest wavelengths. Conversely, the right most panels the probe path has been lengthened by 2 ps so that the main THz peaks are on the earlier section with the "ringing" tail spread across the rest of the probe spectrum. Again, the measurement window is only about 3 ps in duration. These measurements were realized with a 20 s integration time on the USB spectrometer, meaning they require about the same amount of time as an electro-optic sampling scan.

Up to now, we have been using quadratic and cubic terms in the grating dispersion. In actuality, the response can be approximated by a linear dependence, which has two distinct advantages over the higher order model. First, it is easily invertible within the range of interest so that a temporal shift can be related to a frequency shift by just an effective GVD coefficient and vice versa. The second advantage is similar, and it is that the conversion no longer requires an absolute frequency reference. The fourth order dispersion model based on simulated grating and PCF dispersion is a Taylor series expansion about the 1030 nm pump. Without knowing where a point is situated relative to the pump, the temporal mapping risks inaccuracy due to the curvature of the higher order polynomial. A linear approximation sets a uniform projection over the experimental bandwidth.

In Fig. 40, we continue the previous analysis of features shifting with relative probe delay to fit a linear mapping between frequency and time. Part a shows a sequence of five probe delay steps varying by 0.5 ps each time with different features of the THz waveform identified in color

to help visualize how they shift as a function of probe delay. Note that in a, the lines are not a fit. Five features are selected and their position for each probe delay is shown in b with a linear fit for the temporal dependence. Applying dispersion is conventionally done in the frequency domain, so we have transformed from wavelength to relative frequency $\Delta\omega$ with respect to the pump at 1030 nm. In a situation where only group velocity dispersion is present, the temporal stretching will be linear with respect to frequency.

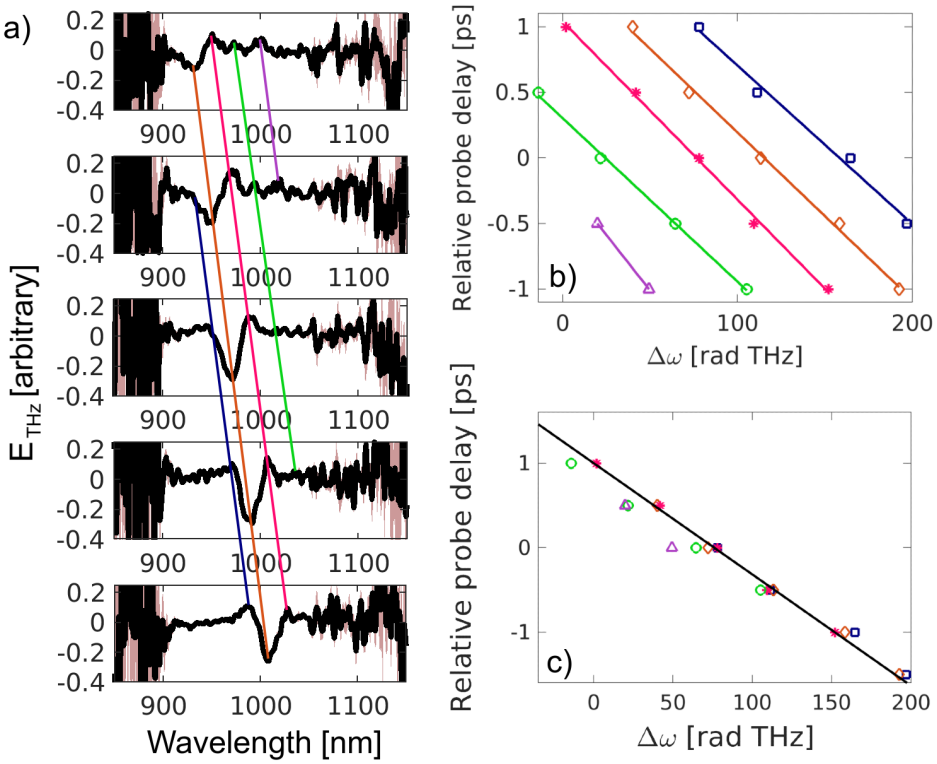

Figure 40: a) Normalized signal proportional to THz field at five relative probe delays; shift between consecutive plots is 0.5 ps. THz feature encoding location shifts as probe delay varies, lines are a guide to the eye. b) Linear fitting of feature shift from one probe delay to the next. c) Feature positions brought relatively closer together to view agreement with weighted average slope fit.

The effective GVD based on a linear fit was estimated as a weighted average of the slopes shown in b, with weighting according to the number of points used to calculate each slope. The resulting GVD= -1.318×10^4 fs^2 is most accurate on the orange diamond and pink star points, which are the most reliable as they are extracted from features clearly visible at all five probe delays. The calculated GVD was -1.80×10^4 fs^2 with an opposite sign TOD, so the effective GVD nearer to zero relative to the simulated value makes sense. In Fig. 41, we show the difference between the two models in the region of interest for spectral encoding. Between 900 and 1150 nm, the two are in quite good agreement. The maximum distance between the two is 0.3 ps in this range, but the relative distance is at most 0.13 ps (i.e. if the mappings were offset to minimize error between them in this range). This value is reaching the laser pulse duration resolution limit for electro-optic sampling, so it should be adequate for initial measurements. Ultimately, the goal will be to reduce noise and repeat this calibration for the best accuracy.

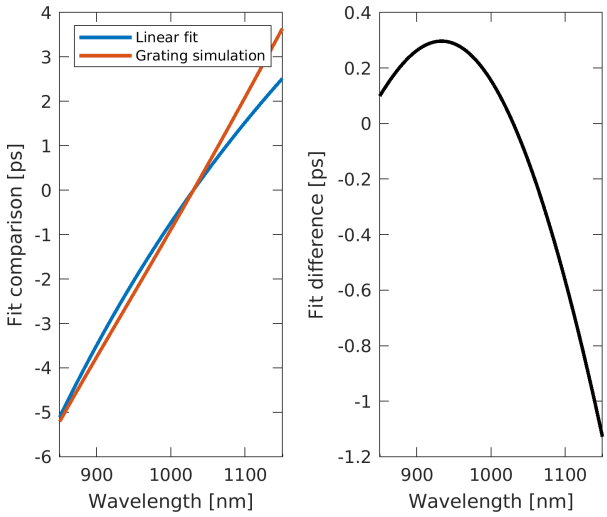

Figure 41: Comparison of cubic simulation dispersion model and linear fit to experimental data; difference in predicted time delay (linear minus cubic).

Another parameter to explore is the polarizer angle for detection of the THz modulation–a smaller angle keeps $\sin\theta \approx \theta$ true to obtain better linearity with respect to the THz field while a larger angle gives more intensity on the detector to improve signal quality. We vary from 6° to 24° in Fig. 42. The modulation depth calculated as one minus the ratio of "THz on" over "THz off" at the peak THz field position at 970 nm decreases from 80% at 6° and 10° down to 50% at 24°. On this scale, it isn't obvious which extracted signal looks best. The varying spectral amplitudes result from the different intensities reaching the detector. In principle, it is possible to solve for θ knowing the sin dependence, though this breaks down in the limit where there is over-rotation beyond the region $\theta \in [-\frac{\pi}{2}, \frac{\pi}{2}]$ in which this mapping is one-to-one [53]. However, this is challenging to calibrate given the units and rescaling necessary to perform the arcsin operation. Assuming linearity in these measurements and EOS is generally standard.

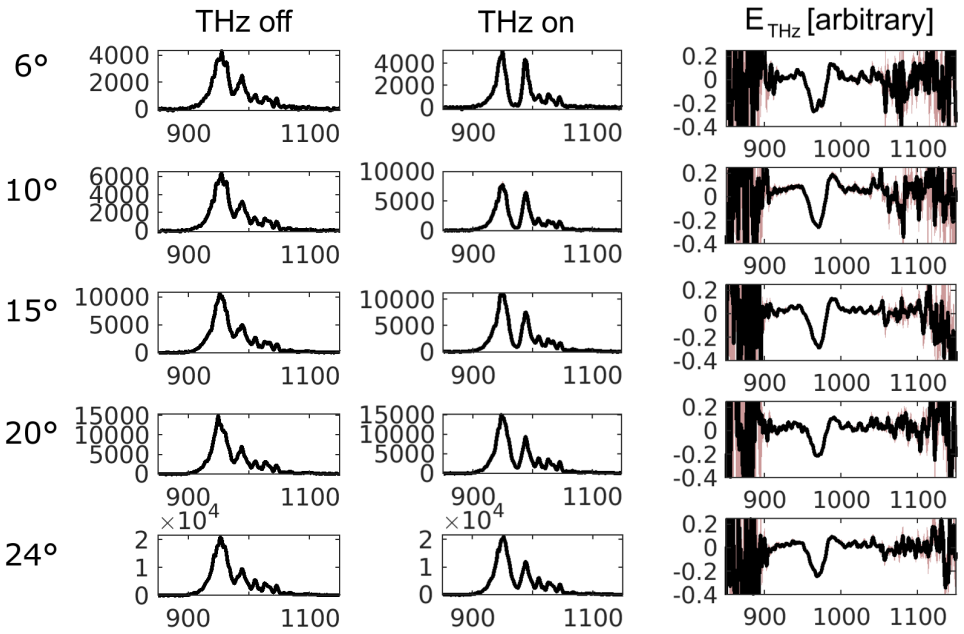

Figure 42: Spectra without and with THz modulation and inferred THz waveform for five detection polarizer angles as indicated at left. Since the purpose of these measurements is to compare the signal accuracy and noise in the y axis, the x axis is left as a function of encoding wavelength.

To see the noise level better, Fig. 43 is an expanded view of the normalized traces from 42 further normalized by maximum amplitude. Those at 6°, 10° and 25° are the smoothest, but the higher angles distort the relative heights of the two opposite signed peaks at 970 and 990 nm, in particular masking the 990 nm dip. The 10° to 15° orientations look to be the best for this particular detector system.

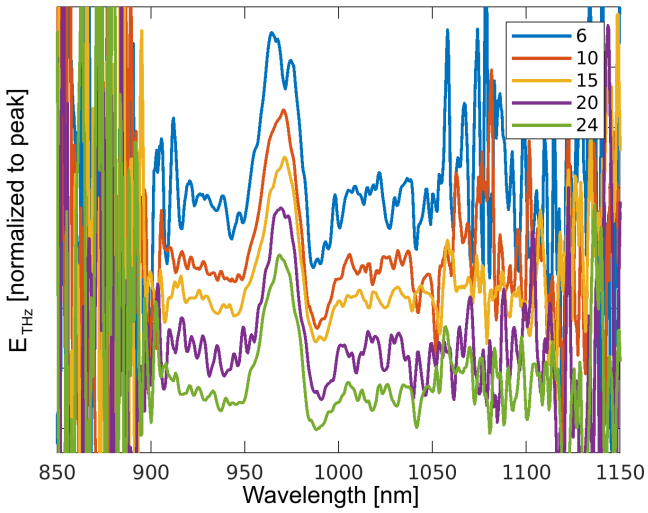

Figure 43: Closer view of normalized THz modulation for different polarizer angles.

4.6 Dispersive Fourier transform

The final component required in shifting toward single-pulse detection is a highly dispersive medium with which to perform a dispersive Fourier transform. The idea of a "physical" implementation of a Fourier transform appears in many areas, for example viewing a diffraction pattern in the far field gives the spatial transform of the obstacle, or similarly a lens results in a Fourier transform at the focus in the "Fourier plane" [107]. For this project, we exploit the dispersive properties of a long optical fiber to cause the frequency content of a pulse to spread in time, resulting in an increase in pulse duration from a few picoseconds to tens of nanoseconds. If the fiber's group velocity dispersion profile is relatively flat across the pulse spectrum, then the stretch will occur linearly with respect to the optical frequency. The lengthened pulse is long enough that a high-speed photodiode with a better-than-nanosecond response time can resolve the temporal profile of the pulse. Figure 44 shows the plan: use the interference pattern between reference and probe pulses passed through the long optical fiber to infer the modulation due to the THz pulse. A similar technique has been used previously to monitor pulse-to-pulse variation in a fiber ring cavity at a high repetition rate [56].

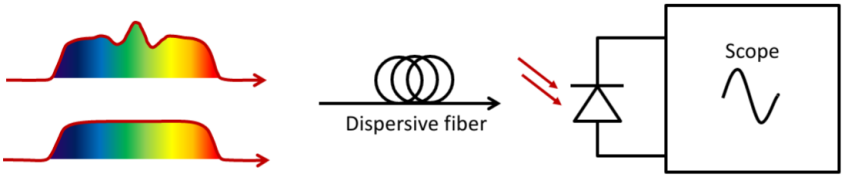

Figure 44: A THz-modulated copy of the detection pulse is coupled with an unmodulated copy into a 5 km commercial optical fiber. The dispersion causes the resulting interference pattern to be stretched out and mapped into the time domain so it can be measured with a high-speed photodiode and oscilloscope.

4.6.1 Demonstration of concept

One of the first initial explorations for this project was to find a long segment of fiber and verify that it could be used as a spectrometer by sufficiently dispersing a laser pulse in time. By varying the input peak power to a 5 km commercial fiber [Corning HI 908, $D(980\text{ nm}) = -63$ ps/(nm km) and $D(1030\text{ nm}) = -55$ ps/(nm km)] at a level sufficient to cause nonlinear spectral broadening, it is possible to generate spectra of various bandwidths to test the dispersive Fourier transform (DFT) process. In particular, this works because the dispersion length $L_D \sim 30$ m is far greater than the nonlinear length $L_{NL} \sim 10$ cm (both defined in Section 3), such that the spectral broadening process occurring in the first few centimeters of propagation can largely be considered independent to the dispersive Fourier transform process. In Fig. 45, the results are shown, comparing the output spectrum measured with a grating-based USB spectrometer with the signal from a high-speed diode [Thorlabs FDS025 silicon photodiode] and oscilloscope [Zurich Instruments UHFLI, sampling rate 1.8 GHz]. Average input power levels ranged from 1 to 15 mW at a pulse duration of 1 ps. Qualitative shape agreement is quite good.

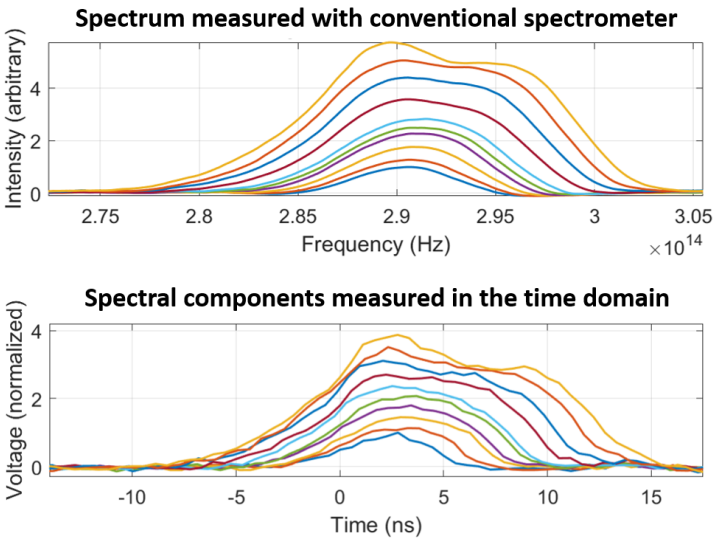

Figure 45: Comparison of spectrum measured with conventional spectrometer and signal measured in the temporal domain after a 5 km fiber.

To make sure that these results are consistent with the expected fiber specifications, the following equation gives an estimate of the final temporal stretch based bandwidth and dispersion:

$$\Delta T = \beta_2 L \Delta\omega = \beta_2 L (2\pi \Delta\nu) \tag{4.23}$$

As shown in Fig. 46, the frequency FWHM bandwidth expected based on the β_2 calculation is consistent with the measured spectral bandwidth of the pulses, indicating that the DFT process is complete. If the fiber were not long enough, the output would not be in the temporal "far field" i.e. the spectral components would not fall at distinct points in time.

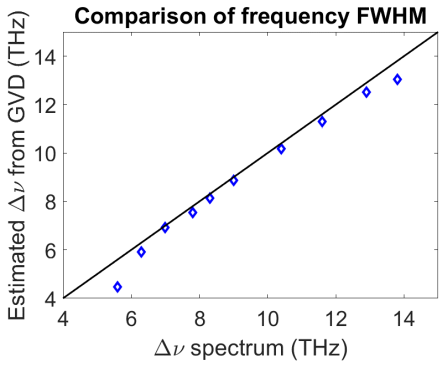

Figure 46: Frequency bandwidth verification for DFT. The horizontal axis represents the spectral FWHM from the USB spectrometer data, while the vertical axis represents the bandwidth $\Delta\nu = \frac{\Delta T}{2\pi\beta_2 L}$ associated with the temporal FWHM ΔT in the oscilloscope measurements.

One challenge is immediately obvious from the single-pulse spectra in Fig. 45: stability to ensure a workable noise level for monitoring pulse-to-pulse changes. In these experiments, average optical powers on the order of mW were available at the input of this 5 km fiber at 1.1 MHz repetition rate; when integrated into the single-pulse THz detection system, the broadening PCF limits the average optical power to mW, but then gratings and further optics downstream leave only tens of μW for the DFT process through a fiber with a coupling efficiency of 5% or less. This poses a challenge for getting clear readings on the oscilloscope.

4.6.2 Integration into single-pulse scheme

We use a feature on the UHFLI known as the periodic waveform analyzer (PWA) which averages over many pulses to solve the challenge of signal to noise for a proof of concept experiment. By using the laser repetition rate as a trigger, the PWA creates a 360° cycle for the repetition period. Further reducing the phase window to a small interval surrounding the pulse allows the effective sampling rate to be increased past the 1.8 GHz rate of the scope and facilitates averaging over many pulses by synchronizing to the laser trigger. Figure 47 shows the comparison between an averaged PWA pulse ("PWA center") and the "Scope" single pulse acquisition. They have the same duration and similar envelope shapes, but the PWA trace has far fewer fluctuations due to the averaging. This figure illustrates another challenge: spatial chirp in the probe beam. The spectral content of the probe pulse is not uniformly distributed, likely due to the grating stretcher. When the probe beam is incident on a grating, the different spectral components are each diffracted at a different angle. Any misalignment between grating pair or in the angle of the roof mirror for the second pass can lead to an angular variation over the probe spectrum upon exiting the stretcher system. This angular deviation becomes a shift in the focal position after passing through a lens. In Fig. 47, the nanometer fiber coupling stage is shifted in the horizontal direction, remaining in the focal plane but travelling parallel to the optical table, to shift the fiber coupling condition to those seen in "PWA λ long" and "PWA λ short". The difference in stage position between these two curves is on the order of 10 μm. The position used for the following experiments is "PWA center", which captures the greatest spectral bandwidth. The coupling lens chromatic dispersion is another limiting factor in our ability to pass the full spectrum through the 5 km fiber; we use an achromatic lens, but in practice a slight wavelength dependence in focal position along the optical axis still exists.

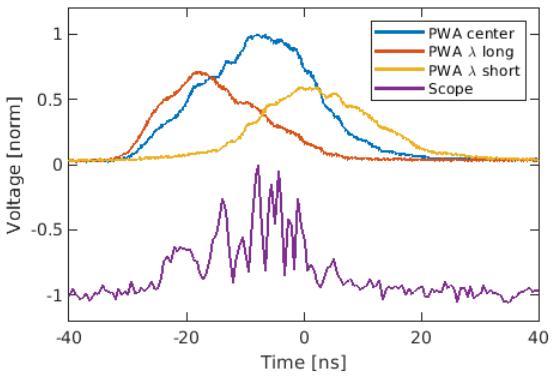

Figure 47: Comparison of PWA and scope sampling and demonstration of spatial chirp at in-coupling for DFT.

We repeat the THz modulation experiments shown in Fig. 39 with a quarter wave plate and polarizer at 15°, but the detector is a high-speed diode [Newport 1544-B] placed after the DFT fiber. We measure the probe with and without interacting with THz in order to obtain the THz waveform, or at least a section of it, on the PWA trace. The results of this process are shown in Fig. 48. The acquisition time for each trace is 0.6 s. Despite these being the three same probe pulse stage positions as in the USB spectrometer data, the normalized signal is not recognizable. The delay in the leftmost column shows a sharper dip that may correspond to the peak field position, but it shifts out of the measurement range at the other positions. This

warrants more thorough investigation to determine if the signal is too distorted to recognize, or if the THz-probe temporal overlap was off. There is a 35 ns window for data extraction. In terms of spectral bandwidth, this corresponds to:

$$\Delta\omega = \frac{\Delta T}{\beta_2 L} = 218 \text{ (rad·THz)} \tag{4.24}$$

where $\beta_2 = -\frac{\lambda^2}{2\pi c} D = 0.0321$ ps^2/m evaluated at 980 nm. For comparison, the spectrum generated in the PCF spans from 910 to 1020 nm at 10% of the maximum (see Fig. 39a), corresponding to a bandwidth of 224 (rad·THz). With only the β_2 term for conversion, the relative time to frequency mapping is consistent with expectations and indicates that nearly the whole spectrum can be used to encode information despite the spectral asymmetry. With an absolute frequency calibration for the UHFLI PWA and scope, it would be possible to include a further correction by estimating β_3 according to the variation of β_2. The inclusion of higher order dispersion terms would lead to a more exact time axis for the THz waveform to ensure that its frequency content is more accurately represented. It is also possible to use the motorized translation stage to map out the time axis as a function of relative delay between THz and probe pulses instead of relying on the dispersion specifications of the optical components as shown in previous sections.

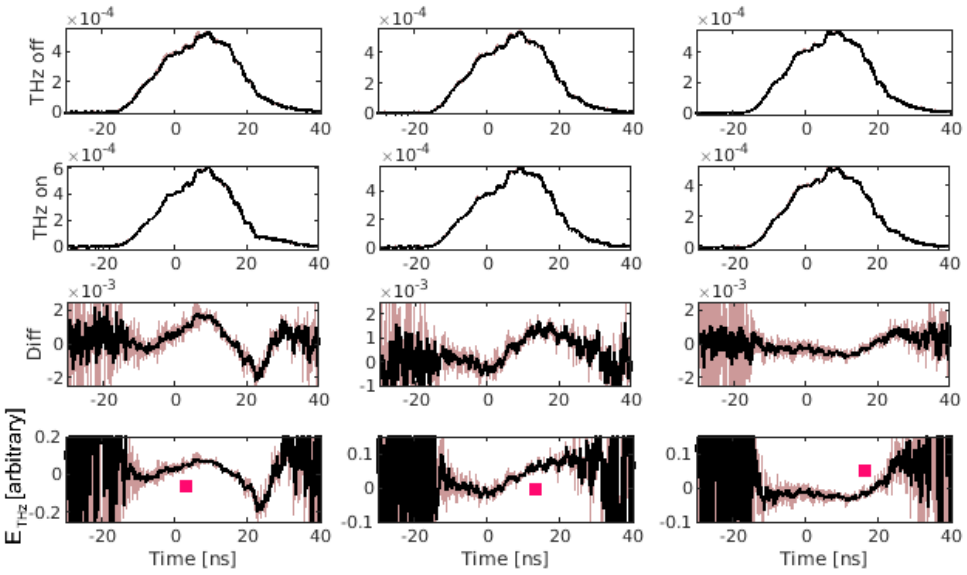

Figure 48: Extracting THz modulation from measurements with DFT on periodic waveform analyzer for three relative probe delays. THz off: temporal pulse profile with THz generation blocked S_{ref}. THz on: pulse profile with THz pulse modulation S_{THz}. Diff: square root difference $\sqrt{S_{THz}} - \sqrt{S_{ref}}$. Norm: normalized signal $\frac{1}{E_0}(\sqrt{S_{THz}} - \sqrt{S_{ref}})$. Noise shown as standard deviation over five measurements.

The earlier negative times after 5 km dispersive fiber ($\beta_2 > 0$) are the longer wavelengths. Indicated with a square is a rise which shifts from modulating longer to shorter wavelengths in the spectrum as the probe delay stage is shifted, lengthening the probe path length by the equivalent of 1 ps each time from the left column to the right column. At this point, these are a guide to the eye only to indicate the direction of the shift and are not placed quantitatively. The midpoint of this rise shifts by approximately 10 ns over for each 1 ps change in probe path length, or an expected frequency shift of 62 (rad·THz). According to the effective GVD for a linear fit, this frequency shift should be equivalent to a 0.8 ps difference in probe delay. Because

clearer peaks are not visible from one delay to the next, this has not yet been more accurately calibrated.

To date, we have not implemented the interferometric scheme, first because it is possible to use other strategies to extract the THz pulse amplitude and phase encoded on the probe and secondly because finding the temporal overlap for interferometric measurements is difficult with weak, temporally stretched beams. Typically, the temporal overlap could be deduced through enhanced second harmonic generation in a crystal such as BBO. The power level and temporal profile of the probe do not make this a viable solution currently. However, we have succeeded in coupling both modulated and unmodulated beams into the DFT fiber when working at a laser pulse duration of 6 ps. This internal compressor setting allows for a ten fold increase in average power incident on the the broadening PCF and thus a ten fold increase in probe power later in the beam path, facilitating alignment.

The probe line which interacts with the THz beam is coupled first using the 3D stage and two mirrors immediately before it to optimize for the angle and position of incidence on the coupling lens. This is adjusted to reach a coupling efficiency of 5% through the 5 km fiber. The loss for this fiber is specified to be < 2.5 dB/km; taking this value as an expected absorption gives a loss of 12.5 dB or a coupling efficiency of 5.6%. With a thorough study of focal lengths and telescope options as performed for the PCF, we may be able to reach a higher coupling efficiency for the probe beam. The reference beam which bypasses the THz detection crystal is coupled into the DFT fiber with the pair of mirrors preceding the beamsplitter that recombines reference and probe beams. This comparatively coarse alignment strategy reaches a coupling efficiency of 1% in the measurements shown below in Fig. 49. The pulse duration on the PWA is shorter than in Fig. 48 as the spectral bandwidth is smaller. The peak power incident on the PCF is lower for these tests (10 kW here vs. 50 kHz). So far, no interferometric pattern is observed.

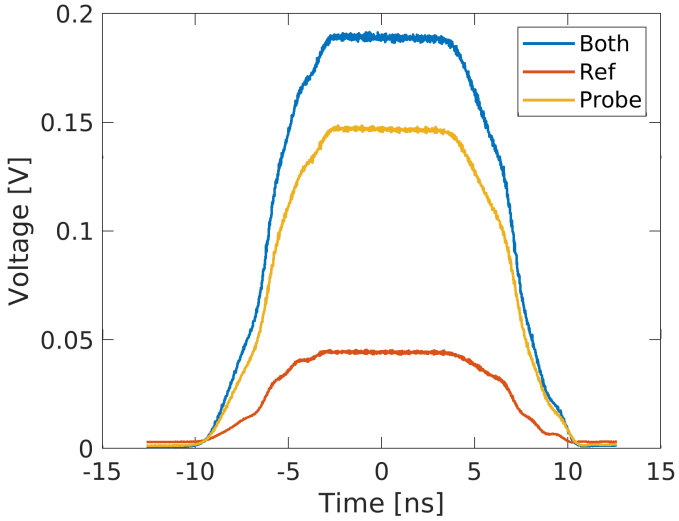

Figure 49: DFT fiber coupling test with reference and probe beams on PWA.

5 Conclusion

In this thesis, we have designed and shown the initial implementation of a single-pulse THz detection scheme based on spectral encoding of the THz waveform onto a broadened, chirped probe. We experimentally demonstrated recovery of a partial THz waveform via the dispersive Fourier transform. Simulations were carried out to characterize elements of the detection scheme, ensuring that the results are consistent with our understanding of the physics at play. Particular attention was paid to improving existing numerical models to solve CGNLSEs in optical fiber, incorporating different depolarization models and mapping to the frequency domain to accelerate computations.

In future, we intend to continue to improve the existing experimental configuration. As with any new experimental project, difficulties arise in the execution and, in hindsight, there may have been simpler strategies that could have been used. Here are some notes on past and present challenges as well as solution ideas.

5.1 Challenges and solutions

This detection scheme has many practical challenges. For one thing, the PCF places a hard limit on the average power in the detection arm. In the current configuration, the gratings and many other optics have a significant amount of loss.

Potential improvements could be to remove the gratings and use a greater length of PCF - as seen in Fig. 14 the pulse duration increases to ~ 10 ps after 1 m travel. Alternatively, recoupling into another low-loss, high-dispersion fiber or high-index material with antireflection coatings could be a way to achieve temporal stretching. The advantage of this substitution is two-fold. First, the overall loss in the detection path could potentially be lowered to increase signal in the final experiment. Arguably, more efficient gratings could also reach this result, but the second benefit of this change would be in preserving a more uniform spectral distribution across the spatial profile of the beam by avoiding the sensitive grating alignment. Another note on the PCF is that it requires significant attenuation of the beam to avoid optical damage. It could be worth testing spectral broadening in commercial fiber with comparable dispersion near the wavelength range of interest as the large core would be easier to couple into and less prone to damage.

The THz generation process should be optimized for spectroscopic experiments; one quick fix is to enclose the THz path in a nitrogen or dry air purged environment to reduce loss from absorption in water. This can help to ensure a smoother reference spectrum as well. The presence of dips in the spectrum in Fig. 28 is an indicator that effort could be put into further improving THz generation efficiency, imaging and overlap with the probe pulse at the detection crystal.

The initial layout on the optical table had the motorized translation stage and broadening fiber swapped so that the stage needed to be aligned so optimally that fiber coupling was consistent across its travel length. This proved highly impractical; motorized stages such as the 15 cm Newport model we use naturally have a certain amount of curvature or bending in response to load (two mirrors in this case) or clamping conditions which gives a lower limit to the beam angle and position precision which can be expected. In practice, fiber coupling was fairly consistent (i.e. no more than 30% drop in coupling efficiency) when the stage was on one side of the center position but dropped much more rapidly (50% drop after 1 cm travel) on the other side of center.

The coupling efficiency had to be re-optimized regularly if the stage was being moved around, which was inconvenient and also detrimental to signal-to-noise due to general instability. To improve this issue, we switched the layout so that the optical component most sensitive to small angle deviations, the broadening fiber, was before the stage. The actual single-pulse detection process does not require the stage to move during measurements, but it is a necessary part of calibration using electro-optic sampling. For future work, a similar thought process might suggest that the translation stage may be better if placed in the THz generation line so that the 5 km dispersive fiber does not suffer from the same instability. Granted, this fiber has a much larger core and is therefore slightly less stringent in coupling conditions, but it could be a potential adjustment for overall stability in the detection path. In general, the overlap between THz and probe pulses can withstand a small amount of variation over the translation length during electro-optic sampling because the THz spot size is much larger than the NIR spot. As long as the probe remains well within the THz spot, the modulation can still occur.

More generally, having seen that this scheme has conceptual promise, it would be worth investing in better achromatic and antireflection-coated optics to reduce loss and ensure uniformity across the broadened detection spectrum. Similarly, calibrating for spectral response instead of assuming achromatic behavior should lead to more accurate translations between time and frequency.

Unlike a conventional grating-based spectrometer, the dispersive Fourier transform spectrometer does not have an absolute frequency reference. Applying the correct time-to-frequency conversion works with this relative system if we consider only the linear chirp from group velocity dispersion β_2, but after this the spectral components must be mapped back to a THz time delay using absolute frequency. If a correct calibration is found for a specific set of input parameters based on a known spectrum, this may suffice for most measurements, but does not generalize to other conditions. A potential solution could be to use a trigger with the second lock-in amplifier input and a short pulse. This could have the second advantage of triggering data collection only within a margin around the pulse, to avoid wasting computer memory and resources on the points in between since the signal has an extremely low duty cycle at the repetition rates below 1 MHz.

As of now, the single-pulse scheme does not have good signal to noise properties compared to electro-optic sampling and lock-in detection. However, for single-shot approaches the criterion for effectiveness is that the SNR must be better than electro-optic sampling for the same averaging time [8]. Therefore, if a single conventional scan takes 2 minutes, averaging over the equivalent number of individual pulses has to give equally precise results. Currently, the USB spectrometer integration time is 30 s each for THz-modulated spectra, with additional one-time measurements of the probe spectrum without polarizer, reference spectrum with polarizer and lab background at the start of measurements for data analysis and normalization. On the periodic waveform analyzer, data acquisition takes 1 s at the averaging level shown in Fig. 48. Figure 50 below shows the detected THz pulse in time and frequency domains for electro-optic sampling using the laser pulse as probe, and for the PCF-shaped probe detected with USB spectrometer and periodic waveform analyzer. The shape of the pulses differ in the time domain, but share the same central dip. Alignment of the probe as it overlaps with the THz spot likely accounts for the discrepancy. The electro-optic sampling noise floor is an order of magnitude lower than for spectral encoding. This suggests that the to reach the same noise floor as with EOS, the signal would have to be averaged 100 times more based on the noise$\propto 1/\sqrt{N}$ rule of thumb.

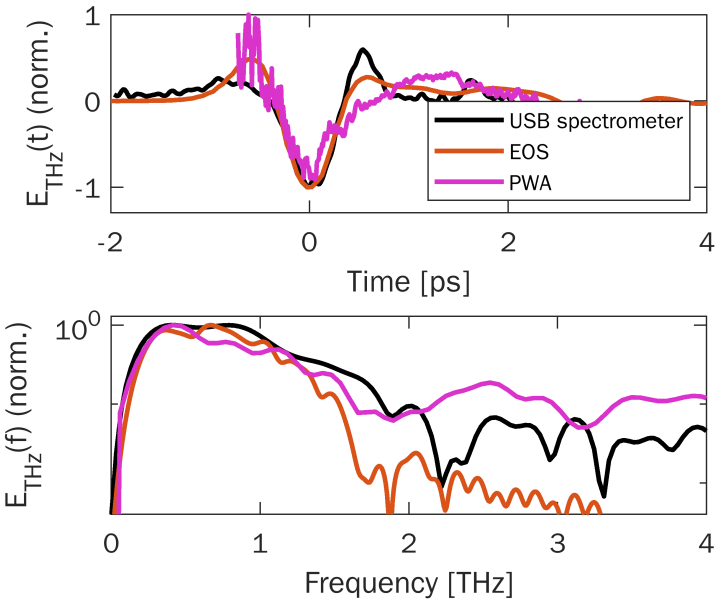

Figure 50: THz pulse comparison between USB spectrometer, periodic waveform analyzer (PWA) and conventional electro-optic sampling (EOS). Top panel shows signal in the time domain; below is frequency content in log scale. For the Fourier transform and processing, the USB spectrometer dataset was restricted to the region between -1.7 and 1.9 ps.

The performance of the spectral encoding technique could be improved with a higher quality spectrometer. For the DFT technique, direct comparison is more difficult as the THz trace is not fully visible in the measurements to date. However, the rapid data acquisition using the PWA or scope show promise for matching the signal to noise ratio of electro-optic sampling for the same total acquisition time. Currently, the noise floor appears 10 to 15 dB above that of electro-optic sampling with a 1 s acquisition time. With some improvements to alignment and signal-to-noise, it should be feasible to bring the measurement quality on par with EOS for an equal averaging time of 2 minutes. Work on implementing the modifications mentioned above is being carried out successfully to enable single-shot spectroscopy measurements and the observation of shot-to-shot variability in samples. A manuscript is in preparation.

5.2 Applications

Once we reach this threshold for measurement noise level, we can consider future perspectives on how the technique might be used to enhance our current understanding of ultrafast processes. This technique is promising for investigating samples that undergo transitions or are prone to degrading in the lab. Examples of ultrafast single-shot measurements across the electromagnetic spectrum exist in the literature; a selection follows.

In chemistry, there is increasing interest in studying chemical reactions as they occur in order to understand intermediate stages of transitions. While valence electron dynamics or changes to single bonds occur on a sub-femtosecond time scale, more complex reactions such as reduction–oxidation of large molecules in liquid phase may take place on a microsecond to millisecond time scale, readily within the reach of laser repetition rates. Real-time monitoring of reactions in the X-ray and visible regions has been demonstrated [108]. Biological molecules such as proteins are another source of irreversible transitions to study on a single-shot basis [109].

Experiments in chemical monitoring slice-selective NMR spectroscopy have been used to distinguish between liquid phase samples as they separate or undergo reactions [14]. This is shown in Fig. 51 which schematically depicts the separated phases contained in a single vial and the transitional spectrum at their junction. This technique is practical for its noninvasive nature [110]. THz spectroscopy could be used in a similar way to monitor sample composition using its sensitivity to rotational and vibrational modes of molecules and their structural form [3].

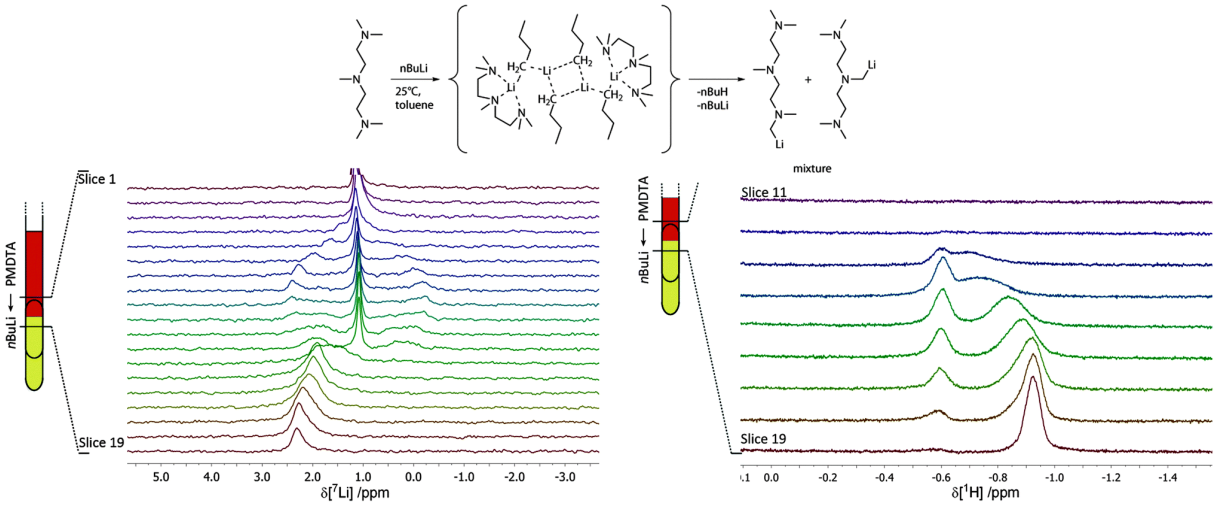

Figure 51: Selected NMR spectroscopy slices from titration experiment illustrating variable composition [14].

This slice selection is also similar to the assembly line characterization as proposed in [50], with material composition probed along the sample length as it travels through the THz beam with a known velocity.

Single-shot pump-probe experiments in the NIR have been performed with dual echelons to achieve 20 fs time resolution over a total 9 ps window. This ensures that samples which do not relax to their original state between pump pulses are accurately characterized despite potentially irreversible damage from the pump [111]. In fact, the literature for single-shot transient absorption spectroscopy mirrors that of single-shot THz detection in the design of techniques for encoding time on another degree of freedom of the probe pulse [112]. In the X-ray region there has been ultrafast monitoring of laser induced non-reproducible demagnetization dynamics using radiation from a free-electron laser [113].

Finally, there is potential to incorporate compressed sensing reconstruction algorithms into multidimensional high-speed detection systems to further accelerate data acquisition as shown for Raman imaging in the visible [46] or in ultrafast THz spectroscopy [45].

References

[1] K. Fukunaga, I. Hosako, I. N. Duling III, and M. Picollo. Terahertz imaging systems: a non-invasive technique for the analysis of paintings. In Luca Pezzati and Renzo Salimbeni, editors, O3A: Optics for Arts, Architecture, and Archaeology II, volume 7391, pages 119 – 127. International Society for Optics and Photonics, SPIE, 2009.

[2] Iwao Hosako, Norihiko Sekine, Mikhail Patrashin, Shingo Saito, Kaori Fukunaga, Yasuko Kasai, Philippe Baron, Takamasa Seta, Jana Mendrok, Satoshi Ochiai, and Hiroaki Yasuda. At the dawn of a new era in terahertz technology. Proceedings of the IEEE, 95(8):1611–1623, 2007.

[3] Bernd M. Fischer, Hanspeter Helm, and Peter Uhd Jepsen. Chemical recognition with broadband THz spectroscopy. Proceedings of the IEEE, 95(8):1592–1604, 2007.

[4] Wei Cui, Aidan W. Schiff-Kearn, Emily Zhang, Nicolas Couture, Francesco Tani, David Novoa, Philip St.J. Russell, and Jean-Michel Ménard. Broadband and tunable time-resolved THz system using argon-filled hollow-core photonic crystal fiber. APL Photonics, 3(11):111301, 2018.

[5] János Hebling, Ka-Lo Yeh, Matthias C. Hoffmann, Balázs Bartal, and Keith A. Nelson. Generation of high-power terahertz pulses by tilted-pulse-front excitation and their application possibilities. J. Opt. Soc. Am. B, 25(7):B6–B19, Jul 2008.

[6] H. Hirori, A. Doi, F. Blanchard, and K. Tanaka. Single-cycle terahertz pulses with amplitudes exceeding 1 MV/cm generated by optical rectification in LiNbO3. Applied Physics Letters, 98(9):091106, 2011.

[7] J. A. Fülöp, L. Pálfalvi, G. Almási, and J. Hebling. Design of high-energy terahertz sources based on optical rectification. Opt. Express, 18(12):12311–12327, Jun 2010.

[8] Stephanie M. Teo, Benjamin K. Ofori-Okai, Christopher A. Werley, and Keith A. Nelson. Invited article: Single-shot THz detection techniques optimized for multidimensional THz spectroscopy. Review of Scientific Instruments, 86(5):051301, 2015.

[9] Takeshi Yasui, Yasuhiro Kabetani, Eisuke Saneyoshi, Shuko Yokoyama, and Tsutomu Araki. Terahertz frequency comb by multifrequency-heterodyning photoconductive detection for high-accuracy, high-resolution terahertz spectroscopy. Applied Physics Letters, 88(24):241104, 2006.

[10] Govind P. Agrawal. Nonlinear Fiber Optics. Academic Press, sixth edition, 2019.

[11] Nicolas Couture, Rachel Ostic, P Harshavardhan Reddy, Ajoy Kumar Kar, Mukul Chandra Paul, and Jean-Michel Ménard. Polarization-resolved supercontinuum generated in a germania-doped photonic crystal fiber. Journal of Physics: Photonics, 3(2):025002, mar 2021.

[12] Idan Parshani, Leon Bello, Mallachi-Elia Meller, and Avi Pe'er. Diffractive saturable loss mechanism in kerr-lens mode-locked lasers: direct observation and simulation. Opt. Lett., 46(7):1530–1533, Apr 2021.

[13] Aidan Schiff-Kearn. Experimental and numerical investigations into terahertz time-domain spectroscopy. Master's thesis, University of Ottawa, Ottawa, ON, January 2019.

[14] T. Niklas, D. Stalke, and M. John. Single-shot titrations and reaction monitoring by slice-selective NMR spectroscopy. Chem. Commun., 51:1275–1277, 2015.

[15] Yun-Shik Lee. Principles of Terahertz Science and Technology. Springer, Boston, 2009.

[16] Derek Abbott and Xi-Cheng Zhang. Special issue on T-Ray imaging, sensing, and retection. Proceedings of the IEEE, 95(8):1509–1513, 2007.

[17] P.R. Smith, D.H. Auston, and M.C. Nuss. Subpicosecond photoconducting dipole antennas. IEEE Journal of Quantum Electronics, 24(2):255–260, 1988.

[18] C. Baker, T. Lo, W. R. Tribe, B. E. Cole, M. R. Hogbin, and M. C. Kemp. Detection of concealed explosives at a distance using terahertz technology. Proceedings of the IEEE, 95(8):1559–1565, 2007.

[19] Hai-Bo Liu, Hua Zhong, Nicholas Karpowicz, Yunqing Chen, and Xi-Cheng Zhang. Terahertz spectroscopy and imaging for defense and security applications. Proceedings of the IEEE, 95(8):1514–1527, 2007.

[20] Maksym Ivanov, Illia Thiele, Luc Bergé, Stefan Skupin, Danas Buožius, and Virgilijus Vaičaitis. Intensity modulated terahertz vortex wave generation in air plasma by two-color femtosecond laser pulses. Opt. Lett., 44(15):3889–3892, Aug 2019.

[21] T. Seifert, S. Jaiswal, U. Martens, J. Hannegan, L. Braun, P. Maldonado, F. Freimuth, A. Kronenberg, J. Henrizi, I. Radu, E. Beaurepaire, Y. Mokrousov, P. M. Oppeneer, M. Jourdan, G. Jakob, D. Turchinovich, L. M. Hayden, M. Wolf, M. Münzenberg, M. Kläui, and T. Kampfrath. Efficient metallic spintronic emitters of ultrabroadband terahertz radiation. Nature Photonics, 10:483–488, 7 2016.

[22] Z. Y. Tan, Tao Zhou, J. C. Cao, and H. C. Liu. Terahertz imaging with quantum-cascade laser and quantum-well photodetector. IEEE Photonics Technology Letters, 25(14):1344–1346, 2013.

[23] Withawat Withayachumnankul and Mira Naftaly. Fundamentals of measurement in terahertz time-domain spectroscopy. Journal of Infrared, Millimeter, and Terahertz Waves, 35(8):610–637, 2014.

[24] Sophie Eliet, Arnaud Cuisset, Francis Hindle, Jean-François Lampin, and Romain Peretti. Broadband super-resolution terahertz time domain spectroscopy applied to gas analysis, 2021.

[25] Withawat Withayachumnankul, Gretel M. Png, Xiaoxia Yin, Shaghik Atakaramians, Inke Jones, Hungyen Lin, Benjamin Seam Yu Ung, Jegathisvaran Balakrishnan, Brian W.-H. Ng, Bradley Ferguson, Samuel P. Mickan, Bernd M. Fischer, and Derek Abbott. T-ray sensing and imaging. Proceedings of the IEEE, 95(8):1528–1558, 2007.

[26] T. L. Cocker, D. Baillie, M. Buruma, L. V. Titova, R. D. Sydora, F. Marsiglio, and F. A. Hegmann. Microscopic origin of the Drude-Smith model. Phys. Rev. B, 96:205439, Nov 2017.

[27] John F. O'Hara, Sabit Ekin, Wooyeol Choi, and Ickhyun Song. A perspective on terahertz next-generation wireless communications. Technologies, 7(2), 2019.

[28] Alexei Halpin, Nicolas Couture, and Jean-Michel Ménard. Optical pulse structuring in gas-filled hollow-core kagomé PCF for generation and detection of phase-locked multi-THz pulses. Opt. Mater. Express, 9(7):3115–3122, Jul 2019.

[29] Lu Wang, György Tóth, János Hebling, and Franz Kärtner. Tilted-pulse-front schemes for terahertz generation. Laser & Photonics Reviews, 14(7):2000021, 2020.

[30] Robert Boyd. Nonlinear Optics. Academic Press, third edition, 2008.

[31] R. A. Kaindl, F. Eickemeyer, M. Woerner, and T. Elsaesser. Broadband phase-matched difference frequency mixing of femtosecond pulses in gase: Experiment and theory. Applied Physics Letters, 75(8):1060–1062, 1999.

[32] H A Hafez, X Chai, A Ibrahim, S Mondal, D Férachou, X Ropagnol, and T Ozaki. Intense terahertz radiation and their applications. Journal of Optics, 18(9):093004, aug 2016.

[33] János Hebling, Gábor Almási, Ida Z. Kozma, and Jürgen Kuhl. Velocity matching by pulse front tilting for large-area THz-pulse generation. Opt. Express, 10(21):1161–1166, Oct 2002.

[34] J. Hebling, A.G. Stepanov, G. Almási, B. Bartal, and J. Kuhl. Tunable THz pulse generation by optical rectification of ultrashort laser pulses with tilted pulse fronts. Applied Physics B, 78:593–599, 2004.

[35] A. G. Stepanov, J. Kuhl, I. Z. Kozma, E. Riedle, G. Almási, and J. Hebling. Scaling up the energy of THz pulses created by optical rectification. Opt. Express, 13(15):5762–5768, Jul 2005.

[36] Levente Tokodi, J. Hebling, and L. Pálfalvi. Optimization of the tilted-pulse-front terahertz excitation setup containing telescope. Journal of Infrared, Millimeter, and Terahertz Waves, 38:22–32, 2017.

[37] Mark Cronin-Golomb. Cascaded nonlinear difference-frequency generation of enhanced terahertz wave production. Opt. Lett., 29(17):2046–2048, Sep 2004.

[38] József András Fülöp, László Pálfalvi, Matthias C. Hoffmann, and János Hebling. Towards generation of mJ-level ultrashort THz pulses by optical rectification. Opt. Express, 19(16):15090–15097, Aug 2011.

[39] Toshiaki Hattori and Masaya Sakamoto. Eo sampling methods for real-time thz imaging. In 2007 Joint 32nd International Conference on Infrared and Millimeter Waves and the 15th International Conference on Terahertz Electronics, pages 915–916, 2007.

[40] F. Blanchard, L. Razzari, H.-C. Bandulet, G. Sharma, R. Morandotti, J.-C. Kieffer, T. Ozaki, M. Reid, H. F. Tiedje, H. K. Haugen, and F. A. Hegmann. Generation of 1.5 μJ single-cycle terahertz pulses by optical rectification from a large aperture ZnTe crystal. Opt. Express, 15(20):13212–13220, Oct 2007.

[41] Zurich Instruments. White paper: Principles of lock-in detection and the state of the art, 2016.

[42] Zhiping Jiang, F. G. Sun, Q. Chen, and X.-C. Zhang. Electro-optic sampling near zero optical transmission point. Applied Physics Letters, 74(9):1191–1193, 1999.

[43] Brandon K. Russell, Benjamin K. Ofori-Okai, Zhijiang Chen, Matthias C. Hoffmann, Ying Y. Tsui, and Siegfried H. Glenzer. Self-referenced single-shot THz detection. Opt. Express, 25(14):16140–16150, Jul 2017.

[44] J. van Tilborg, C. B. Schroeder, Cs. Tóth, C. G. R. Geddes, E. Esarey, and W. P. Leemans. Single-shot spatiotemporal measurements of high-field terahertz pulses. Opt. Lett., 32(3):313–315, Feb 2007.

[45] Sushovit Adhikari, Cristian L. Cortes, Xiewen Wen, Shobhana Panuganti, David J. Gosztola, Richard D. Schaller, Gary P. Wiederrecht, and Stephen K. Gray. Accelerating ultrafast spectroscopy with compressive sensing. Phys. Rev. Applied, 15:024032, Feb 2021.

[46] Jonathan V. Thompson, Joel N. Bixler, Brett H. Hokr, Gary D. Noojin, Marlan O. Scully, and Vladislav V. Yakovlev. Single-shot chemical detection and identification with compressed hyperspectral Raman imaging. Opt. Lett., 42(11):2169–2172, Jun 2017.

[47] Zhiping Jiang and X.-C. Zhang. Electro-optic measurement of THz field pulses with a chirped optical beam. Applied Physics Letters, 72(16):1945–1947, 1998.

[48] U. Schmidhammer, V. De Waele, J.-R. Marquès, N. Bourgeois, and M. Mostafavi. Single shot linear detection of 0.01–10 THz electromagnetic fields. Applied Physics B, 94(95), 2008.

[49] Peng Yu Han, Zhiping Jiang, Jennifer A. Riordan, Lijun Wang, and Xi-Cheng Zhang. Ultrafast electro-optic sensors and magneto-optic sensors for THz beams. In Kong-Thon F. Tsen and Harold R. Fetterman, editors, Ultrafast Phenomena in Semiconductors II, volume 3277, pages 198 – 207. International Society for Optics and Photonics, SPIE, 1998.

[50] Pierre Jeunesse and Uli Schmidhammer. "On-the-fly" monitoring with a single-shot terahertz time-domain spectrometer. IEEE Sensors Journal, 13(1):44–49, 2013.

[51] J. R. Fletcher. Distortion and uncertainty in chirped pulse THz spectrometers. Opt. Express, 10(24):1425–1430, Dec 2002.

[52] N. H. Matlis, G. R. Plateau, J. van Tilborg, and W. P. Leemans. Single-shot spatiotemporal measurements of ultrashort THz waveforms using temporal electric-field cross correlation. J. Opt. Soc. Am. B, 28(1):23–27, Jan 2011.

[53] Gargi Sharma, Kanwarpal Singh, Ibraheem Al-Naib, Roberto Morandotti, and Tsuneyuki Ozaki. Terahertz detection using spectral domain interferometry. Opt. Lett., 37(20):4338–4340, Oct 2012.

[54] Shuiqin Zheng, Xinjian Pan, Yi Cai, Qinggang Lin, Ying Li, Shixiang Xu, Jingzhen Li, and Dianyuan Fan. Common-path spectral interferometry for single-shot terahertz electro-optics detection. Opt. Lett., 42(21):4263–4266, Nov 2017.

[55] Yupeng Fan, Junjun Xiao, and Yi Li. Single-shot measurement of the free-space time domain terahertz (THz) waveforms by iterative frequency-domain interferometry technology. Optical and Quantum Electronics, 51:323, 2019.

[56] Jonas Hammer, P. Hosseini, C. R. Menyuk, Philip St.J. Russell, and Nicolas Y. Joly. Single-shot reconstruction of spectral amplitude and phase in a fiber ring cavity at a 80 MHz repetition rate. Opt. Lett., 41(20):4641–4644, Oct 2016.

[57] Jie Shan, Aniruddha S. Weling, Ernst Knoesel, Ludwig Bartels, Mischa Bonn, Ajay Nahata, Georg A. Reider, and Tony F. Heinz. Single-shot measurement of terahertz electromagnetic pulses by use of electro-optic sampling. Opt. Lett., 25(6):426–428, Mar 2000.

[58] Takeshi Yasui, Ken ichi Sawanaka, Atsushi Ihara, Emmanuel Abraham, Mamoru Hashimoto, and Tsutomu Araki. Real-time terahertz color scanner for moving objects. Opt. Express, 16(2):1208–1221, Jan 2008.

[59] Yoichi Kawada, Takashi Yasuda, Atsushi Nakanishi, Koichiro Akiyama, and Hironori Takahashi. Single-shot terahertz spectroscopy using pulse-front tilting of an ultra-short probe pulse. Opt. Express, 19(12):11228–11235, Jun 2011.

[60] Zhao-Hui Zhai, Sen-Cheng Zhong, Jun Li, Li-Guo Zhu, Kun Meng, Jiang Li, Qiao Liu, Qi-Xian Peng, Ze-Ren Li, and Jian-Heng Zhao. Time-resolved single-shot terahertz time-domain spectroscopy for ultrafast irreversible processes. Review of Scientific Instruments, 87(9):095101, 2016.

[61] Steven P. Jamison, Jingling Shen, A. M. MacLeod, W. A. Gillespie, and D. A. Jaroszynski. High-temporal-resolution, single-shot characterization of terahertz pulses. Opt. Lett., 28(18):1710–1712, Sep 2003.

[62] Gregory P. Wakeham and Keith A. Nelson. Dual-echelon single-shot femtosecond spectroscopy. Opt. Lett., 25(7):505–507, Apr 2000.

[63] K. Y. Kim, B. Yellampalle, A. J. Taylor, G. Rodriguez, and J. H. Glownia. Single-shot terahertz pulse characterization via two-dimensional electro-optic imaging with dual echelons. Opt. Lett., 32(14):1968–1970, Jul 2007.

[64] Taeho Shin, Johanna W. Wolfson, Samuel W. Teitelbaum, Maria Kandyla, and Keith A. Nelson. Dual echelon femtosecond single-shot spectroscopy. Review of Scientific Instruments, 85(8):083115, 2014.

[65] G. Timothy Noe, Ikufumi Katayama, Fumiya Katsutani, James J. Allred, Jeffrey A. Horowitz, David M. Sullivan, Qi Zhang, Fumiya Sekiguchi, Gary L. Woods, Matthias C. Hoffmann, Hiroyuki Nojiri, Jun Takeda, and Junichiro Kono. Single-shot terahertz time-domain spectroscopy in pulsed high magnetic fields. Opt. Express, 24(26):30328–30337, Dec 2016.

[66] Yasuo Minami, Kohei Horiuchi, Kaisei Masuda, Jun Takeda, and Ikufumi Katayama. Terahertz dielectric response of photoexcited carriers in Si revealed via single-shot optical-pump and terahertz-probe spectroscopy. Applied Physics Letters, 107(17):171104, 2015.

[67] Sonal Saxena, Suman Bagchi, Bobbili Sanyasi Rao, Prasad Anant Naik, and Juzer Ali Chakera. Single-shot terahertz time profiling using curved wavefront. IEEE Transactions on Terahertz Science and Technology, 8(5):528–534, 2018.

[68] Takeshi Yasui, Eisuke Saneyoshi, and Tsutomu Araki. Asynchronous optical sampling terahertz time-domain spectroscopy for ultrahigh spectral resolution and rapid data acquisition. Applied Physics Letters, 87(6):061101, 2005.

[69] Péter Földesy. Terahertz single-shot quadrature phase-shifting interferometry. Opt. Lett., 37(19):4044–4046, Oct 2012.

[70] Yin-Zhong Wu, Zong-Qing Zhao, Yu-Qiu Gu, Lai Wei, and Lei-Feng Cao. New terahertz dispersive device for single-shot spectral measurements of terahertz pulse. Chinese Physics B, 23(12):125202, nov 2014.

[71] Stephan Wesch, Bernhard Schmidt, Christopher Behrens, Hossein Delsim-Hashemi, and Peter Schmüser. A multi-channel THz and infrared spectrometer for femtosecond electron bunch diagnostics by single-shot spectroscopy of coherent radiation. Nuclear Instruments and Methods in Physics Research Section A: Accelerators, Spectrometers, Detectors and Associated Equipment, 665:40–47, 2011.

[72] Dogeun Jang, Hanran Jin, and Ki-Yong Kim. Single-shot terahertz spectrometer using a microbolometer camera. Applied Physics Letters, 117(9):091105, 2020.

[73] C. Evain, E. Roussel, M. Le Parquier, C. Szwaj, M.-A. Tordeux, J.-B. Brubach, L. Manceron, P. Roy, and S. Bielawski. Direct observation of spatiotemporal dynamics of short electron bunches in storage rings. Phys. Rev. Lett., 118:054801, Feb 2017.

[74] C. Szwaj, C. Evain, M. Le Parquier, P. Roy, L. Manceron, J.-B. Brubach, M.-A. Tordeux, and S. Bielawski. High sensitivity photonic time-stretch electro-optic sampling of terahertz pulses. Review of Scientific Instruments, 87(10):103111, 2016.

[75] J. M. Dudley and J. R. Taylor, editors. Supercontinuum Generation in Optical Fibers, chapter 3. Cambridge University Press, 2010.

[76] Kristelle Roidot. Numerical Study of Non-linear Dispersive Partial Differential Equations. Theses, Université de Bourgogne, October 2011.

[77] MathWorks. ode45, 2021.

[78] John M. Dudley, Goëry Genty, and Stéphane Coen. Supercontinuum generation in photonic crystal fiber. Rev. Mod. Phys., 78:1135–1184, Oct 2006.

[79] J. P. Gordon. Theory of the soliton self-frequency shift. Opt. Lett., 11(10):662–664, Oct 1986.

[80] Chongqing Wu, Zhi Chao Wang, Yongpeng Zhao, and Fenghai Xu. Dispersion of principal polarization axes (PPA) in optical fiber. In Shuisheng Jian, Franklin F. Tong, and Reinhard Maerz, editors, Fiber Optic Components and Optical Communication II, volume 3552, pages 210 – 215. International Society for Optics and Photonics, SPIE, 1998.

[81] Mercédesz Horváth, Bálint G. Nagyillés, Tímea Grósz, and Attila P. Kovács. Wavelength-dependent orientation of the principal axes of photonic crystal fibers measured by windowed Fourier-transform spectral interferometry. Opt. Express, 28(2):2156–2165, Jan 2020.

[82] Antoine Proulx, Jean-Michel Ménard, Nicolas Hô, Jacques M. Laniel, Réal Vallée, and Claude Paré. Intensity and polarization dependences of the supercontinuum generation in birefringent and highly nonlinear microstructured fibers. Opt. Express, 11(25):3338–3345, Dec 2003.

[83] M. Lehtonen, G. Genty, H. Ludvigsen, and M. Kaivola. Supercontinuum generation in a highly birefringent microstructured fiber. Applied Physics Letters, 82(14):2197–2199, 2003.

[84] Haohua Tu, Yuan Liu, Xiaomin Liu, Dmitry Turchinovich, Jesper Lægsgaard, and Stephen A. Boppart. Nonlinear polarization dynamics in a weakly birefringent all-normal dispersion photonic crystal fiber: toward a practical coherent fiber supercontinuum laser. Opt. Express, 20(2):1113–1128, Jan 2012.

[85] Iván Bravo Gonzalo, Rasmus Dybbro Engelsholm, Mads Peter Sørensen, and Ole Bang. Polarization noise places severe constraints on coherence of all-normal dispersion femtosecond supercontinuum generation. Scientific Reports, 8:6579, 2018.

[86] Emiliano R. Martins, Danilo H. Spadoti, Murilo A. Romero, and Ben-Hur V. Borges. Theoretical analysis of supercontinuum generation in a highly birefringent D-shaped microstructured optical fiber. Opt. Express, 15(22):14335–14347, Oct 2007.

[87] Scott R. Domingue and Randy A. Bartels. Overcoming temporal polarization instabilities from the latent birefringence in all-normal dispersion, wave-breaking-extended nonlinear fiber supercontinuum generation. Opt. Express, 21(11):13305–13321, Jun 2013.

[88] Herbert G. Winful. Self-induced polarization changes in birefringent optical fibers. Applied Physics Letters, 47(3):213–215, 1985.

[89] Yuan Liu, Youbo Zhao, Jens Lyngsø, Sixian You, William L. Wilson, Haohua Tu, and Stephen A. Boppart. Suppressing short-term polarization noise and related spectral decoherence in all-normal dispersion fiber supercontinuum generation. Journal of Lightwave Technology, 33(9):1814–1820, 2015.

[90] R. J. Kruhlak, G. K. Wong, J. S. Chen, S. G. Murdoch, R. Leonhardt, J. D. Harvey, N. Y. Joly, and J. C. Knight. Polarization modulation instability in photonic crystal fibers. Opt. Lett., 31(10):1379–1381, May 2006.

[91] S. G. Murdoch, R. Leonhardt, and J. D. Harvey. Polarization modulation instability in weakly birefringent fibers. Opt. Lett., 20(8):866–868, Apr 1995.

[92] M. Monerie and L. Jeunhomme. Polarization mode coupling in long single-mode fibres. Optical and Quantum Electronics, 12(6):449–461, 1980.

[93] Sandra F. Feldman, Doreen A. Weinberger, and Herbert G. Winful. Observation of polarization instabilities and modulational gain in a low-birefringence optical fiber. Opt. Lett., 15(6):311–313, Mar 1990.

[94] Q.D. Liu, L. Shi, P.P. Ho, and R.R. Alfano. Nonlinear vector rotation and depolarization of femtosecond laser pulses propagating in non-birefringent single-mode optical fibers. Optics Communications, 138(1):45–48, 1997.

[95] Brendan J. Chick, JamesW.M. Chon, and Min Gu. Polarization effects in a highly birefringent nonlinear photonic crystal fiber with two-zero dispersion wavelengths. Opt. Express, 16(24):20099–20105, Nov 2008.

[96] G. Genty, M. Lehtonen, and H. Ludvigsen. Effect of cross-phase modulation on supercontinuum generated in microstructured fibers with sub-30 fs pulses. Opt. Express, 12(19):4614–4624, Sep 2004.

[97] Zhaoming Zhu and Thomas G. Brown. Polarization properties of supercontinuum spectra generated in birefringent photonic crystal fibers. Journal of the Optical Society of America B, 21(2):249–257, 2004.

[98] Ariel Flores-Rosas, Josue I. Peralta-Hernandez, Yazmin E. Bracamontes-Rodríguez, Balder A. Villagomez-Bernabe, Georgina Beltrán-Pérez, Olivier Pottiez, Baldemar Ibarra-Escamilla, Roberto Rojas-Laguna, and Evgeny A. Kuzin. Observation of a high grade of polarization of solitons generated in the process of pulse breakup in a twisted fiber. J. Opt. Soc. Am. B, 31(4):821–826, Apr 2014.

[99] A N Ghosh, M Meneghetti, C R Petersen, O Bang, L Brilland, S Venck, J Troles, J M Dudley, and T Sylvestre. Chalcogenide-glass polarization-maintaining photonic crystal fiber for mid-infrared supercontinuum generation. Journal of Physics: Photonics, 1(4):044003, sep 2019.

[100] Sterling Backus, Charles G. Durfee, Margaret M. Murnane, and Henry C. Kapteyn. High power ultrafast lasers. Review of Scientific Instruments, 69(3):1207–1223, 1998.

[101] Mira Naftaly and Richard Dudley. Methodologies for determining the dynamic ranges and signal-to-noise ratios of terahertz time-domain spectrometers. Opt. Lett., 34(8):1213–1215, Apr 2009.

[102] Yihong Yang, Alisha Shutler, and D. Grischkowsky. Measurement of the transmission of the atmosphere from 0.2 to 2 THz. Opt. Express, 19(9):8830–8838, Apr 2011.

[103] Pedram Abdolghader, Adrian F. Pegoraro, Nicolas Y. Joly, Andrew Ridsdale, Rune Lausten, François Légaré, and Albert Stolow. All normal dispersion nonlinear fibre supercontinuum source characterization and application in hyperspectral stimulated Raman scattering microscopy. Opt. Express, 28(24):35997–36008, Nov 2020.

[104] Sheila Galt, Mats Sjöberg, Manuel Lopez Quiroga-Teixeiro, and Sverker Hård. Optical breakdown in fused silica and argon gas: application to Nd:YAG laser limiter. Appl. Opt., 42(3):579–584, Jan 2003.

[105] John R. Rumble. CRC Handbook of Chemistry and Physics, chapter Dielectric Strength of Solids. CRC Press/Taylor & Francis, Boca Raton, FL, 102nd edition, 2021. Internet Version 2021.

[106] Ishan Sharma. Grating-pair chirped pulse amplification system for a low power femtosecond pulse source. Master's thesis, Cornell University, Ithaca, NY, August 2011.

[107] Suganda Jutamulia and Toshimitsu Asakura. Fourier transform property of lens based on geometrical optics. In Guoguang Mu, Francis T. S. Yu, and Suganda Jutamulia, editors, Optical Information Processing Technology, volume 4929, pages 80 – 85. International Society for Optics and Photonics, SPIE, 2002.

[108] Giorgio Olivo, Alessia Barbieri, Valeria Dantignana, Francesco Sessa, Valentina Migliorati, Manuel Monte, Sakura Pascarelli, Theyencheri Narayanan, Osvaldo Lanzalunga, Stefano Di Stefano, and Paola D'Angelo. Following a chemical reaction on the millisecond time scale by simultaneous X-ray and UV/Vis spectroscopy. The Journal of Physical Chemistry Letters, 8(13):2958–2963, 2017. PMID: 28605898.

[109] Jessica L. Klocke, Markus Mangold, Pitt Allmendinger, Andreas Hugi, Markus Geiser, Pierre Jouy, Jérôme Faist, and Tilman Kottke. Single-shot sub-microsecond mid-infrared spectroscopy on protein reactions with quantum cascade laser frequency combs. Analytical Chemistry, 90(17):10494–10500, 2018. PMID: 30080964.

[110] Robert Evans, Aran Sandhu, Tony Bridgwater, and Katie Chong. Slice-selective NMR: A noninvasive method for the analysis of separated pyrolysis fuel samples. Energy & Fuels, 31(4):4135–4142, 2017.

[111] Taeho Shin, Johanna W. Wolfson, Samuel W. Teitelbaum, Maria Kandyla, and Keith A. Nelson. Dual echelon femtosecond single-shot spectroscopy. Review of Scientific Instruments, 85(8):083115, 2014.

[112] Kelly S. Wilson, Zachary S. Walbrun, and Cathy Y. Wong. Single-shot transient absorption spectroscopy techniques and design principles. Spectrochimica Acta Part A: Molecular and Biomolecular Spectroscopy, 253:119557, 2021.

[113] Michele Buzzi, Mikako Makita, Ludovic Howald, Armin Kleibert, Boris Vodungbo, Pablo Maldonado, Jörg Raabe, Nicolas Jaouen, Harald Redlin, Kai Tiedtke, Peter M. Oppeneer, Christian David, Frithjof Nolting, and Jan Lüning. Single-shot monitoring of ultrafast processes via X-ray streaking at a free electron laser. Scientific Reports, 7:7253, 2017.

[114] Akira Wada, Satoshi Okude, Tetsuya Sakai, and Ryozo Yamauchi. GeO2 concentration dependence of nonlinear refractive index coefficients of silica-based optical fibers. Electronics and Communications in Japan (Part I: Communications), 79(11):12–19, 1996.

[115] K. Kieu, L. Schneebeli, J. M. Hales, J. W. Perry, R. A. Norwood, and N. Peyghambarian. Demonstration of zeno switching through inverse Raman scattering in an optical fiber. Opt. Express, 19(13):12532–12539, Jun 2011.

[116] Karsten Rottwitt and Jorn H. Povlsen. Analyzing the fundamental properties of Raman amplification in optical fibers. J. Lightwave Technol., 23(11):3597, Nov 2005.

Appendix

Simulation parameters

Quantity	Single-pulse PCF	SC paper	Reference
Number of time samples N	2^{12}	2^{14}	
Temporal window width (ps)	12	12	
λ_0 (nm)	1030	1034	
T_0 (fs)	180	185	
Pulse shape GVD (ps^2)	0.001	0	
Pulse shape TOD (ps^3)	-0.0002	0	
β_2 (ps^2/m)	0.015	0.0017	
β_3 (ps^3/m)	-3.7e-5	8.608e-5	
β_4 (ps^4/m)	3.0e-7	-7.75e-8	
β_5 (ps^5/m)	-1.1e-9	-1.08e-10	
β_6 (ps^6/m)	2.5e-12	0	
β_7 (ps^7/m)	6e-15	0	
n_2 (m^2/W)	3e-20	5.2e-20	[114]
A_{eff} (μm^2)	$\pi(1.45)^2$	$\pi(4)^2$	
Loss	Neglected	Neglected	
f_R	0.18	0.24	[10, 115]
$f_a = 1 - f_b$	1	0.79	[10]
τ_1 (fs)	13	12.2	[116, 115]
τ_2 (fs)	32	65	[116, 115]
τ_b (fs)	Neglected	96	[10]
Number of samples over propagation length N_z	200	200	
Birefringence	Neglected	1e-6	

Table 2: List of parameters used in fiber optic simulations

The quantities in green are measured or extracted from data analysis, the quantities in purple are "free" parameters estimated to reach good agreement with experimental data, yellow are values taken from literature and the remaining quantities were chosen to reach sufficient sampling ranges.

CGNLSE simulation code

The MATLAB code was expanded from an existing repository and consists of an input script and solver function for the CGNLSEs [75, 78]. The additions made during the MSc include optional dispersion for input pulse shaping, an additional correction to the Raman response and the addition of polarization sensitivity.

Provided below is the function `cgnlse` to define the differential equations to solve, an input script to define the parameters of the optical fiber and input pulse, and finally a snippet which generates a spectrogram representing the pulse after propagation in the fiber.

CGNLSE function

```
function [Z, ATx, ATy, AWx, AWy, W] = cgnlse(T, Ax, Ay, w0, gamma, betas,...
    birefringence, coupling, loss, fr, hA, hB, fB, flength, nsaves)
% Takes fiber parameters and solves CGNLSEs in linear XY polarization basis
% Returns spectrum and signal in time over fiber length

% Constant
c = 299792458*1e9/1e12;     % [nm/ps] speed of light

% === Time and frequency grids
n = length(T);
dT = T(2)-T(1); % grid parameters
V = 2*pi*(-n/2:n/2-1)'/(n*dT); % [rad*THz] angular frequency grid (relative to w0)

% === Loss conversion
alpha = log(10.^(loss/10));    % [m^{-1}]

% === Dispersion
B = 0;
for ii = 1:length(betas)        % Taylor expansion of dispersion coefficients
  B = B + betas(ii)/factorial(ii+1).*V.^(ii+1);
end

% === Linear operators for each axis
birefringence = birefringence/(c*1e-9); % from dimensionless to units
Lx = 1i*(B - birefringence/2.*V) - alpha/2;
Ly = 1i*(B + birefringence/2.*V) - alpha/2;

% === Self-steepening when carrier frequency nonzero
if abs(w0) > eps                % if w0>0 then include shock
    gamma = gamma/w0;
    W = V + w0;                 % for shock W is true (absolute) freq
else
    W = 1;                      % set W to 1 when no shock
end

% === Raman
fA = 1 - fB;
```

```
hR = fA*hA + fB*hB;
hAW = n*ifft(fftshift(hA.'));   % frequency domain Raman
hBW = n*ifft(fftshift(hB.'));
hRW = n*ifft(fftshift(hR.'));

Lx = fftshift(Lx); W = fftshift(W); % shift to fft space
Ly = fftshift(Ly);

% === "Concatenate" the two axes contributions for ode solver
AWin = horzcat( ifft(Ax), ifft(Ay) ); % use ifft to go from time to freq

% === Define function to return derivative in z (freq domain ODE)
function R = rhs(z, AW)
  AWx = AW(1:n);                    % separate the inputs
  AWy = AW(n+1:2*n);

  ATx = fft(AWx.*exp(Lx*z));         % time domain field
  ATy = fft(AWy.*exp(Ly*z));

  ITx = abs(ATx).^2;                % time domain intensity
  ITy = abs(ATy).^2;

  if (length(hA) == 1) || (abs(fr) < eps) % no Raman case (not used, left for reference)
    Mx = ifft( ATx.*(ITx + 2/3*ITy) );
    My = ifft( ATy.*(ITy + 2/3*ITx) );
    sprintf('%s','no raman')

  else % Raman convolution included

    % === Full response
    RSx = dT*fr*( ATx.*( fft(ifft(ITx).*hRW) + fA*fft(ifft(ITy).*hAW) )...
        + (fB/2)*ATy.*( fft(ifft(ATx.*conj(ATy))...
        + conj(ATx).*ATy.*exp(-2*1i*birefringence*z)).*hBW) ) );
    RSy = dT*fr*( ATy.*( fft(ifft(ITy).*hRW) + fA*fft(ifft(ITx).*hAW) )...
        + (fB/2)*ATx.*( fft(ifft(ATy.*conj(ATx))...
        + conj(ATy).*ATx.*exp(-2*1i*birefringence*z)).*hBW) ) );
    Mx = ifft( (1-fr).*(ATx.*(ITx + (2/3)*ITy)...
        + 1i*gamma/3*conj(ATx).*ATy.^2.*exp(-2*1i*birefringence*z)) + RSx );
    My = ifft( (1-fr).*(ATy.*(ITy + (2/3)*ITx)...
        + 1i*gamma/3*conj(ATy).*ATx.^2.*exp(-2*1i*birefringence*z)) + RSy );

  end

  % Put together differential equation
  Rx = ( coupling.*AWy.*exp(Ly*z) + 1i*gamma*W.*Mx ).*exp(-Lx*z);
  Ry = ( -conj(coupling).*AWx.*exp(Lx*z) + 1i*gamma*W.*My ).*exp(-Ly*z);

  % Concatenate x and y along correct direction
  R = vertcat(Rx, Ry);
```

```
end

% === Define function to print ODE integrator status
function status = report(z, ~, flag) %
  status = 0;
  if isempty(flag)
    fprintf('%05.1f %% complete\n', z/flength*100);
  end
end

% === ODE integrator
Z = linspace(0, flength, nsaves);  % interpolate output z points
% === Set error tolerance options
options = odeset('RelTol', 1e-5, 'AbsTol', 1e-12, ...
                 'NormControl', 'on', ...
                 'OutputFcn', @report);
[Z, AW] = ode45(@rhs, Z, AWin, options); % run integrator

% === Process output of integrator
AWx = AW(:, 1:n);
AWy = AW(:, n+1:2*n);
ATx = zeros(size(AWx));
ATy = zeros(size(AWy));
for ii = 1:nsaves
  AWx(ii,:) = AWx(ii,:).*exp(Lx.'*Z(ii)); % change variables
  AWy(ii,:) = AWy(ii,:).*exp(Ly.'*Z(ii));
  ATx(ii,:) = fft(AWx(ii,:));           % time domain output
  ATy(ii,:) = fft(AWy(ii,:));
  AWx(ii,:) = fftshift(AWx(ii,:))./dT;  % scale
  AWy(ii,:) = fftshift(AWy(ii,:))./dT;
end

W = V + w0; % absolute frequency grid
end
```

Input script

```
% Script for fiber parameters and input pulse definition

n = 2^12;                   % number of grid points in time/frequency
twidth = 12;                % [ps] width of time window
c = 299792458*1e9/1e12;     % [nm/ps] speed of light
wavelength = 1030;          % [nm] reference wavelength
w0 = (2.0*pi*c)/wavelength; % [rad*THz] reference frequency
T = linspace(-twidth/2, twidth/2, n); % [ps] time grid [ps]
    dT = T(2) - T(1);

% === Freq array (omega) for fourier transform space
```

```
V = 2*pi*(-n/2:n/2-1)/(n*dT*1e-12); % [rad/s] frequency grid

% === Input pulse
pulsen = 5e-9;      % [J] pulse energy
t0 = 0.2;           % [ps] duration of input FWHM
power = pulsen /(t0*1e-12);     % [W] peak input power
A00 =  exp(-1/2*T.^2/(t0*0.6004).^2);  % gaussian shape

% === Pulse shaping dispersion
b1 = 0;
b2 = 0*(1e-12)^2; % [s^2]
b3 = 0;%0.001*(1e-12)^3; % [s^3]
b4 = 0;%-0.0002*(1e-12)^4; % [s^4]
A0_freq = fftshift(fft(A00));

A1_freq = A0_freq.* exp(1i.*( b1*V + 1/2.*b2.*V.^2 + ...
    1/6.*b3.*V.^3 + 1/24.*b4.*V.^4 ));

A0 = ifft(ifftshift(A1_freq));
% This will decrease the peak power, to preserve:
% A0 = A0/max(abs(A0)):

% === Fiber parameters
flength = 1;                % [m] fiber length
% betas = [beta2, beta3, ...] in units [ps^2/m, ps^3/m ...]
betas = [0.001780890334886, 8.608e-5, -7.75e-8, -1.08e-10,0];
n2 = 3e-20;                 % [m^2/W] nonlinear index of refraction
Aeff = pi*(3e-6)^2;         % [m^2] effective mode area
gamma = (w0*1e12)*n2/(c*1e3)/Aeff;   % [1/W/m] nonlinear coefficient
loss = 0;                   % [dB/m] loss
birefringence = 1e-5;       % dimensionless
mode_coupling = 0.5;        % [/m] "twist rate"
theta = 5 *pi/180;          % [rad] input polarization angle with respect to x

% === Raman response
fr = 0.2;                   % fractional Raman contribution
tau1 = 0.012; tau2 = 0.06;  % [ps] timescales for oscillatory Raman
hA = (tau1^2+tau2^2)/(tau1*tau2^2)*exp(-T/tau2).*sin(T/tau1); % damped oscillator model
hA(T<0) = 0;                % heaviside step function
tauB = 0.09;                % [ps] timescale for nonoscillatory Raman
hB = (2*tauB - T)./tauB^2.*exp(-T/tauB);
hB(T<0) = 0;
fB = 0.2;                   % fractional part for B, fA=1-fB

% === simulation parameters
nsaves = 200;    % number of z steps to save field at

% === Project onto axes
A_x = A0*cos(theta)*sqrt(power);   % x axis
```

```
A_y = A0*sin(theta)*sqrt(power);   % y axis

% === Propagate field through differential equation
[Z, ATx, ATy, AWx, AWy, W] = cgnlse(T, A_x, A_y, w0, gamma, betas, birefringence,...
                                mode_coupling, loss, fr, hA, hB, fB, flength, nsaves);

% === Window for plotting
WL = 2*pi*c./W;
% conditional selection to avoid wrapping
wlmin = 700;
wlmax = 1500;
iis = (WL>wlmin & WL<wlmax);

% === Log scale intensity
% Frequency
lIWx = 10*log10(abs(AWx).^2);
lIWy = 10*log10(abs(AWy).^2);
mlIW = max( max(max(lIWx)), max(max(lIWy)) ); % max value, for scaling plot
% Time
lITx = 10*log10(abs(ATx).^2);
lITy = 10*log10(abs(ATy).^2);
mlIT = max( max(max(lITx)), max(max(lITy)) ); % max value

% === Surface plots for data visualization
% Wavelength
figure(1)
subplot(1,2,1)
pcolor(WL(iis), Z, lIWx(:,iis))
colormap jet
shading flat
caxis([mlIW-50, mlIW])
xlabel('Wavelength [nm]')
ylabel('Distance [m]')
title('X')
set(gca,'tickdir','out','box','off','linew',1,'XMinorTick','on')

subplot(1,2,2)
pcolor(WL(iis), Z, lIWy(:,iis))
colormap jet
shading flat
caxis([mlIW-50, mlIW])
xlabel('Wavelength [nm]')
ylabel('Distance [m]')
title('Y')
set(gca,'tickdir','out','box','off','linew',1,'XMinorTick','on')

% Time
figure(2)
subplot(1,2,1)
```

```
pcolor(T, Z, lITx)
colormap jet
shading flat
caxis([mlIT-50, mlIT])
xlabel('Time [ps]')
ylabel('Distance [m]')
title('X')
set(gca,'tickdir','out','box','off','linew',1,'XMinorTick','on')

subplot(1,2,2)
pcolor(T, Z, lITy)
colormap jet
shading flat
caxis([mlIT-50, mlIT])
xlabel('Time [ps]')
ylabel('Distance [m]')
title('Y')
set(gca,'tickdir','out','box','off','linew',1,'XMinorTick','on')
```

The output should look like Fig. 52.

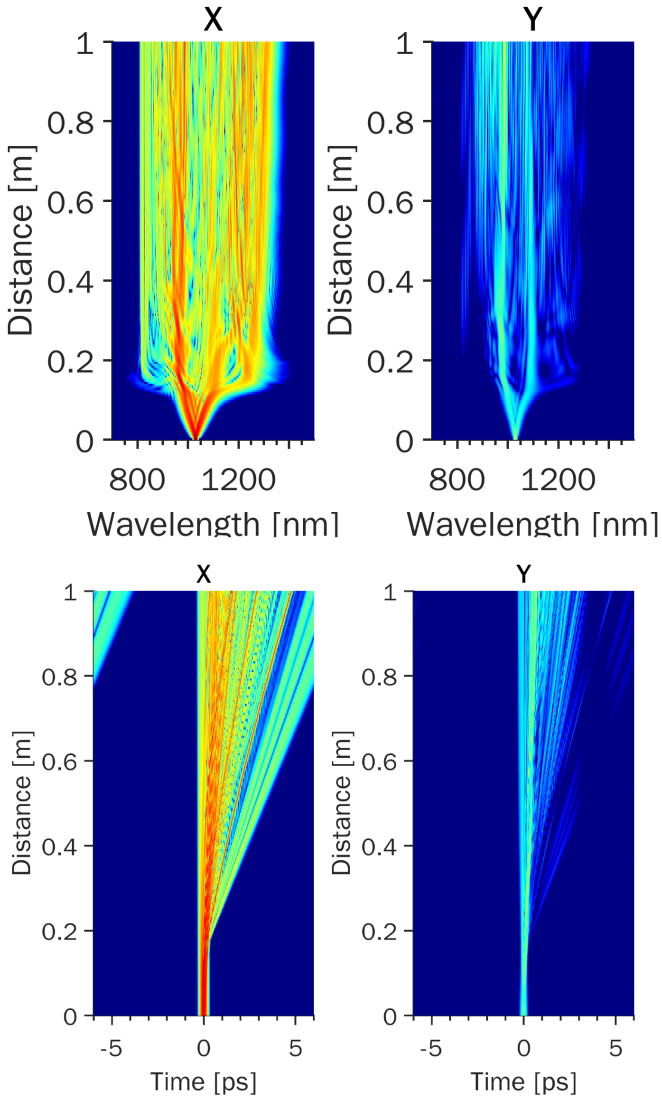

Figure 52: Output of sample code. Surface plots on 50 dB logarithmic scale.

Spectrogram

At the end of the input script, this optional section can be included as an example of how to generate a spectrogram. This can be useful to visualize how frequency components disperse in time and which ones may interact. This snippet shows takes the final spectrum from x polarization state and renders the spectrogram in log scale as shown in Fig. 53.

```
% === Spectrogram at fiber output (using input pulse as reference)
sigma = zeros(n);

   for specidx = 1:n

       tau = T(specidx);

       sigma(:,specidx) = ifftshift(ifft( ATx(nsaves,:)...
            .*exp(-1/2*(T-tau).^2/(t0*0.6004).^2) ));
       sigma(:,specidx) = abs(sigma(:,specidx)).^2;
```

```
        fprintf('Generating spectrogram %06.2f %% complete\n', specidx/n*100);
    end

figure(3)
pcolor( WL(iis), T, 10*log10(sigma(iis,:))' )
xlabel('Wavelength [nm]')
ylabel('Time [ps]')
title('X')
caxis([-50 0])
shading flat
colormap hot
```

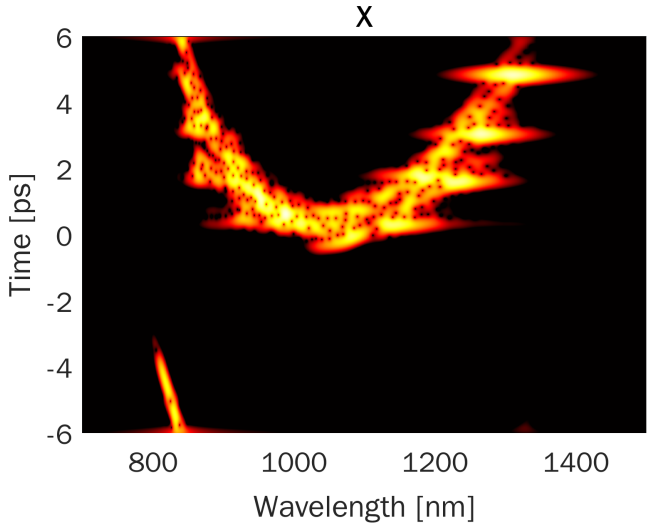

Figure 53: Output of spectrogram snippet. Surface plot on 50 dB logarithmic scale.

Grating dispersion

An extra useful function to calculate the GVD, TOD and FOD applied to a pulse after a double pass through a grating pair [100, 106].

```
function [GVD, TOD, FOD] = gratingpair(lambda_nm, sgroove, Lg_cm, thetai_deg)
% Calculate grating dispersion based on
% lambda_nm: center wavelength [nm]
% sgroove: groove density [/mm]
% Lg_cm: distance between gratings along normal [cm]
% thetai_deg: angle of incidence [deg]
% Outputs in [s^i/m] for i=2,3,4

% === Conversions and constants
lambda = lambda_nm *1e-9;
Lg = Lg_cm *1e-2;
c = 299792458;
Leff = Lg;
```

```
d = 1 / ( sgroove *1e3 ) ;
thetai = thetai_deg *( pi / 180 ) ;

% === Dispersion
GVD = -(lambda^3* Leff / ( pi*c^2*d^2 ) ) *(1 -( (lambda/d) - sin(thetai) )^2 )^(-3/2) ;

TOD = -(3/(2* pi) *lambda/c)*GVD *((1+( lambda* sin(thetai)/d ) -( sin(thetai ) )^2 )...
    /(1 -(( lambda/d ) - sin( thetai ) )^2 ) ) ;

FOD = (-3*d^2*lambda^5*Leff*(d^2*cos(4*thetai) +3*d^2 +4*cos(2*thetai)*(d^2-lambda^2)+...
    16*d*lambda*sin(thetai)*(cos(thetai))^2 +6*lambda^2)) / (8*pi^3*c^4*(-d*sin(thetai)...
    +d+lambda)^3*(d*sin(thetai)+d-lambda)^3*sqrt(1 -( (lambda/d) - sin(thetai) )^2 )) ;

end
```